UNIVERSIDADE FEDERAL DO ESPÍRITO SANTO
CENTRO TECNOLÓGICO
PROGRAMA DE PÓS-GRADUAÇÃO EM ENGENHARIA MECÂNICA

MARCO AURÉLIO BAZELATTO ZANONI

SMOLDERING COMBUSTION IN POROUS MEDIA: KINETIC MODELS FOR NUMERICAL SIMULATIONS

VITÓRIA-ES/BRAZIL
2012

MARCO AURÉLIO BAZELATTO ZANONI

SMOLDERING COMBUSTION IN POROUS MEDIA: KINETIC MODELS FOR NUMERICAL SIMULATIONS

Dissertation presented to the Post-graduation Programme in Mechanical Engineering of Federal University of Espírito Santo, as part of the requirements to obtain the title of **MASTER IN MECHANICAL ENGINEERING**.

Supervisor: Prof. Márcio Ferreira Martins, Ph.D

VITÓRIA-ES/BRAZIL

2012

MARCO AURÉLIO BAZELATTO ZANONI

SMOLDERING COMBUSTION IN POROUS MEDIA: KINETIC MODELS FOR NUMERICAL SIMULATIONS

Dissertation presented to the Post-graduation Programme in Mechanical Engineering of Federal University of Espírito Santo, as part of the requirements to obtain the title of **MASTER IN MECHANICAL ENGINEERING**.

Approved on 2012, March 05^{th}.

EVALUATION COMMITTEE:

Prof. Dr. Márcio Ferreira Martins - Supervisor
Universidade Federal do Espírito Santo

Prof. Dr. Emanuel Negrão Macêdo - External Member
Universidade Federal do Pará

Prof. Dr. Rogério Ramos - Internal Member
Universidade Federal do Espírito Santo

VITÓRIA-ES/BRAZIL

2012

“Seja você quem for, seja qual for a posição social que você tenha na vida, a mais alta ou a mais baixa, tenha sempre como meta muita força, muita determinação e sempre faça tudo com muito amor e com muita fé em Deus, que um dia você chega lá. De alguma maneira você chega lá”. (*Ayrton Senna*).

Acknowledgments

I would like to thank my family for encouraging me and giving me emotional support to get this Master degree.

I must acknowledge mainly my supervisor, Prof. Márcio Ferreira Martins. With him, I could improve my rigor in scientific research. He believed me and taught me to think critically. Today, he is more a mentor and friend than a professor. He also introduced me Dr. Guillermo Rein, that presented me Dr. Jason Gerhard, my future doctoral supervisor.

I would like to thank Dr. Henrique Massard da Fonseca for helping me with the numerical model simulations and my great friends Ramon, Anselmo, Bruno, Davi, Gabriel and Guilherme.

In conclusion, my sincere acknowledgments to the Agência Nacional do Petróleo - PRH-29/ANP and Coordenação de Aperfeiçoamento de Pessoal de Nível Superior - CAPES. I recognize that this research would not have been possible without these financial assistances. Also, I would like to thank the Petrobras and the Laboratório de Fenômenos de Transporte Computacional (LFTC/UFES) for the use of its computational facilities.

Abstract

Enhanced technologies for power generation using unconventional fuels - oil shale and its semi-coke, oil sands, extra-heavy oil and biomass from municipal solid waste and from sewage sludge - have in common thermochemical processes composed of complex chemical reactions. This work deals with the formulation and optimization of the chemical mechanism typically involved in oil shale pyrolysis and oil shale and its semi-coke combustion. Inverse problems (using the Levenberg-Marquardt algorithm) were employed to minimize the error between estimated values and the thermogravimetric data for kinetic pathways of 3-steps for oil shale pyrolysis, and 4-steps and 3-steps proposed for oil shale and its semi-coke respectively. The kinetic parameters such as reaction order, pre-exponential factor, activation energy and stoichiometric coefficients that affect drying, pyrolysis, oxidation and decarbonation reactions were estimated with success. Also, statistic and residual errors were evaluated, resulting in a reasonable value for all estimations. In addition, the kinetic mechanism proposed and estimated for semi-coke combustion was applied in a code in porous media. A parametric study between temperature profile and air velocity, and temperature profile and fixed carbon concentration was made. This study shows that the temperature profile is extremely influenced by these parameters confirming that the front propagation was controlled by O_2 supply.

Key Words: Oil Shale, Semi-Coke, Pyrolysis, Combustion, Parameters Estimation, Inverse Problems, Levenberg-Marquardt, Porous Media

Resumo

Tecnologias avançadas para a geração de energia usando combustíveis não convencionais - xisto betuminoso e seu semi-coque, areias betuminosas, petróleo extra-pesado e biomassa proveniente de resíduos sólidos urbanos e de lodo de esgoto - têm em comum processos termoquímicos compostos de complexas reações químicas. Este trabalho trata da formulação e otimização de mecanismos químicos normalmente envolvidos na pirólise do xisto betuminoso e na combustão do xisto betuminoso e seu semi-coque. Problemas inversos (usando o algoritmo de Levenberg-Marquardt) foram empregados para minimizar o erro entre os valores estimados e os dados de termogravimetria para os mecanismos de reação de 3 passos para a pirólise do xisto betuminos, e mecanismos de 4 e 3 passos para o xisto betuminoso e seu semi-coque, respectivamente. Os parâmetros cinéticos, tais como ordem de reação, fator pré-exponencial, energia de ativação e os coeficientes estequiométricos que afetam a secagem, as reações de oxidação, pirólise e descarbonatação foram estimadas com sucesso. Além disso, os erros estatísticos e residuais foram avaliados, resultando em um valor razoável para todas as estimativas e o mecanismo cinético proposto e estimado para a combustão do semi-coque foi aplicado em um código em meios porosos. Um estudo paramétrico entre o perfil de temperatura e a velocidade do ar, e o perfil de temperatura e a concentração de carbono fixo foi desenvolvido. Este estudo mostra que o perfil de temperatura é extremamente influenciado por estes parâmetros, confirmando que a propagação da frente é controlada pela injeção de O_2.

Palavras-chave: Xisto Betuminoso, Semi-Coque, Pirólise, Combustão, Estimação de Parâmettros, Problemas Inversos, Levenberg-Marquardt, Meios Porosos.

List of Publication

Papers

1. M. A. B. Zanoni, H. Massard, M. F. Martins, S. Salvador, *Application of Inverse Problem and Thermogravimetry to Determine the Kinetics of Oil Shale Pyrolysis*, High Temperatures High Pressures - The International Journal of Thermophysical Properties Research (Accepted);

2. M. A. B. Zanoni, H. Massard and M. F. Martins, *Formulating and optimizing a combustion pathways for oil shale and its semi-coke*, Combustion and Flame (Submitted);

Book Chapter

1. M. F. Martins, M. A. B. Zanoni, E. N. Macedo, Biomass and Renewable. Prof Daniel Favrat (Author); MER François Maréchal (Author); Yannick Bravo (Creator); Nicolas Borboen (Creator). (Org.). ECOS 2010: Proceedings of ECOS 2010 Conference in Lausanne. 1 ed. : CreateSpace, 2011, v. II, p. 127-134.

Conferences

1. M. A. B. Zanoni, M. F. Martins, H. Fonseca, F. S. P. Sisquini, *Smoldering Combustion in Oil Shale: Kinetics Parameters Estimation using Inverse Problems*, 21^{st} International Congress of Mechanical Engineering - COBEM, Natal - RN, Brazil;

2. F. S. P. Sisquini, M. A. B. Zanoni, M. F. Martins, *Microbial Reduction Contamination During biogasification Process: Estimating the Kinetic Parameters by Inverse Problems*, 21^{st} International Congress of Mechanical Engineering - COBEM, Natal - RN, Brazil;

3. M. F. Martins, M. A. B. Zanoni, E. N. Macedo, *Modeling the Thermochemical Conversion of Single Wood Particle*, 23^{rd} International Conference on Efficiency, Cost, Optimization, Simulation and Environmental Impact of Energy Systems - ECOS, Lausanne-Suisse.

4. M. A. B. Zanoni, M. F. Martins, H. Fonseca, F. S. P. Sisquini, *Applying Inverse Problem to Determine the Reactions Parameters for Oil Shale Combustion*, 13^{th} Brazilian Congress of Thermal Sciences and Engineering - ENCIT, 2010, Uberlândia - MG, Brazil.

5. F. S. P. SISQUINI, M. F. MARTINS, M. A. B. ZANONI, *Inativação de Microorganismos Patógenos Durante o Processo de Biogaseificação: Estimando os Parâmetros Cinéticos Pelo Problema Inverso*, PDPetro, 2011, Florianópolis. 6ºCongresso Brasileiro de Pesquisa e Desenvolvimento em Petróleo e Gás, 2011.

List of Figures

List of Tables

List of Abbreviations

Abbreviations

API	American Petroleum Institute
DSC	Differential Scanning Calorimetry
ESEM	Environmental Scanning Electron Microscopy
FC	Fixed Carbon
FD	Fuel Deposition
GA	Genetic Algorithm
HC	Hydrocarbons
HTO	High Temperature Oxidation
ICP	In-Situ Conversion Process
IM	Inert Material
IP	Inverse Problem
ISC	In-Situ Combustion
LM	Levenberg-Marquardt
LTO	Low Temperature Oxidation
MIS	Modified In-Situ
MSW	Municipal Solid Waste
NAPLs	Non-Aqueous Phase Liquids
ODEs	Ordinary Differential Equations
OM	Organic Matter
OP	Optimization Problem

OS	Oil Shale
PAHs	Polycyclic Aromatic Hydrocarbons
RSC	Reduced Sensitivity Coefficients
SC	Semi-Coke
STAR	Sellf-Sustaining Treatment for Active Remediation
STP	Standard Temperature Pressure
TG	Thermogravimetry
THAI	Toe to Heel Air Injection
TIS	True In-Situ
VM	Volatile Matter

List of Symbols

Nomenclature

A	Pre-exponential Factor
E	Activation Energy, $kJ.mol^{-1}$
fr	Quantity of carbon oxidized into CO or/and CO_2
J	Jacobian or Sensitivity Coefficients
k	Arrhenius Constant
M	Mass, *kg*
n	Reaction Order
P	Unknown Parameters
R	Ideal Gas Constant, $J.K^{-1}.mol^{-1}$
S	Objective Function
T(t)	Temperature Evolution in the time *t*
Y	Mass Fraction, *kg/kg*

Greek Letters

α	Stoichiometric Coefficient of Oxidation
β	Heating Rate, $K.min^{-1}$
δ	Radon Error
γ	Stoichiometric Coefficient of Decarbonation
μ	Damping Parameter
Ω	Diagonal Matrix
σ	Standard Deviation

Subscripts

f	Final
g	Gas
k	Iteration Number
l	Liquid
o	Initial
s	Solid
T	Matrix Transposition

Contents

Chapter 1

Introduction and Objectives

Unconventional energy sources - oil shale and its semi-coke, oil sands, extra-heavy oil and biomass from municipal solid waste and from sewage sludge - could be an alternative to reduce the current dependence on conventional fuels. In the last years, due to its high extraction costs, these sources have been underused. However, with the development of new techniques, the improvement of existing ones and the constant rise of oil prices, it has become viable and competitive.

Several technologies for unconventional fuels are available. However, only thermochemical technologies taking place in unconventional fuels are described here. Among them are surface retorting and in-situ retorting.

All these technologies have in common processes containing complex kinetic mechanisms composed of homogeneous and heterogeneous chemical reactions, where each one is controlled by the respective kinetic parameters.

In the literature, there are many numerical procedures aiming to determine the kinetic parameters. Nevertheless, they only may be used in kinetic pathways represented by one reaction step. Consequently, the development of robust numerical procedures, where is possible to use kinetic pathways with many reaction steps, is very important to predict all thermochemical reactions present in thermal decomposition processes.

Founded on the statements listed above, the objective of this work is to develop a methodology to obtain a new reaction mechanism for oil shale pyrolysis and for combustion of oil shale and its semi-coke that can be applied to computers modeling. Also, the kinetic parameters (Arrhenius parameters and stoichiometric coefficients) present in this reaction mechanism is estimated using a numerical procedure based on a robust optimization technique by inverse problems (Levenberg-Marquardt algorithm), while allowing the best agreement between predictions and experiments. After estimated, the kinetic parameters are applied in a numerical code in porous media where some parameters such as temperature profile, air velocity and fixed carbon concentration are analyzed and tested in a parametric study.

The present work is divided into seven chapters.

- In the second chapter the state of the art of the unconventional fuels and their extraction techniques are presented in details. A clear identification of the oil shale and its semi-coke as a solid fuel is made. In addition, a literature review of the kinetic mechanisms as well as the chemical reactions taking place in these fuels and a explanation about thermochemical processes (drying, pyrolysis, gasification, oxidation and decarbonation) involving reactions at particles and porous media are made in this chapter. Finally, it is presented the main methods to estimate the kinetic parameters.

- In the third chapter, it is presented the inverse problems technique, using the Levenberg-Marquardt algorithm. A detailed scheme for the iterative process and the algorithm is made along with a explanation about sensitivity matrix, sensitivity coefficients, objective function, stopping criterion and statistic errors.

- In the fourth chapter a formulation and a optimization of kinetic mechanisms for oil shale pyrolysis are presented. In this chapter, thermogravimetric analyze for an oil shale sample under heating rate of 10 $Kmin^{-1}$ is used to show the main chemical reactions taking place in a pyrolysis process. Also, a methodology to show the feasibility in the estimation process using sensitivity and determinant analyzes as well as the estimated parameters and the statistic errors are presented.

- In the fifth chapter, a formulation and optimization of reaction mechanisms for oil shale and its semi-coke combustion are presented. In this chapter, a new reaction mechanism is proposed and a comparison of the estimated parameters for two different oil shale samples under heating rates of the 3 $Kmin^{-1}$ and 10 $Kmin^{-1}$ is made. For the semi-coke, the sample is subjected to a heating rate of the 3 $Kmin^{-1}$. The sensitivity and determinant analyzes as well as statistic errors are made for each case.

- In the sixth chapter, it is presented a test case for the reaction mechanism proposed for semi-coke combustion using the estimated parameters. The kinetic mechanism is applied in a 1D numerical code in porous media developed by Martins et. al. [16] where a parametric study is made to show the dependence between temperature profile, air velocity and fixed carbon concentration. In addition, the front velocity is evaluated.

- In the last chapter, it is presented the work conclusion along the final comments and future perspectives.

Chapter 2

State of the Art

In this chapter is presented a literature review of some unconventional fuels and thermochemical processes taking place in their extraction technologies to produce energy. In addition, two unconventional fuels - oil shale and its semi-coke - is chosen as a fuel model and a literature review of the reaction mechanisms and their parameters estimation methods is made.

2.1 Unconventional Fuels for Power Generation

Unconventional fuels resources could be an alternative to reduce the current dependence on conventional fuels. They can be classified in two groups: fossil and residual. Regarding to the fossil unconventional fuels, they are those were discovered (there is information about site, scale of reserves and amount of oil and gas that is possible to recovery) but due to their geological and rheological characteristics, they require alternative technologies whose production cost is generally higher than the cost of conventional oil. About the residual group - organic, thermoplastic, thermoset and elastomer materials - they can be used to produce flue gas in gasification plants or to produce energy burning in combustion processes. In the last years, both fossil as well as residual groups have been underused. However, with the development of new techniques, the improvement of existing ones and the constant rise of oil prices, it has become viable and competitive.

Thus, there are many varieties of unconventional fuels. However, in this work is described only those that have had a big rise in recent years due to the environmental problems and the energy production such as oil shale and its semi-coke, oil sands, extra-heavy oil and biomass from municipal solid waste and from sewage sludge.

The oil shale can be defined as a sedimentary rock consisting of a mineral porous matrix filled with oil called kerogen, Figure 2.1(a), representing 10-65% of the total mass, with ash content exceeding 33%. This mineral matrix is consisted mainly of carbonates (20-70%) and 15-60% of the quartz, feldspars and clay [17, 18, 19]. When exposed to heating processes, oil shale leaves a solid waste material, called semi-coke.

(a) Oil shale [20] (b) Semi-coke [21]

Figure 2.1: Deposits of oil shale and its semi-coke.

The semi-coke from oil shale is characterized by a considerable content of carbon (10-12%), by a low volatility and by a high content of mineral matter (60-70%) [22, 23]. Currently, it is considered the main cause of the environmental problems in the oil shale industry, Figure 2.1(b), because the cost of its disposal is very expensive. Its posteriori treatment has recently attracted interest of many researches [22, 24]

Oil sands, Figure 2.2, are composed of sand, silt, clay, water and about 10%-12% bitumen (organic matter). They present a dark color, Figure 2.2(a), and a strong hydrocarbon smell. The technical term for the oil extracted from oil sands is crude bitumen, a type of extra heavy oil which is defined as a viscous mixture of hydrocarbons that, in its natural state, does not flow easily [25, 1]. The oil sands deposits are shown in the Figure 2.2(b).

Concerning to the extra-heavy oils, they are characterised by their high density (according

(a) Oil Sands (b) Oil Sands deposits

Figure 2.2: Deposits of Canada's oil sands in Alberta [1].

to Martinez et al. [26], with API $<10^{o}$), high viscosity, and high concentrations of nitrogen, sulphur, oxygen, and heavy metals [27]. When exposed to heating process, its high viscosity decreases and then, it is possible to flow easily.

Regarding to the biomass from Municipal Solid Waste (MSW), Figure 2.4(a), and from sewage sludge, Figure 2.4(b), the organic matter presents in these fuels can be used to produce energy. MSW consists of miscellaneous organic and inorganic wastes from residential and industrial sources. According to the Center for Sustainable Systems of University of Michigan [3] and the U.S. Environmental Protection Agency [2] the composition of the MSW is according to the Figure 2.3. It is important to know that its composition depends on the locality and the population habits. The main problems caused are the health risks, due to the amount of contaminants and the environmental degradation caused by uncollected domestic refuse in streets and open areas, urban drainage systems that have become clogged by indiscriminately dumped refuse, and the pollution of water resources near to uncontrolled dumping sites [28].

About the sludge, it is the residual left from industrial wastewater or sewage treatment processes, where its composition depends on the area where it is collected and population habits among others. Sludge contains organic matter, nitrogen, phosphorus, potassium, calcium, sulphur and magnesium and pollutants divided between heavy metals, organic pollutants and pathogens [29]. According to Inoue et al. [30] a basic composition of the sludge involves about 84% of moisture content and in relation to the organic content, 33.4% are protein, 6.6% are lipid and 3.3% are carbohydrate on an organic basis. To eliminate the contaminants, some

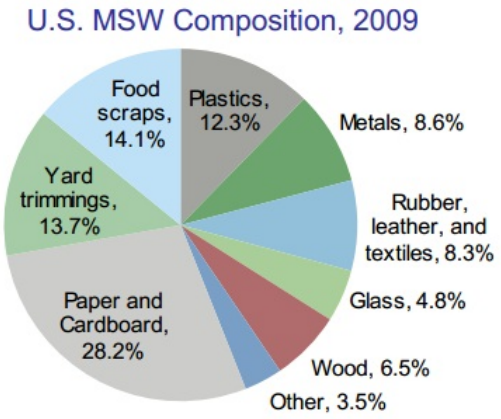

Figure 2.3: Main composition of the MSW [2, 3].

thermochemical treatment processes, such as gasification, can be used and moreover, due to their reasonable amount of organic matter, they still may be used to produce energy.

(a) Municipal Solid Waste [31]

(b) Sludge from wastewater [32]

Figure 2.4: Two examples of the residual group where the organic matter can be extracted.

2.2 Technologies for Unconventional Fuels

Several technologies for unconventional fuels are available. In this work, only some thermochemical technologies are described. Among them: - surface retorting reactors available for oil shale and oil sands pyrolysis, semi-coke combustion (sintering processes in cement plants) and gasification processes for biomass; - in-situ self-sustaining smoldering combustion in porous media for oil shales, oil sands, extra-heavy oil and Non-Aqueous Phase Liquids (NAPLs) - coal

tar, creosote, petroleum, hydrocarbons, diesel range organics, oils and greases, mineral oil and oil mixtures [9, 33, 34];

2.2.1 Surface Retorting

Oil shale and Oil Sands Retorting

The first thermochemical process analyzed is the surface retorting for oil shale pyrolysis, semi-coke combustion (sintering processes in cement plants) and gasification processes for biomass. More specifically about oil shales, Figure 2.5 shows an overview of the processes involved in their exploitation and their main products and residues. In relation to the surface retorting, basically, this process includes three steps: mining of the oil shale and ore preparation, thermal processing or retorting processing of the shale oil to obtain a refinery feedstock and value-added by-products. Mining of the oil shale involves large impact on the environment also resulting in important investments in waste disposal and site reclamation. About in-situ techniques, oil shales can be mined or not and the heating process takes place underground. The products of pyrolysis (oil and gas) are pumped to the surface and depending on the type of kerogen and the underground heating process, the recovered oil has to be treated and improved before further refinement or may be directly used as a refinery feedstock [4, 5].

Surface retorting process can be classified into direct heating mode (particulates) and indirect heating mode (lump). Many countries have developed several retorting technologies, such as Kiviter retort in Estonia, Petrosix retort in Brazil, Paraho retort in USA and Fushun-type retort in China available for oil shales; and Taciuk retort in Canada available for oil sands and oil shales [6, 35, 36, 37]. Figure 2.6 shows the Paraho retort using direct and indirect heating mode respectively [6].

In direct heating mode, Figure 2.6(a), the mined fuel enters through the top of the retort and it moves vertically when it is heated to pyrolysis temperatures by a rising stream of hot combustion gases. Oil and gas, produced by pyrolysis reaction, are collected by tubes and released in a product separation equipment. As the fuel approaches the burner bars, the fixed

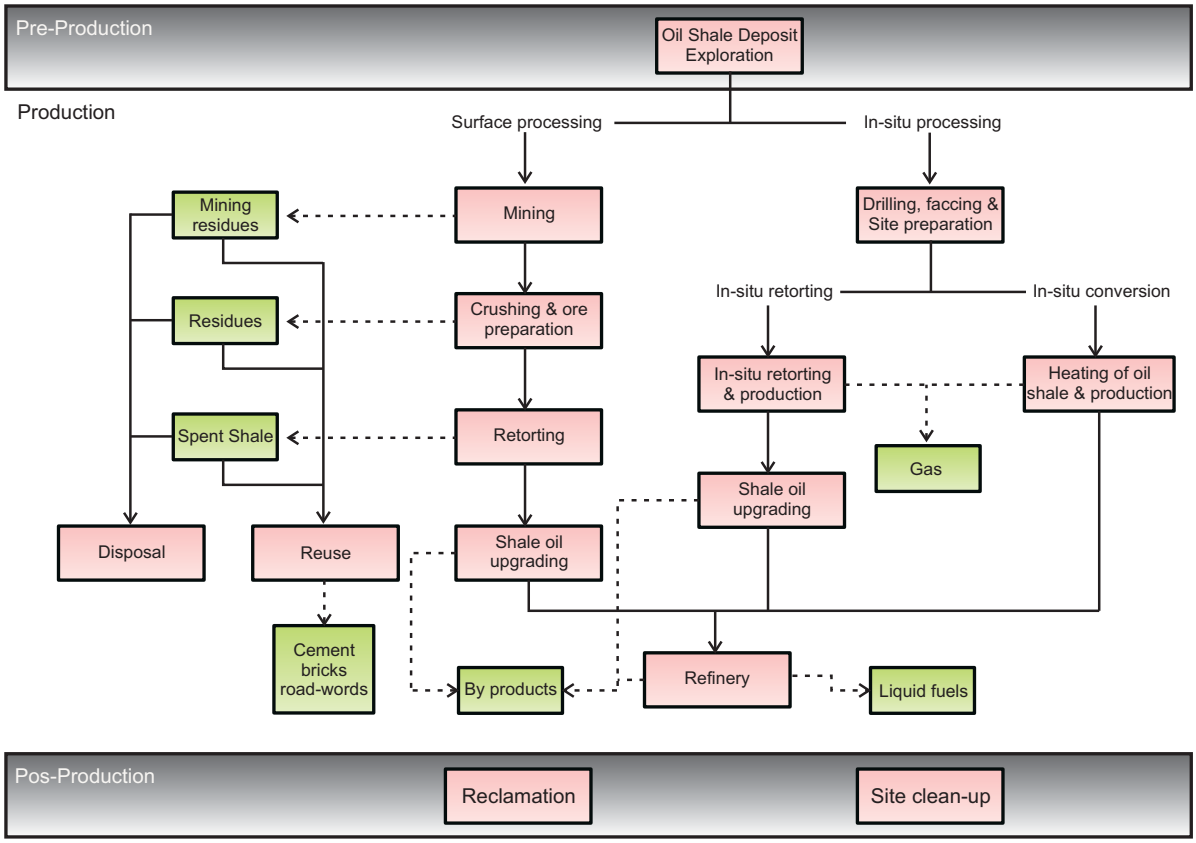

Figure 2.5: Overview of the processes involved in the oil shale exploitation and of the main products and residues, [4, 5].

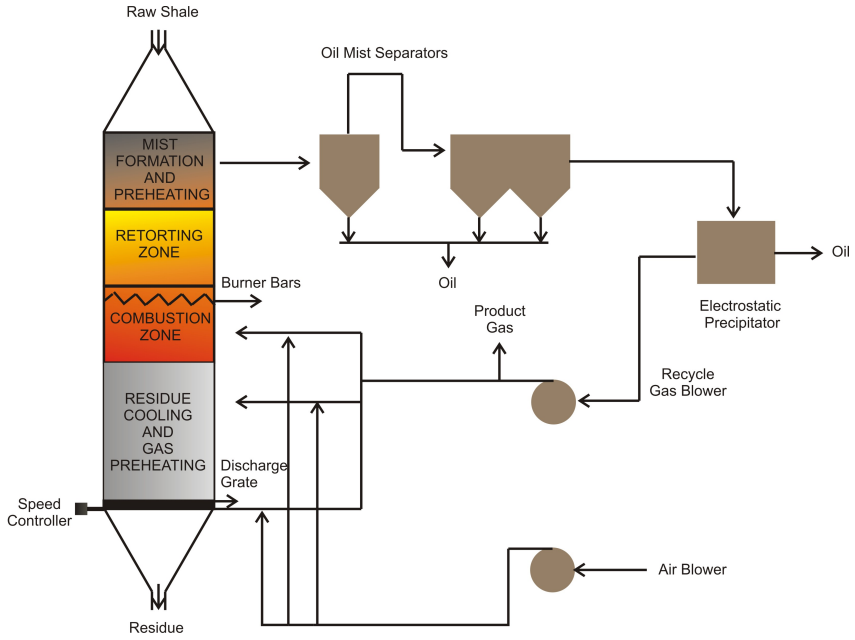

(a) Direct heating mode

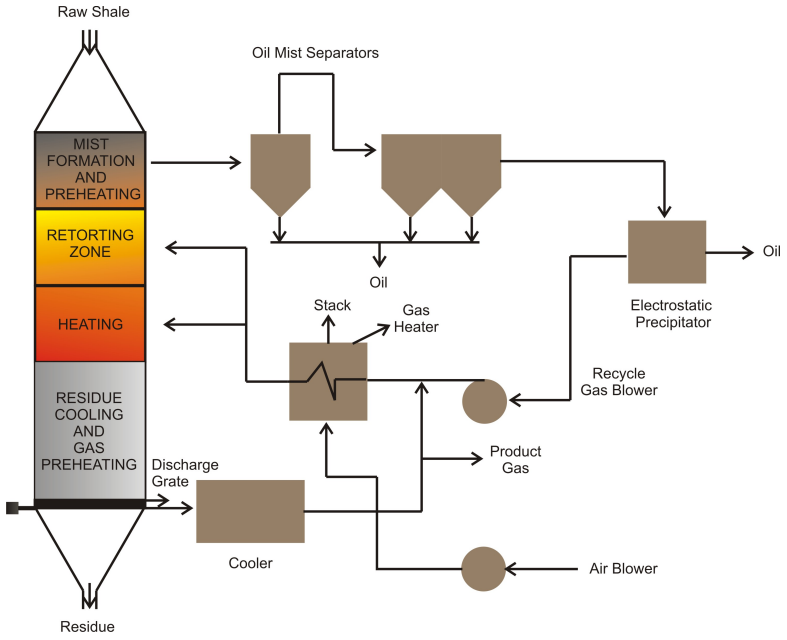

(b) Indirect heating mode

Figure 2.6: Schematic retorting plant using direct and indirect heating mode [6].

carbon still contained in the retorted fuel is ignited and gives off the heat (by oxidation reaction) required for pyrolyzing additional raw fuel. Thus, it is cooled in a stream of recycle gas after passing beyond the burner bars and leaves the retort through the discharge grate.

In indirect heating mode, Figure 2.6(b), the process is similar to the direct mode except that air is not injected and the off-gas steam is divided into four distinct flows after oil separation. One part of off-gas steam is composed of the net product gas and another is sent through a reheating furnace and then reinjected into the middle of the retort. A third part is reheated but this part is not reinjected in the bottom of the retort. Finally, the fourth part is used for fuel in the reheating furnace. There is no combustion occurring in the retort and all heat for kerogen pyrolysis is provided by the reinjected gases. Petrosix retort as well as Paraho retort can be described in this classification, [6].

Cement Plants (Semi-Coke Combustion)

The semi-coke is considered the main cause of environmental problems in oil shale industry. Residual organics present in the semi-coke contain phenols, PAHs (Polycyclic Aromatic Hydrocarbons) and oil products that are potential pollutants with harmful environmental effect [23]. A feasible solution to reduce the environmental impacts is to take its high residual energetic potential burning it as feedstock for power generation [38] in retorting processes. Another possibility could be the production of carbon-rich materials in order to obtain, for example, activated carbon from semi-coke [22]. Besides, it can be used as ash-based cement and binding agents, autoclave hardened shale ash bricks, glass ceramic and heat insulating materials as well as filling agents to replace chalk in rubber fillings. Methods for utilizing ash in road construction for consolidation of earth and materials, when constructing base of roads, as well as neutralizing agent in production of fertilizers and in agriculture for chalking acidic soils have been worked out [38].

However, only the use of semi-coke as a feedstock in cement industries is presented here. Semi-coke has been mixed in the amount of 10 to 30% in Portland cements [22] because it has high amount of SiO_2 and CaO which has cementitious properties on its own [24]. Also, it

produces heat, resulting in the reduced heat consumption in the process of calcination.

The raw material, in the form of a slurry - mixture of Portland cement and semi-coke - enters in a rotary kiln, Figure 2.7(a), where undergoes some thermochemical reactions, Figure 2.7(b). These reactions can be considered as:

- drying - water evaporation;
- calcining - loss of carbon dioxide from limestone;
- sintering - fusion of particles creating one solid mass.

After that, due to the inclination of the kiln, the hot clinker drops out and cools [7]. Thus, this destination given to the semi-coke helps to provide heat to the process in cement plants, being very useful and reducing the environmental impact.

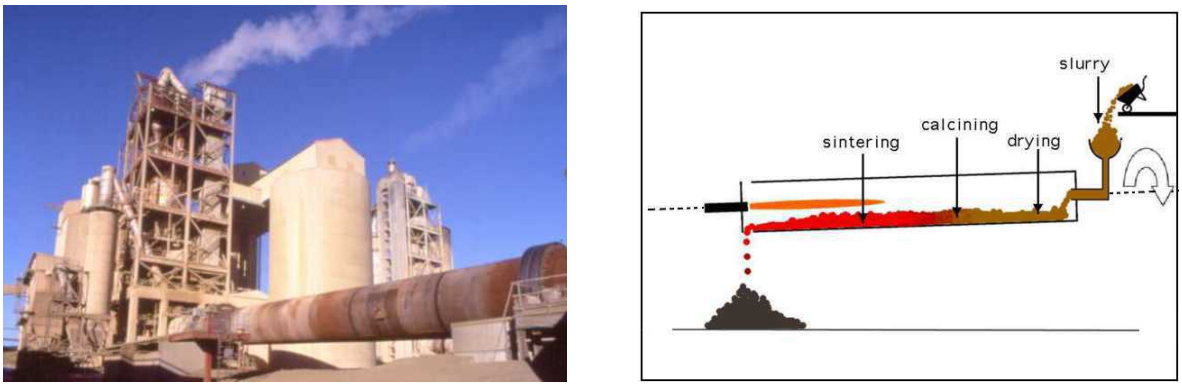

(a) Rotary Kiln (b) Thermochemical Reactions

Figure 2.7: Thermochemical reactions taking place in a rotary kiln [7].

Biomass Gasification - Municipal Solid Waste and Sewage Sludge

Gasification has proven to be an attractive alternative for the treatment of municipal solid waste and sewage sludge to reduce mass and decrease the environmental impact [39]. Gasification is a thermal conversion process in which both heat and flue gases are produced. One method of gasification refers to the partial oxidation of the fuel in presence of an oxidant amount lower than that required for the stoichiometric combustion. Basically, part of the fuel mass is

burned to provide heat needed to gasify the rest. In a second method, the biomass is indirectly heated in the absence of oxygen or air, with steam as the oxidizing agent [40, 41].

The gasification process occurs in a gasifier, Figure 2.8(a), where take place some thermochemical reactions such as drying, pyrolysis, oxidation and reduction reactions, Figure 2.8(b).

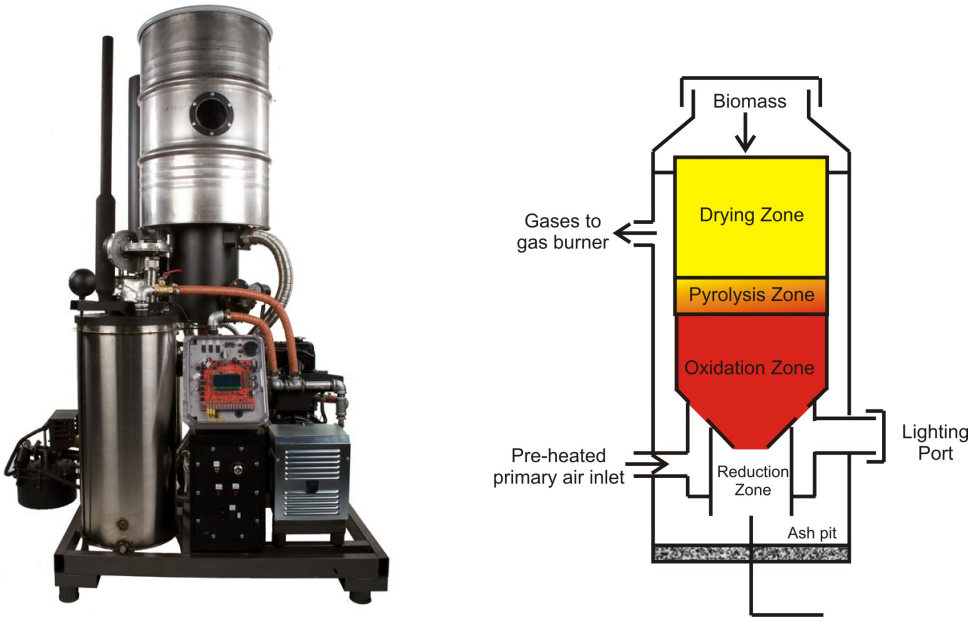

(a) Gasifier Experimenters Kit (GEK) [42] (b) Thermochemical Reactions [43]

Figure 2.8: Thermochemical reactions taking place in the gasifier.

In the drying reaction, water is evaporated at temperatures up to about 160 ^{o}C [41]. After drying reaction, pyrolysis of organic matter takes place producing large quantities of tar and gases containing carbon dioxide [44]. The oxidation reaction occurs in the solid fuel, where an exothermic reaction takes place producing energy and releasing carbon dioxide and carbon monoxide. Finally, in the reduction reaction, a number of high temperature chemical reactions take place in the absence of oxygen, where the solid fuel is burned or reduced to carbon monoxide.

2.2.2 In-Situ Self-Sustaining Smoldering Combustion

Oil Shale In-Situ Processes

Smoldering combustion can be defined as a slow, low-temperature, flameless form of combustion, sustained by the heat released when oxygen directly attacks the surface of a condensed-phase fuel [45, 46]. Thus, based on this definition is possible to show the in-situ self-sustaining smoldering combustion, available for oil shales, oil sands, extra-heavy oil and NAPLs. In this process, small fraction of the fuel in the reservoir is burned and a combustion front is sustained by injecting air or an oxygen rich gas, decreasing the viscosity of the unburned fuel fraction and increasing oil recovery, [11]. Regarding to the oil shales, some in-situ self-sustaining smoldering combustion processes can be used: True In-Situ process (TIS) [6], Modified In-Situ process (MIS) [6] and Shell's In-Situ Conversion Process (ICP) [4, 47].

TIS processing consist in, as a first step, makes a dewatering the deposit, if it contains a reasonable amount of water. After that, the oil shale is fractured by explosives to increase the permeability and then it is heated in the underground by injecting hot fluids to provide heat for pyrolysis. The last step is recover the oil and gases through wells. The mining is not needed in the TIS processing, and waste disposal is minimized due to few disturbances on the surface. However, it has low recovery of the shale oil and moreover, the spent shale may contaminate the groundwaters.

Same procedure is used in MIS processing, except that, in this case, the oil shale is mined and after it is fractured by explosives to increase the permeability. This technique can be used in large deposits and relatively few surface facilities are required. However, it generates an accumulation of solid waste on the surface and as well as in TIS processing, occurs a low oil recovery and also the spent shale may contaminate the groundwater [6].

Concerning to ICP, this process consists of four main steps [47]. First, a freeze wall is created to prevent groundwater from flowing into the heating process, and second to contain the ICP products. After, oil shale is heated using electric resistance heating. The heat moves slowly through the formation, heating the oil shale to the temperature of kerogen decomposition.

The next step is the pumping the hydrocarbons produced to surface. Finally, hydrocarbons are flushed and the freeze wall is thawed. ICP is more environmentally friendly and more efficient than previous in-situ combustion technologies because the conventional mining is not used, and consequently, almost there is no tailing from them on the surface, moreover uses less water in the process.

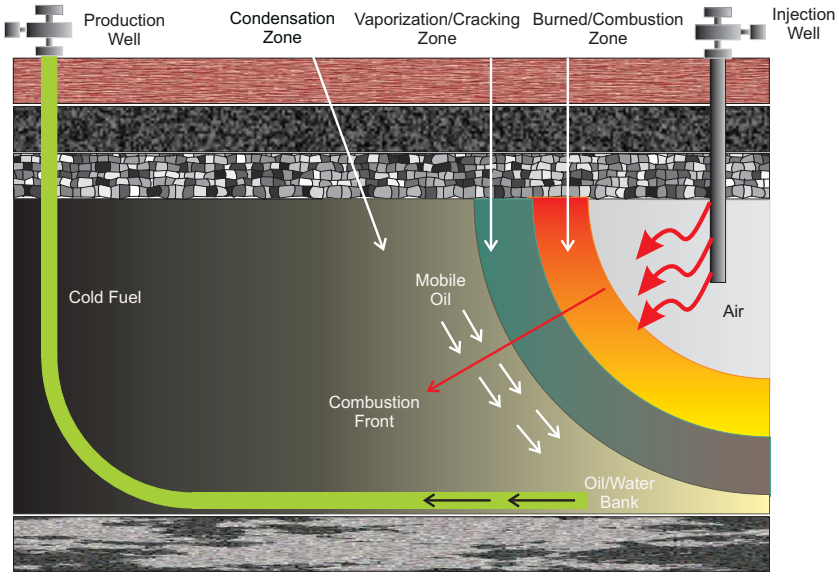

Figure 2.9: Schematic section of the THAI in-situ combustion process in a deposit of fuel [8].

Toe to Heel Air Injection (THAI)

Toe to Heel Air Injection process (THAI), [8], Figure 2.9, is available for oil sands and extra-heavy oil. This process combines in-situ combustion and horizontal well technology, used instead of a vertical well, employed in conventional in-situ combustion. In vertical configurations, it is placed towards of the oil layer top, while in horizontal configurations, it is placed in the bottom of the reservoir. After the combustion front becomes *anchored* into the *toe* of the horizontal well, it then propagates steadily, along them, from the *toe* to the *heel* position [8].

Self-Sustaining Smoldering Treatment for Active Remediation (STAR)

STAR, Figure 2.10, is a new technology to remediate Non-Aqueous Phase Liquids (NAPLs). NAPLs are a class of organic compounds - coal tar, creosote, petroleum, hydrocarbons, diesel range organics, oils and greases, mineral oil, and oil mixtures - with a long history of extensive use in industrial processes [48, 9] causing environmental contaminants (groundwater and soil) due to its inappropriate disposal practices. Thus, it uses smoldering combustion to remediate NAPLs because this process destroys contaminants quickly and efficiently [48]. Regarding to the unconventional fuels, STAR can be used to remediate final residues created by retorting processes and in-situ combustion that, in the most of the cases, are deposited in the environmental, contaminating the soil and the groundwater.

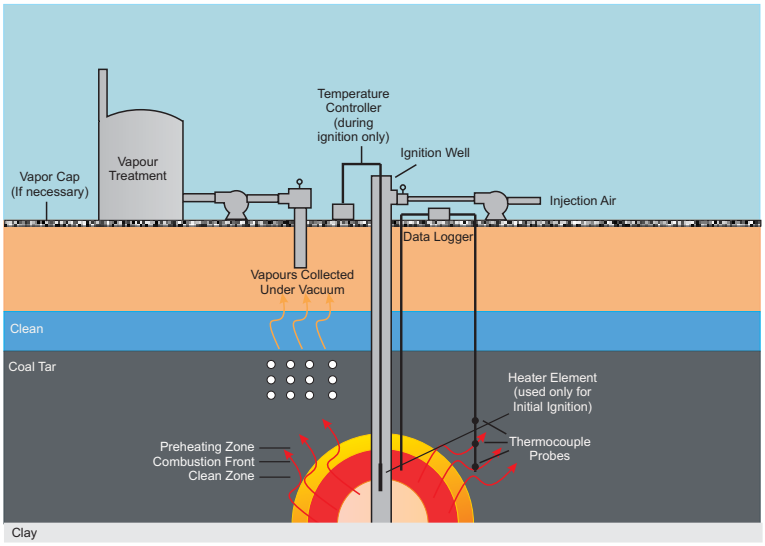

Figure 2.10: Elements of an In Situ STAR Pilot Test [9].

STAR process, Figure 2.11, starts by inserting a heating element into the target treatment zone, Figure 2.11(b). A short duration input of energy is then applied to heat the NAPL adjacent until its heating ignition temperature. Once this temperature is attained (typically between 200 and 400 ^{o}C), air is injected to ignite the NAPL. The NAPL combustion, releasing heat energy which is retained by the porous medium and used to pre-heat NAPL farther away from the ignition point. At this stage, the heating element can be turned off, Figure 2.11(c), and as long as sufficient air is supplied, the combustion process continues propagating away from the air

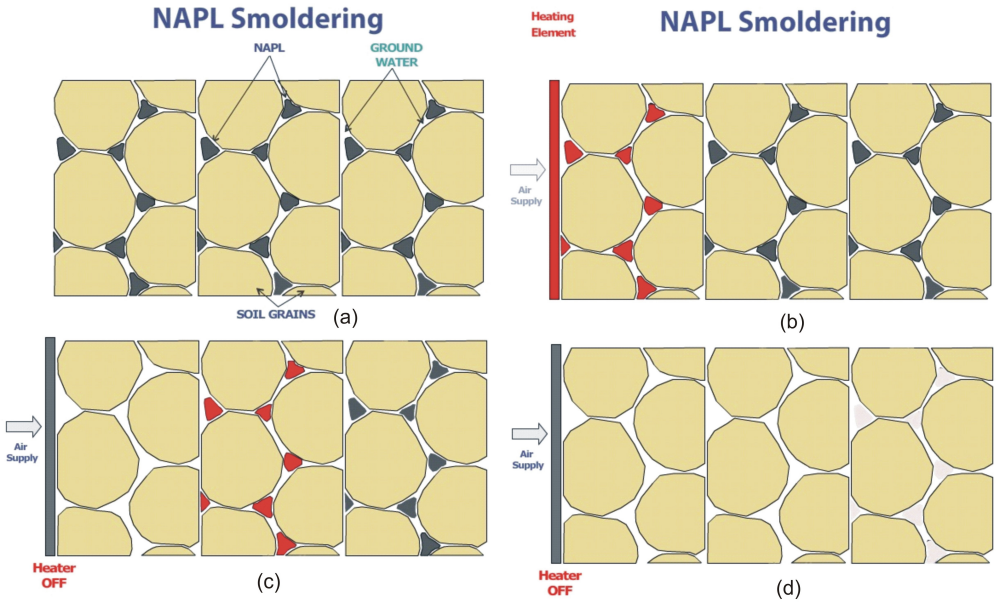

Figure 2.11: NAPL smoldering remediation process [9].

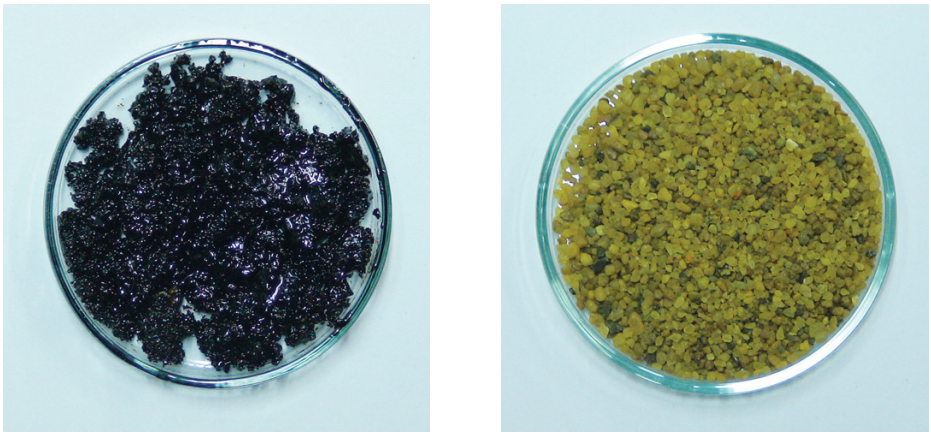

(a) NAPL before STAR (b) NAPL after STAR

Figure 2.12: Examples of the NAPL remediation by STAR [9].

injection point [9]. After that, Figure 2.11(d), all NAPLs were eliminated. The result of STAR process is presented in the Figure 2.12. Figure 2.12(a) shows a portion of sand with NAPL before the STAR process. After the STAR process, Figure 2.12(b), around 95 to 99.99% of the NAPLs were eliminated [9].

2.3 Oil Shale and its Semi-Coke as a Fuel Model

The oil shale and its semi-coke have many characteristics that provide their choice as a fuel model. From a scientific point of view, their kinetic mechanisms to propagate a combustion front involve chemical transformations in the bed as well as heat transfer (due to the high temperature elevation) and the gas flow in the porous bed, with strong couplings. Because of these coupled mechanisms, the structure of a combustion front is complex and can vary depending on a large number of parameters. Such questions are still not fully understood.

The structure of a combustion front and the chemical reactions that happen during its propagation involve smoldering phenomena [45, 46, 49]. According to Aldushin et al. [10] and Martins [12], three distinct processes of travelling combustion front structures can be identified. Figure 2.13, presented by Aldushin et al. [10], shows a scheme to illustrate the three combustion structures.

The first one, Figure 2.13(a), where the combustion zone precedes the heat transfer zone, in which the solid gives up heat to the incoming cold fresh gas, to carry it into thermal equilibrium with the solid. Since the processes in two zones are independent, each progress with its own velocity. In this type of structure the reaction zone runs faster and therefore ahead of the heat transfer zone; this type of structure is called *reaction leading structure*. The second called *reaction trailing structure*, Figure 2.13(b), the heat transfer zone precedes the reaction zone. Experimental observations of both cases, presented superadiabatic effect. The last case, Figure 2.13(c), separates the two structures and corresponds to a combustion temperature T_b which is infinite, i.e. solutions in form of travelling combustion front are no longer possible - travelling combustion front analysis breaks down. However, this situation corresponds to conditions where the superadiabatic effect manifests itself most strongly.

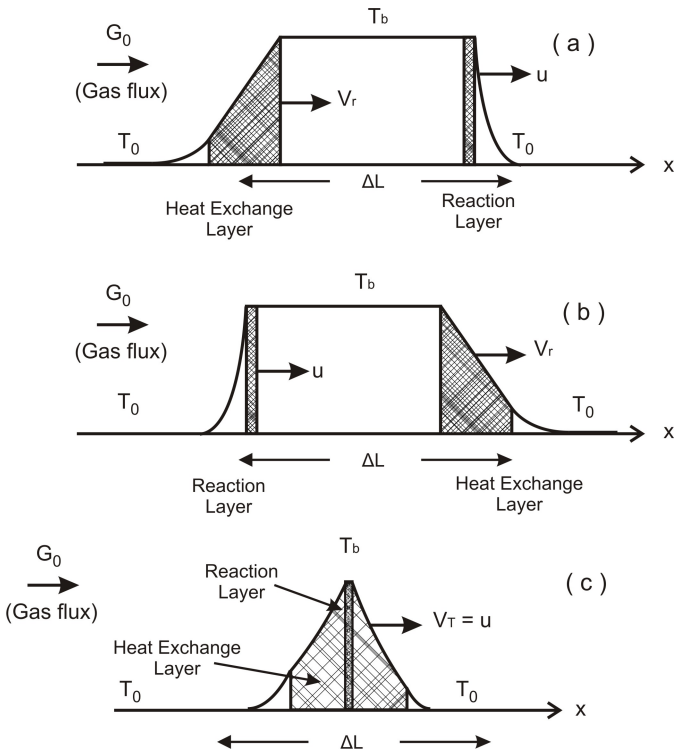

Figure 2.13: Forward front of combustion: (a) reaction leading structure; (b)reaction trailing structure; (c) wave with maximal energy accumulation [10].

Concerning to the smoldering velocity, theoretical models developed by Schultz et al. [50] and by Johnson et al. [51] for forward smoldering propagation have shown that the smoldering velocity depends on the oxygen fraction, entry air velocity, energy released in the combustion process, heat flux from the igniter and the physical properties of the porous media.

Torero and Fernandez-Pello [52], have studied the forward smoldering combustion using air as oxidizer. The objective was to provide further understanding of the mechanisms controlling forward smoldering and verification of theoretical models of the problem. Upward and downward forward smoldering were compared to also observe the effect of buoyancy on the process. Buoyancy was observed to affect this mode of smoldering at very low air velocities, or when the smoldering front approaches the sample end. However, the theory shows a good agreement with the experiments. The main conclusion of this work was that smoldering is controlled by the heat transfer from the oxidation reaction to the adjacent material, and the mass transfer of oxidizer to the reaction. In other words, the smoldering front propagation only depends on the fuel and the oxidizer.

In addition, further describing in a scientific point of view, a significant advantage of an oil shale used as a porous medium bed to study the propagation of a combustion front is that the bed preserves its geometry during the front evolution, allowing a 1D formulation. This is a very important motivation for using oil shale as a fuel model.

Martins et al. [16] have developed a new 1D experimental device in a fixed bed, where the front propagates as a plane and horizontal surface while using oil shale the front propagates as an inclined curved surface. The oil formed during the pyrolysis is adsorbed in the porous medium in the course of the experiment, and expelled from the cell by the end.

Regarding to the geometry preservation, Martins et al. [13] noted that for particles in the size range 500-1000 μm, the oil shale remains constant when the heating rate is varied between 50 and 900 $Kmin^{-1}$. According to Martins [12], such behavior is due to the association of the organic matter with the mineral matrix.

From an application point of view, propagating a combustion front in a particle bed of oil shale is a way to recover part of the oil contained in its structure. The oil recovered can be used

as a petroleum like liquid. Moreover, the flue gas that is produced may prove interesting as a source of energy. The combustion of oil shale can be made in-situ or in surface retorting after mining.

Martins et al. [13] provides a detailed chemical characterization of Timahdit oil shale and of its smoldering combustion products. The amount of fixed carbon formed during devolatilization is measured at 4.7% of the initial mass of oil shale where its combustion was operated using a mix of 75/25 wt.% of oil shale/sand. Approximately 52% of the organic matter from oil shale is recovered as liquid oil. The front decarbonated 83% of carbonates.

Sennoune et al. [53] have analyzed the influence of CO_2 emission when the oil shale reaches high temperatures required to activate the decarbonation reaction of the oil shale in a smoldering combustion packed bed. According to the authors, this phenomenon has caused 70% of the CO_2 emissions and the other 30% was resulted from the fixed carbon oxidation. In order to decrease the temperature of combustion front and to avoid the decarbonation reaction, experimental tests carried out aiming to increase the amount of carbonates and decreasing the amount of fixed carbon in the medium. The results have shown that increasing the amount of carbonates may only decrease the front temperature up to 800 ^{o}C, i.e. still too high to avoid decarbonation reaction. On the other hand, reducing the amount of fixed carbon, was observed the decreasing of the front temperature avoiding almost completely the decarbonation.

Jiang et al. [54] have shown a new utilization system for oil shale where it is composed of three subsystems: retort subsystem, combustion subsystem and ash processing subsystem. In the first subsystem, oil shale particles (8-80 mm) were retorted resulting into shale oil, hydrocarbon gases and oil shale semi-coke. In the combustion subsystem, the semi-coke and fine oil shale (0-8 mm) were fed to a circulating fluidized bed furnace to burn. Finally, in the processing subsystem, the oil shale ash from the circulating fluidized bed furnace was utilized to produce building materials. This system has presented lower pollutants emission and energy loss, more diversified products and a higher utilization efficiency of oil shale resources.

Lee and Sohn [55] have determined experimentally the ignition characteristics of a bed of broken oil shale. Also, a mathematical model was developed to describe the ignition process and the effects of the flow rate and the retorting gas composition, the size and the grade of

the shale pieces on the minimum time and energy required to attain a self-sustaining retorting front were determined by a nonisothermal experimental method. The ignition time decreased and the ignition energy increased with increasing flow rate of air, both increased with shale particle size and both decreased with increasing shale grade and oxygen partial pressure. In this experiment the ignition process was controlled by the gas-solid heat transfer, the oxidation of light hydrocarbons liberated from kerogen, kerogen decomposition kinetics, and shale particle size.

Regarding to the semi-coke, is possible to produce energy burning the fixed carbon presents in its composition. The utilization of the semi-coke involves both scientific and application point of view. For scientific point of view, as the semi-coke is the pyrolyzed oil shale, there is no organic and volatiles matter in its composition. Thus, it is known that all the heat released in the combustion process is due to the fixed carbon oxidation.

For application point of view, the semi-coke can be used in cement plants to produce energy. Smadi and Haddad [24] have studied the effects of its utilization. In their investigation, mortar and concrete mixtures were prepared at different rations of water, oil shale ash and sand. The compressive strength of mortar and concrete mixtures, was determined using different curing periods. A mathematical model was developed to describe the effect of constituents on the strength developments of oil shale ash mortars and concretes. The models' accuracy was checked by comparing the numerical results with experimental results. In addition, the oil shale ash replacement of cement, sand or both by about 10 wt.% would yield a optimum compressive strength, and that its replacement of cement by up to 30 wt.% would not reduce significantly its compressive strength. It was found that oil shale ash contains a limited cementitious value and its contribution to mortar or concrete is due to the involvement in pozzolanic reactions.

Vasalos et al. [56] have used a fluid bed combustor, applying two-phase theory of fluidization, to burn the semi-coke residue that remains in the inorganic matrix during pyrolysis process. The carbon burning efficiency was calculated as a function of temperature, pressure, and bubble size. The carbonate decomposition and the associated energy loss were also established using the same conditions. As a results, the authors have shown that a complete carbon combustion is feasible and presents a minimum carbonate decomposition.

According to Trikkel et al. [22], the high potential of residual energy of the semi-coke could be used in a circulating fluidized bed combustion. The additional heat produced and the main parameters of combustion process were calculated and verified by combustion tests in a fluidized bed device. The authors, in their experiments, have shown that a semi-coke containing low moisture may be burnt directly in fluidized bed and those with over 10% moisture content, about 10% of oil shale must be added. Moreover, the possibilities to utilize the fixed carbon present in the semi-coke to obtain activated carbon also was discussed. As a result, the separation of carbon-rich ingredients did not worked as expected, due to close integration of mineral and organic part of the semi-coke. Consequently, the failure to obtain products rich in carbon resulted in failure to obtain activated carbon.

2.3.1 Reaction Mechanisms

All these technologies presented previously have in common thermochemical processes that involve reaction zones composed of complex mechanisms of chemical reactions. Various simultaneous and parallels (homogeneous and/or heterogeneous) reactions take place in these kinetic mechanisms. An analyze more detailed about these reaction zones may be made for oil shales and its semi-coke using the example of retorting technologies and the in-situ combustion.

Thermochemical conversion involves processes with high temperatures and generally high pressures. As the temperature increases, several reactions are established producing elements in gas, liquid and solid phases, with or without energy generation. For oil shale and its semi-coke, this process can be defined into drying, pyrolysis, gasification, oxidation and decarbonation reactions.

Drying reaction or also so called pre-heating reaction may be consecutive and overlapping where only physical processes are involved such as heat and mass transfer. Some authors refer to the pre-heating reaction as a simple ignition process, where the focus is only on the body surface to obtain a time estimation of the thermochemical processes [57, 58].

Pyrolysis reaction is defined as thermal degradation (chemical changes) occurring when heat is applied to a fuel in the absence of oxygen. For oil shales, in the pyrolysis reaction takes

place degradation of organic matter releasing flue and non flue gases and water, and producing fixed carbon. The products depend upon temperature, pressure, residence time and heat losses [44].

Gasification reaction, as explained previously, occurs with partial oxidation in the presence of steam resulting in production of combustible gases where they can be used to run internal combustion engines [44]. Concerning to the oil shale, the gasification is a process that requires extraction of volatile components through pyrolysis, followed by partial oxidation of the remaining fixed carbon. This set of reactions produces flue gases together with small amount of other gases [59].

Oxidation is an exothermic chemical reaction where heat is released in the presence of air or pure oxygen. The fuel is usually composed of elements such as carbon, hydrogen and oxygen. In complete combustion, carbon dioxide is obtained from fixed carbon in the fuel, and water is obtained from the hydrogen, usually as steam [44]. About oil shale oxidation, oxidation reaction occurs due to the presence of fixed carbon produced in the pyrolysis reaction. This reaction released carbon monoxide, carbon dioxide and heat.

Decarbonation reaction is endothermic and occurs due to decomposition of $CaCO_3$ and $MgCO_3$ releasing CO_2, CaO and MgO. In the case of oil shales and its semi-coke presented here, the carbonates were established only composed of $CaCO_3$. Regarding to the amounts of CO_2 formed, it can be established for this mass balance that CO_2 from decarbonation of $CaCO_3$ represents 69% of the total CO_2 emissions [13], i.e. including CO_2 from fixed carbon oxidation. Consequently, decarbonation reaction has a strong environmental impact in terms of CO_2 emissions.

The Figure 2.6 presented previously shows the reaction zones taking place in retorting technologies. This figure was reformulated, and it is exhibited in the Figure 2.14, to show only the retorting reactor for both direct and indirect heating mode.

For the direct heating mode, four zones are identified: preheat zone, retorting zone, combustion zone and spent shale zone. In this configuration, the air flow is reinjected into the middle of the retorting reactor. The raw oil shale enters through the top of the retort being heated. In

this zone, occurs the water evaporation. After, it moves vertically until the retorting zone when it is heated to pyrolysis temperatures. In this zone, occurs the organic matter conversion releasing gaseous hydrocarbons and fixed carbon. In the combustion zone, fixed carbon is oxidized giving off heat required for pyrolysis of raw fuel. The last zone contains spent shale formed in the combustion zone.

In the indirect heating mode, the main difference is that the potential heat of fixed carbon contained in the shale coke is not utilized, influencing the thermal efficiency of the retort [35].

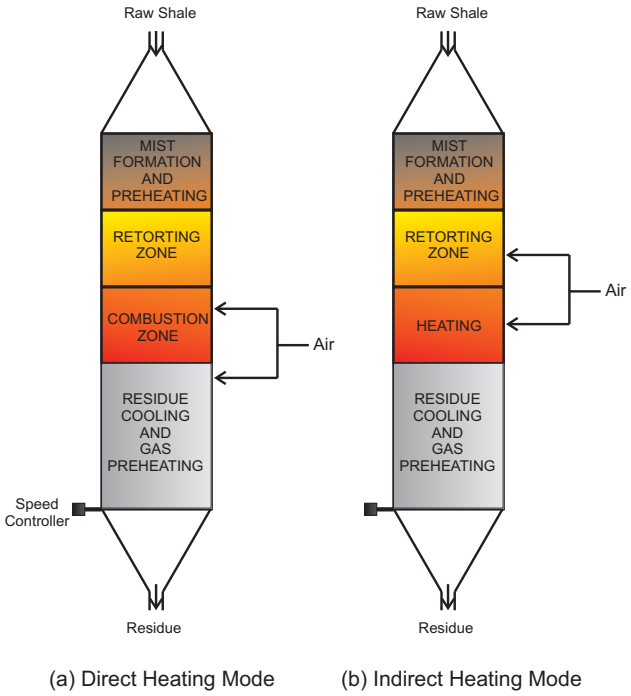

Figure 2.14: Schematic retorting reactor showing the main reactions taking place in the retorting technologies [6].

In relation to the in-situ combustion, Figure 2.9 and Figure 2.15 show seven reaction zones taking place in this process: burned zone, combustion zone, cracking/vaporization (coking) zone, condensation zone, water bank zone, oil bank zone and native zone [11, 60].

In the burned zone, the temperature increases toward combustion front. This zone may contain some residual unburned organic solid (fixed carbon). In the combustion zone occurs the highest temperature levels due to the reaction between oxygen and fuel, generating heat, water and combustion gases (CO_2 and CO). In the coking zone, the fixed carbon is formed and it

is used as fuel for combustion zone. The high temperature generated by combustion reactions causes fuel devolatilization resulting in the production of CO_2, organic gases, hydrocarbon and char. In the condensation zone, the hydrocarbon vapor are condensed and dissolved in the crude. This zone contains steam, oil, water and flue gases. The zones containing banks are just an accumulation of displaced water and oil. Finally, the last zone contains native oil shale, where combustion front still do not reached. The gas saturation increases slightly in this zone due to the high mobility of combustion gases.

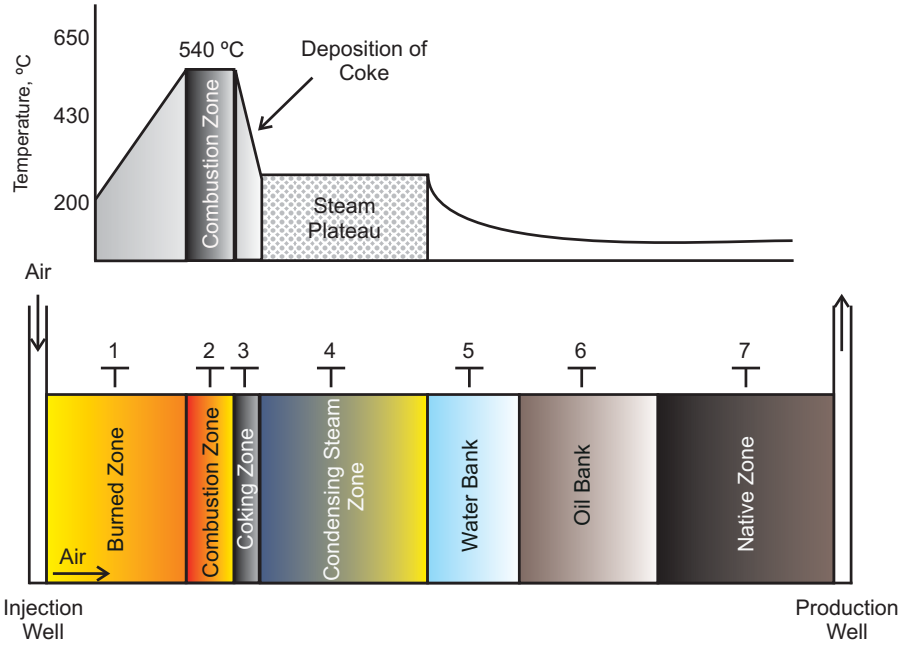

Figure 2.15: In-Situ Combustion Schematic Temperature Profile [11].

Many authors have studied the behavior of these reaction zones [13, 16, 17, 61, 62, 63, 64, 65, 66] conducting trials in laboratory by means of two techniques: ThermoGravimetry (TG) and Differential Scanning Calorimetry (DSC) analyzes.

Thermogravimetric analyzes, Figure 2.16(a), is an analytical technique in which changes in sample mass is determined as a function of temperature and/or time. It is used to determine materials thermal stability and its fraction of volatile components by monitoring the weight change that occurs when a specimen is heated. The measurement is normally carried out in air or in an inert atmosphere; exploiting the results it is possible to characterize the chemical reaction kinetics of materials. This technique is divided into isothermal thermogravimetry [67],

in which the sample mass is recorded as a function of time and constant temperature, and nonisothermal thermogravimetry [67], in which the sample mass is recorded while both, mass and temperature, are subjected to the same heating programme.

In the Differential Scanning Calorimetry (DSC), Figure 2.16(b), both sample and reference are maintained at nearly to same temperature throughout experiment and differential heat flow (endothermic and exothermic) is measured using a sample relative to a reference as a function of temperature [68]. In this experiment, not only reaction heat but also changes in the enthalpy of the material, and reaction kinetics can be evaluated.

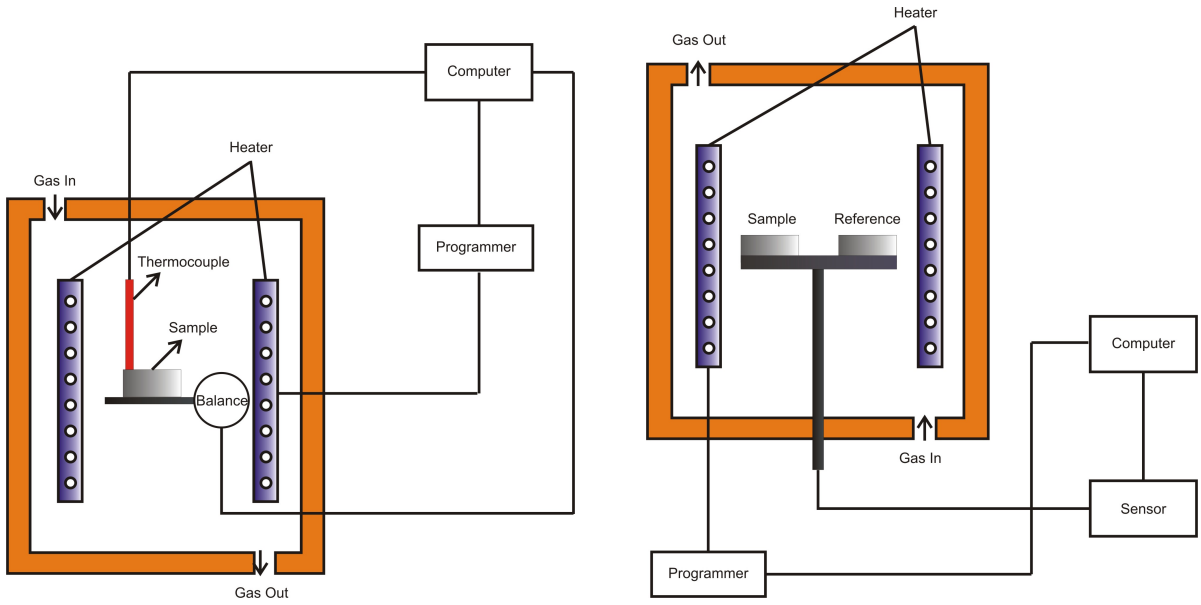

(a) TG instrument (b) DSC instrument

Figure 2.16: Schematic diagrams of a typical TG and DSC instruments

Thus, using these techniques, TG and DSC, two distinct reactions regions can be found: Low Temperature Oxidation (LTO) and High Temperature Oxidation (HTO) [11, 60, 69, 70]. LTO region are generally responsible for fuel generation [60] and in HTO region, an exothermic heterogeneous reaction occurs, where oxygen reacts with char (formed in LTO) producing CO_2, CO and H_2O. Between these two reaction regions there is a zone of linearly increasing temperature. This zone is called Fuel Deposition (FD) region in which organic matter is coked and deposited as a fuel for the combustion process [17].

Martins et al. [16], by carrying out experiments in a vertical cylindrical combustion cham-

ber, have found a way to reproduce these similar zones mentioned above and placing in evidence the role of the decarbonation reaction in the energy balance and environmental emissions.

In experiments of in-situ combustion in porous media, same reaction regions were found by Akkutlu and Yortsos [60]. In their experiments, LTO tends to increase density, apparent viscosity and boiling range of the liquid phase oil. In the FD region, excessive fuel deposition can retard the advance combustion front rate, while insufficient fuel deposition may not provide enough heat supply to self-sustaining, and HTO produces an oxidation reaction with a large activation energy.

Sarathi [11] have simplified the characteristic of the three zone as: LTO reactions are heterogeneous (gas/liquid/solid) and generally results in production of partially oxygenated compounds and little or no carbon oxides; FD reactions involve cracking/pyrolysis of hydrocarbons which leads to the formation of fixed carbon (a heavy carbon rich, low volatility hydrocarbon fraction) and HTO reactions are heterogeneous, in which the oxygen reacts with unoxidised fuel, and the oxygenated compounds to give carbon oxides and water.

Based on these regions, it is possible to build reaction mechanisms composed of various homogeneous and heterogeneous reactions [63, 64, 65, 71, 72, 73].

A review about the kinetics influence of different processes for different types of oil shale was made by Burnham [74]. The author have exhibited a set of chemical reactions presented in organic pyrolysis, carbonate decomposition, carbon combustion, sulfur and nitrogen reactions.

Concerning to the oil shale pyrolysis, various reaction mechanisms were proposed in the literature. Equation 2.1 and Equation 2.2, suggested by Hubbard and Robinson [63], represent a simple model of kerogen decomposition, where kerogen was decomposed into bitumen and gases and bitumen was decomposed into oil, gas and fixed carbon.

$$Kerogen \xrightarrow{k_1} Bitumen + Gas \tag{2.1}$$

$$Bitumen \xrightarrow{k_2} Oil + Gas + Fixed\ \ Carbon \tag{2.2}$$

The kinetics of oil shale pyrolysis using isothermal and non-isothermal thermogravimetry was studied by Thakur and Nuttall [71] and Ballice et al. [72], using kinetic mechanism showed

in Equations 2.3 and 2.4 proposed by Allred [64]. Such mechanism has considered that thermal decomposition of oil shale involves two consecutive reactions with bitumen as an intermediate, where kerogen was decomposed into gas, bitumen and fixed carbon and then bitumen was decomposed into gas, oil and fixed carbon.

$$Kerogen \xrightarrow{k_1} Bitumen + Gas + Fixed\ \ Carbon \tag{2.3}$$

$$Bitumen \xrightarrow{k_2} Gas + Oil + Fixed\ \ Carbon \tag{2.4}$$

The oil shale combustion was discussed by Khraisha [15]. The author has shown typical reactions that may take place in a fluidized bed, Table 2.1. In the organic reactions, kerogen is heated and decomposed into gas, oil and fixed carbon, as showed previously. However, in this case, occurs gas and oil oxidation of the gas and oil, releasing CO_2, CO, H_2O, heat and other. Table 2.1 also displays some exothermic and endothermic reactions along inorganic reaction of the calcite ($CaCO_3$) decarbonation and calcium silicate ($CaSiO_3$) formation.

Table 2.1: Possible reactions of oil shale in a fluidized bed combustor [15].

Organic Reaction	**Inorganic Reactions**
Volatile Release	
Kerogen+Heat → Gas + Oil + Fixed Carbon	$CaCO_3 \rightarrow CaO + CO_2$
Volatile Reaction	$CaCO_3 + SO_3 \rightarrow CaSO_4 + CO_2$
Gas + Oil + O_2 → CO_2 + H_2O + Other + Heat	$CaO + SiO_2 \rightarrow CaSiO_3$
Fixed Carbon Reactions	
Surface Reactions (Heterogeneous)	
$C + CO_2 \rightarrow 2CO$	
$C + 1/2\ O_2 \rightarrow CO$	
$C + O_2 \rightarrow CO_2$	
Phase Reaction (Homogeneous)	
$CO + 1/2\ O_2 \rightarrow CO_2$	

A similar kinetic mechanism, Equations 2.5 to 2.7, containing three reactions for oil shale

combustion in a fixed bed was proposed by Debenest [73]. The kerogen is converted into fixed carbon and volatile gases. Fixed carbon is then oxidized releasing CO_2 and heat, and calcite is decomposed into $CaO_{(s)}$ and CO_2.

$$Kerogen + Heat \xrightarrow{k_1} C_{(s)} + Volatile \tag{2.5}$$

$$C_s + O_2 \xrightarrow{k_2} CO_2 + Heat \tag{2.6}$$

$$CaCO_3 + Heat \xrightarrow{k_3} CaO_{(s)} + CO_2 \tag{2.7}$$

Rajeshwar et al. [65] have made a review about various reaction mechanisms for oil shale kerogen. Equations 2.8 to 2.12, proposed by Schnackenberg and Prien [75], are an example of more complex reaction mechanism for the thermal decomposition of the organic matter (kerogen) presents in the oil shale.

$$kerogen \xrightarrow{k_1} Rubberoid + Gas \tag{2.8}$$

$$Rubberoid \xrightarrow{k_2} Bitumen + Oil \tag{2.9}$$

$$Bitumen \xrightarrow{k_3} Semi - Coke + Oil \tag{2.10}$$

$$Semi - Coke \xrightarrow{k_4} Coke + Heavy\ \ Oil + Gas \tag{2.11}$$

$$Coke \xrightarrow{k_5} Oil \tag{2.12}$$

A more realist reaction mechanism for oil shale combustion was proposed by Martins et al. [16]. In this reaction mechanism, oil shale dries when it is heated. The organic fraction then devolatilizes and produces volatile matter. Part of this volatile matter condenses to form liquid oil. A solid residue called fixed carbon is left in the mineral matrix. If temperature is high, the carbonates in the oil shale are partly or totally decarbonated.

2.3.2 Kinetic Parameters Estimation

The kinetic parameters estimation is a very important step in reaction schemes conception commonly present in several fields of engineering. For complex reaction mechanism involving

various simultaneous reactions as those taking place in solid combustion, in gas/liquid combustion, or in the thermal decomposition of solid fuels, a robust numerical procedure may be used.

Chemical theory predicts that rate constants related to the chemical reactions should be time-temperature-dependent. Thus, variation of the rate constant with temperature and time can be represented by an Arrhenius equation, Equation 2.13, indicating the rate of chemical reactions for each species,

$$k_i = A_i exp\left(\frac{-E_i}{RT(t)}\right) with\,(i = 1, 2...) \tag{2.13}$$

where *k* is the Arrhenius constant, *A* is the pre-exponential factor, *E* is the activation energy, *R* is the ideal gas constant and *T(t)* is the temperature evolution. The subscript *i* indicates the number of chemical species.

The Arrhenius constant is related with both concentration of the constituents and reaction order by means reaction rate expressed on the form $k[A]^x[B]^y$. Then, the reaction is said to be of order $n = (x + y + ...)$ (total or overall order) and the exponents x, y can be positive or negative integral or rational non-integral numbers.

A lot of works have proposed a first order one-step reaction mechanism, [71, 76, 77, 78], because this greatly simplifies the representation of the decomposition rate and it gives a reliable result for most engineering purposes. However, for multiple-step reaction mechanisms, the assumption of first order reaction can become non-representative. Then, some authors try to introduce methodologies to estimate reaction orders [54, 79, 80]. On the basis of the reaction rate theory, the kinetic equation that appropriately describes the combustion process is presented in Equation 2.14,

$$\frac{dY}{dt} = k_i[Y(t)]^n \tag{2.14}$$

where Y is the mass fraction, in kilograms and n is the reaction order. Jiang et al. [54] in their manuscript about progress and recent utilization trends in combustion of Chinese oil shale,

have used a two-step reaction mechanism describing the entire combustion process, resulting in negative values and in high order values for n. Nowadays, the majority of the works available about pyrolysis mechanisms make the hypothesis of first order reactions.

Various methods have been proposed in order to find the set of reaction rate parameters that gives the best fit for a given set of experimental data. These methods use a variety of techniques as differential, integral and approximate methods, where the more used are Freeman-Carroll method [81, 54] and Kissinger method [82, 16, 83] inside of differential methods, and Coats-Redfern method [84, 71, 85] and Ozawa method [86, 87, 88] presents in integral methods.

Freeman-Carroll method [81] is exhibited in the Equations 2.15 to 2.17. Equation 2.15 is written in logarithmic form

$$\ln\left(\frac{dY}{dt}\right) = n\left[\ln\left(1-Y\right)\right] + \ln A - \frac{E}{R}\left(\frac{1}{T}\right) \tag{2.15}$$

Differentiating the Equation 2.15 with respect to $\ln(1-Y)$, leads to the Equation 2.16:

$$\frac{d[\ln(dY/dt)]}{d[\ln(1-Y)]} = n - \frac{E}{R}\frac{d(1/T)}{d[\ln(1-Y)]} \tag{2.16}$$

Therefore, a plot of Equation 2.17 results in a straight line of slope $-E/R$ and intercept n.

$$\frac{d[\ln(dY/dt)]}{d[\ln(1-Y)]} \;\; versus \;\; \frac{d(1/T)}{d[\ln(1-Y)]} \tag{2.17}$$

Activation energies and reaction orders are calculated from a single experimental curve. A possible problem in this method is that, due to the slope of the best-fit line to the data points has a very large absolute value, a small error in the slope estimation results in a considerable uncertainty in the value of n. As a result, it is often impossible to distinguish with confidence between various proposed reaction mechanisms using this procedure. This method shows a strong dependence on the sample mass and the heating rate [89].

The Equations 2.18 to 2.21 present the Kissinger's method [82], with a variable heating rate, which depend on the peak maximum in the DSC were employed. The activation energy (E) can be calculated from the results. Kissinger suggests a method, which relates the logarithm of (β/T_P^2) with the inverse of the peak temperature $1/T_P$, through the following Equation 2.18:

$$-\ln\left(\frac{\beta}{T_P}\right) = \frac{E}{RT_P^2} - \ln\left(\frac{AR}{E}\right) \tag{2.18}$$

Simplifying Equation 2.18 gives Equation 2.19:

$$\ln\left(\frac{T_P^2}{\beta}\right) = \frac{E}{RT_P^2} + C_1 \tag{2.19}$$

where β is heating rate, E is the activation energy, A is the pre-exponential factor, C_1 is a constant linear coefficient and R is the gas constant (8.314 J mol^{-1}K^{-1}). Thus, activation energy and pre-exponential factor were calculated using the Equation 2.20 and Equation 2.21:

$$E = R\frac{d\left[\ln\left(\beta/T_P^2\right)\right]}{d\left[1/T_P\right]} \tag{2.20}$$

$$A = \frac{\beta E}{RT_P} exp^{(E/RT_P)} \tag{2.21}$$

For a reaction in which the order is unknown, the Coats-Redfern method [84], Equation 2.22, is used:

$$log\left[\frac{1-(1-Y)^{t-n}}{T^2(1-n)}\right] = log\frac{AR}{\beta E}\left[1-\frac{2RT}{E}\right] - \frac{E}{2.3RT} \tag{2.22}$$

where Y is the fraction of the sample decomposed at time t, and β is the heating rate. A plot of either $log\left[\frac{1-(1-Y)^{t-n}}{T^2(1-n)}\right]$ against $1/T$, or, where n=1, $log\left[-\frac{ln(1-Y)}{T^2}\right]$ against $1/T$, should result in a straight line of slope $-E/2.3R$ for the correct value of n [67].

Finally, the Ozawa method [86] can be defined by Equations 2.23 to 2.25 below.

$$log\beta = log\left(\frac{AE}{R}\right) - 2.315 - 0.4567\left(\frac{E}{RT}\right) - log\left[\left(\frac{AE}{\beta R}\right)P\left(\frac{E}{RT}\right)\right] \tag{2.23}$$

In this method, plots of $log\beta$ versus $1/T$ give parallel lines for each Y value, mass fraction reacted given by Equation 2.24.

$$\alpha = \left(\frac{m_o - m_T}{m_o - m_f}\right) \tag{2.24}$$

where m_o is the initial mass of the sample, m_T is the mass of the sample at temperature T and m_f is the final mass at a temperature at which the mass loss is approximately unchanged. The slope of these lines gives the activation energy, as seen from Equation 2.25.

$$Slope = -0.4567\left(\frac{E}{R}\right) \tag{2.25}$$

The next step in the analyzes is the determination of A and reaction order n. For this reason, the theoretical curves of $(1-\alpha)$ against $logf(\alpha)$ should be found before the calculation [67].

Some of these methods provide relatively net information about mass loss behavior, but the calculation of kinetic parameters are based on ordinary assumptions that do not correspond to the complex chemical reactions during thermal degradation [61], and generally are limited only to one overall reaction.

For complex reaction mechanisms involving various simultaneous chemical reactions as the ones taking place in complex fuels - polyurethane foam, biomass, oil shales and its semi-coke, oil sands and extra-heavy oil -, the problem can be reformulated as an Optimization Problem (OP) and an objective function is minimized.

According to Elliott et al. [90], the objective function for complex fuels is usually highly structured, having multiple ridges and valleys and exhibiting multiple local optima. For this kind of objective functions, even reformulating as an OP, traditional gradient based on algorithms are likely to fail, as well as the optimization methods based upon the linearization of the objective function [90].

An alternative method to circumvent these problems has been proposed by Frenklach et al. [91] based on approximating the surface of the objective function by polynomial response

surfaces (solution mapping method). Despite its efficiency from the point of view of computational time, for this method with a highly structured surface with multiple valleys and hills, the error in approximating the objective function is large and it is likely to affect the results of the optimization procedure, like observed by Elliott et al. [90].

On the other hand, there are standard techniques widely adopted in a broad variety of disciplines for optimizing objective functions with complex and highly structured landscapes i.e. the Genetic Algorithm (GA) [92, 93, 94] and Levenberg-Marquardt (LM) algorithm [95, 96].

Genetic algorithm is a heuristic search method that imitates the principles of biological adaptation (Darwinian evolution) to seek an optimal solution to a nonlinear problem having a large number of adjustable parameters. In a genetic algorithm, the candidate solutions represent the individuals in a population that it develops with time in a predetermined environment. In this context, a candidate solution is a set of kinetic parameters values, and the environment consists of mathematical formulation of the problem and experimental thermogravimetry results [92, 93, 94].

The Levenberg-Marquardt algorithm is an iterative technique that locates the minimum of a multivariate function that is expressed as the sum of squares of non-linear real-valued functions. Levenberg-Marquardt algorithm can be thought as a combination of steepest descent and the Gauss-Newton method. When the current solution is far from the correct one, the algorithm behaves like a steepest descent method: slow, but guaranteed to converge. When the current solution is close to the correct solution, it becomes a Gauss-Newton method.

On inverse problems, the values of some model parameter must be obtained from an experimental data. As an example, the thermogravimetric analyze can be used for this propose, then, the typical results is the mass-loss rate of the solid at the corresponding temperature of the oven.

There is some works that deal with the use of inverse problem to optimise solid fuels kinetics. Rein et al. [94] have proposed a mechanism consisting of five reactions for the oxidative degradation of flexible polyurethane foam. The kinetic parameters were estimated using thermogravimetric data and genetic algorithms. The predictions, based on Arrhenius-type reaction rates, were compared to the thermogravimetric measurements, and kinetic and stoichiometric

parameters were estimated providing the best agreement between lumped model and experiments.

The kinetic parameters of substrate consumption and storage product formation of activated sludge were estimated by Fang et al. [97], using a weighted non-linear least-squares analyzes and accelerating genetic algorithm. A storage product formation equation was developed and used to construct the objective function for the determination of its production kinetics.

A simple mathematical model was developed by Sadhukhan et al. [98] to describe pyrolysis of a single biomass particle. The kinetic model consists of both primary and secondary pyrolysis reactions while heat transfer model includes diffusive, convective and radiative modes of heat transfer. The kinetic parameters and heat of reaction were estimated by Levenberg-Marquardt nonlinear optimization technique.

Loulou et al. [99] have estimated the kinetics parameters, using Levenberg-Marquardt algorithm and thermogravimetric experiments, for a reaction mechanism that represents pyrolysis process of cardboard. To design a robust estimation tool, a linear dependency analyze of the pyrolysis parameters has been made. Also, to perform this analyze, sensitivity coefficients and sensitivity matrix determinant were examined.

Reverte et al. [100] have contributed with additional numerical techniques in Levenberg-Marquardt algorithm - reparametrization - to determine the kinetic parameters and to design a more robust parameter estimation tool. This numerical technique was used when the sensitivity coefficients have a different order of magnitude, aiding in the comparison of magnitude order between them.

2.3.3 Thermochemical Models

Analyzing and modeling of the solid combustion using single particle and porous media models in stoves, boilers, furnaces, retorting process, fixed bed, fluidized bed systems and industrial processes (in-situ combustion) require adequate knowledge of the fuel properties [101].

Ragland and Aerts [101] have classified these fuel properties into physical, thermal, chemical and mineral properties. They are not still clearly understood due to mainly complex chemical reactions that happen simultaneously or sequentially, and the heat and mass transfer control in a combustion processes [102]. Thus, the building of mathematical models that join both transport phenomena - heat, momentum and mass transfer - and chemical processes are extremely important.

In the particle models, the particle size is a very important parameter that combines heat transfer with kinetic reactions, and it indicates which of them prevails over the other. Pyle and Zaror [103] have developed a new theory that defines the parameters controlling the pyrolysis rate of single particles. The authors have shown the relative importance between internal and external heat transfer and pyrolysis kinetics, determined from the Thiele modulus (Py) and Biot (Bi) number. According to their modeling calculations, if Py$\gg$1, the reaction proceeds slowly in comparison to the temperature front. If Py$\ll$1, the reaction proceeds virtually instantaneously, and the kinetic expression can be integrated directly at the temperature in question. For Bi$\gg$1, internal heat transfer is relatively slow as compared with external heat transfer, and internal temperature gradients will be significant. For Bi$\ll$1, internal heat transfer is rapid and the sample temperature can be assumed essentially uniform.

Peters and Bruch [102] have developed a flexible and stable numerical method to predict thermal decomposition of large wood particles of different sizes, shapes and properties due to drying and pyrolysis in a packed bed. The kinetic reactions for drying and pyrolysis are described by a set of one-dimensional and mass and energy transient conservation equations. The authors have made a comparison between measurements and predictions of drying models and a satisfactory agreement was yielded only for the constant evaporation temperature model. Thus, this indicates that the drying process is transport limited by heat transfer for large wood particles.

Martins et al. [104] have developed a mathematical model using one-dimensional and transient conservation equations for mass and energy in spherical coordinates for thermal decomposition of wood particles. Thermochemical conversions that happen during heating, drying and pyrolysis processes were simplified in two-step reactions. By calculating the Damkohler

number, it was verified the overlap of drying and pyrolysis process. An external heat transfer controlling regime is established using Biot number and Thiele modulus.

In a porous media model, combustion process involves a large range of geometric length scales, thermophysical and thermochemical properties, and flow, heat and mass transfer conditions. According to Oliveira and Kaviany [105], all the physical and chemical processes have different phenomenological length and time scales resulting in different transport and reaction regimes, and leading to thermal and chemical non-equilibria.

In a fixed bed experiments, Shin and Choi [106] have investigated the effects of air supply rate on the waste particles combustion using a computational model to predict the phenomena. In their experiments, the authors have found two distinct reaction modes: the oxygen-limited mode and the reaction-limited mode. In the oxygen-limited mode, the flame propagation speed increases almost linearly, while in the reaction-limited mode, the heat releasing decreases when the air supply increases further.

Gottfried [107] have used one of the first models of combustion in porous media to simulate the in-situ combustion processes to the oil recovery. The model describes the propagation of the combustion front by means of a chemical reaction between oxygen and oil, formation of a steam plateau, and formation of water and oil banks.

Zhou et al. [108] have developed one-dimensional mathematical model for optimizing operating conditions and design parameters of the straw combustion in a fixed bed. The combustion process involves moisture evaporation, straw pyrolysis, gas combustion, and fixed carbon combustion. The model provides detailed information of the structure of the ignition flame front, ignition flame front rate, bed temperature oxygen concentration and moisture content in straw. The authors found that the effective heat conductivity and heat capacity of the straw have considerable effects on the model predictions of straw combustion in the fixed bed.

Debenest et al. [109] have examined various regimes of smouldering process in porous media, and their physical consequences for a macroscopic description. To represent oxidative chemical reactions, was used a single-step heterogeneous reaction on the surface of the solid grains. The model have shown in detail the transport processes by convection and diffusion for

heat and the chemical species in the gas.

Therefore, for the processes described above, the chemical reactions that take place in kinetic mechanisms along as the fuel properties are not still fully understood and its estimation is a very important task.

Chapter 3

Inverse Problems

Inverse Problem (IP) involves the estimation of the cause from the knowledge of the effect. An advantage of IP is to join experimental and theoretical data, in order to obtain the maximum information regarding the physical problem under study. Also, inverse problem is very sensitive to random errors in measured input data, thus requiring special techniques for its solution in order to satisfy the stability condition [110].

Generally, inverse problems are mathematically classified as *ill-posed* [111]. According to Hadamard [112], the process of obtaining physical information from experimental data is an *ill-posed inverse problem* if one of the three conditions, existence, uniqueness and continuity with respect to experimental noises, is not satisfied. Some methods of inverse problems solution, such as the Levenberg-Marquardt (LM) algorithm, involve their reformulation in terms of *well-posed* minimization problems. This chapter presents in details the Levenberg-Marquardt algorithm along with a new methodology of parameter estimation.

3.1 Levenberg-Marquardt Algorithm

The Levenberg-Marquardt algorithm is an iterative technique that locates the minimum of a multivariate function that is expressed as the sum of squares of non-linear real-valued func-

tions [95, 96]. LM can be thought as a combination of steepest descent and the Gauss-Newton method. When the current solution is far from the correct one, the algorithm behaves like a steepest descent method: slow, but guaranteed to converge. When the current solution is close to the correct solution, it becomes a Gauss-Newton method, Equation 3.1.

$$\mathbf{P}^{(k+1)} = \mathbf{P}^{(k)} + [(\mathbf{J}^{(k)})^T(\mathbf{J}^{(k)})]^{-1}(\mathbf{J}^{(k)})^T[\mathbf{Y} - \mathbf{M}(\mathbf{P}^{(k)})] \tag{3.1}$$

The Levenberg-Marquardt method is also susceptible to the imprecisions about the convergence criteria. It is a local method, i.e. the global solution is not found with accuracy, and the set of kinetic parameters giving the smallest value of the minimization criterion. Classically, the solution found by this numerical method is strongly depend on the initial values chosen for the parameters [100].

According to Farooji et al. [113], Levenberg-Marquardt method is very sensitive to the initial guesses. Using poor initial guess values, the algorithm may converge to local minima. According to Eftaxias et al. [114] and Sebastiao et al. [115], to fix the local convergence problem is need to test different initial guess parameters, more precisely with 10% away from the correct value. In addition, as the number of involved parameters increases, the probability to find an initial guess suitable for all parameters decreases.

Thus, using these information, the solution of inverse problems with the Levenberg-Marquardt algorithm can be obtained through the minimization of the least-squares norm [111], Equation 3.2. Note that vectors and arrays appear in boldface, and the superscript (^{T}) is used to denote a matrix transposition.

$$\mathbf{S(P)} = [\mathbf{Y} - \mathbf{M(P)}]^T[\mathbf{Y} - \mathbf{M(P)}] \tag{3.2}$$

where $\mathbf{P} = [A_i, E_i, n_i, fr, \gamma]$, for $i = 1, 2...$, denotes the vector of unknown parameters, S is the objective function and $[\mathbf{Y} - \mathbf{M(P)}]^T$ is given by Equation 3.3,

$$[\mathbf{Y} - \mathbf{M(P)}]^T \equiv [(\mathbf{Y}_1 - \mathbf{M}_1), (\mathbf{Y}_2 - \mathbf{M}_2), ..., (\mathbf{Y}_N - \mathbf{M}_N)] \tag{3.3}$$

the right-hand side terms, $(\mathbf{Y}_i - \mathbf{M}_i)$, are the rows vector containing the differences between measured mass fraction (by experimental data from thermogravimetry) and numerical mass fraction (obtained from direct problem solution (Equation 2.14) at measurement time t.

However, according to Beck [116] and Ozisik and Orlande [110], Equation 3.2 is only valid if eight standard assumptions below, regarding to the statistical description of measurement errors in the input data cited previously, were accepted. They are:

1. The experimental errors are additive, as show the Equation 3.4

$$Y_i = M_i + \delta_i \tag{3.4}$$

where *Y*, is the measured mass fraction, *M*, denotes the numerical mass fraction and δ_i is the random error.

2. The mass errors δ_i have a zero mean, shown in the Equation 3.5

$$E(\varepsilon_i) = 0 \tag{3.5}$$

where *E* is the expected value operator. The errors are then said to be unbiased.

3. The errors have constant variance, Equation 3.6,

$$\sigma_i^2 = E[Y_i - E(Y_i)]^2 = \sigma^2 = constant \tag{3.6}$$

which means that the variance of Y_i is independent of the measurement.

4. The errors associated with different measurements are uncorrelated. Two measurement errors δ_i and δ_j, where $i \neq j$, are uncorrelated if the covariance of δ_i and δ_j is zero, Equation 3.7,

$$cov(\delta_i, \delta_j) \equiv E[\delta_i - E(\delta_i)][\delta_j - E(\delta_j)] = 0 \quad for \quad i \neq j \tag{3.7}$$

Such is the case if the errors δ_i and δ_j have no effect on or relationship to the other.

5. The measurement errors have a normal (Gaussian) distribution. By taking into consideration the assumptions 2, 3 and 4 above, the probability distribution function of δ_i is given by Equation 3.8

$$f(\delta_i) = \frac{1}{\sigma\sqrt{2\pi}} exp\left(-\frac{\delta_i^2}{2\sigma^2}\right) \tag{3.8}$$

6. The statistical parameters describing δ_i, such as σ, are known.

7. The only variables that contain random errors are the measured mass loss. The measurement times, measurement positions, dimensions of the heated body, and all other quantities appearing in the formulation of the inverse problem are all accurately known.

8. There is no prior information regarding the quantities to be estimated, which can be either parameters or functions. If such information exists, it can be utilized to obtain improved estimates.

All of the eight assumptions above rarely apply in actual experiments. However, they permit the verification of the applicability of a method of solution to a specific inverse problem, as well as of the stability of the inverse problem solution by using simulated measurements in the inverse analysis [110].

Concerning to the iterative process of the Levenberg-Marquardt algorithm, Equation 3.9 shows the discrete equation to perform this iterative procedure. This equation is the result of second order Taylor series expansion based on Newton Methods [95, 96],

$$\mathbf{P}^{(k+1)} = \mathbf{P}^{(k)} + [(\mathbf{J}^{(k)})^T(\mathbf{J}^{(k)}) + \mu^{(k)}\mathbf{\Omega}^{(k)}]^{-1}(\mathbf{J}^{(k)})^T[\mathbf{Y} - \mathbf{M}(\mathbf{P}^{(k)})] \tag{3.9}$$

The superscript $(^k)$ denotes the iteration number, $\mathbf{J}$ is the Jacobian called sensitivity matrix, μ is a positive scalar named damping parameter and $\mathbf{\Omega}$ is a diagonal matrix, Equation 3.10.

$$\mathbf{\Omega}^k = diag[(\mathbf{J}^k)^T\mathbf{J}^k] \tag{3.10}$$

The iterative process contains oscillations and instabilities that difficult the convergence process. Thus, the purpose of the matrix term $\mu^k \mathbf{\Omega}^k$ is to damp oscillations and instabilities due to the *ill-conditioned* character of the problem by making its components, if necessary, large as compared to those of $\mathbf{J}^T\mathbf{J}$ and small when the iteration procedure advances to the solution of the searched parameters. This corresponds to search for the correct update for the next iteration $\mathbf{P}^{k+1}$. The automatic control makes the Levenberg-Marquardt method a quite robust and stable estimation procedure.

There are several versions of the Levenberg-Marquardt algorithm in the literature. The main change occurs in the matrix $\Omega^{\mathbf{k}}$ that can be the identity matrix or any other. Ozisik and Orlande [110] present below one these versions available for the vector of unknown parameters **P** and initial guesses μ^0=0.001 and k=0. Then,

1. Solve the direct kinetic problem given by Equation 2.13 with the available estimate $\mathbf{P^k}$ in order to obtain the mass evolution vector $\mathbf{M(P)} = (M_1, M_2, ..., M_i)$.

2. Compute $\mathbf{S}(\mathbf{P^k})$ from Equation 3.2.

3. Compute the sensitivity matrix $\mathbf{J^k}$ defined by Equation 3.13 and then the matrix $\Omega^{\mathbf{k}}$ given by Equation 3.10 by using the current values of $\mathbf{P^k}$.

4. Solve the following linear system of algebraic equations, Equation 3.11, obtained from the iterative procedure of the Levenberg-Marquardt method, Equation 3.9:

$$[(\mathbf{J^k})^T\mathbf{J^k} + \mu^k\Omega^{\mathbf{k}}]\Delta\mathbf{P^k} = (\mathbf{J^k})^T[\mathbf{Y} - \mathbf{T}(\mathbf{P^k})] \tag{3.11}$$

   in order to compute $\Delta\mathbf{P^k} = \mathbf{P^{k+1}} - \mathbf{P^k}$.

5. Compute the new estimate $\mathbf{P^{k+1}}$ as the Equation 3.12

$$\mathbf{P^{k+1}} = \mathbf{P^k} + \Delta\mathbf{P^k} \tag{3.12}$$

6. Solve the direct problem, Equation 2.13 with the new estimate $\mathbf{P^{k+1}}$ in order to find $\mathbf{M}(\mathbf{P^{k+1}})$. Then compute $\mathbf{S}(\mathbf{P^{k+1}})$, as defined by Equation 3.2.

7. If $\mathbf{S}(\mathbf{P^{k+1}}) \geq \mathbf{S}(\mathbf{P^{k}})$, replace μ^k by $10\mu^k$ and return to step 4.

8. If $\mathbf{S}(\mathbf{P^{k+1}}) < \mathbf{S}(\mathbf{P^{k}})$, accept the new estimate $\mathbf{P^{k+1}}$ and replace μ^k by $0.1\mu^k$.

9. Check the stopping criteria given by Equation 3.16 to Equation 3.18. Stop the iterative procedure if any of them is satisfied; otherwise, replace *k* by *k+1* and return to step 3.

3.2 Sensitivity Matrix

The sensitivity matrix, Equation 3.13, is defined as

$$\mathbf{J} = \left[\frac{\partial \mathbf{M}^T(\mathbf{P})}{\partial \mathbf{P}}\right]^T = \begin{bmatrix} \frac{\partial M_1}{\partial P_1} & \cdots & \frac{\partial M_1}{\partial P_m} \\ \vdots & \ddots & \vdots \\ \frac{\partial M_N}{\partial P_1} & \cdots & \frac{\partial M_N}{\partial P_m} \end{bmatrix} \tag{3.13}$$

The elements of the sensitivity matrix are called sensitivity coefficients. They are defined as the first derivative of the estimated mass, Equation 3.14, with respect to each one of the unknown parameters P_i, with $i = 1, 2...$, computed by finite differences and with a forward difference.

$$\mathbf{J}_{ij} \cong \frac{\mathbf{M}_i(P_1, P_2, ..., P_j + \varepsilon P_j, ..., P_N) - \mathbf{M}_i(P_1, P_2, ..., P_j, ..., P_N)}{\varepsilon \mathbf{P}_j} \tag{3.14}$$

The sensitivity coefficient is a measure of the degree to which changes in unknown parameters reflect on the estimated mass loss. The sensitivity coefficient that corresponds to a certain parameter reveals if it contributes or not with useful information for the estimation process. If it is rather small, the estimation of the corresponding parameter is quite difficult and consequently the error in the estimation can be high.

To calculate the sensitivity coefficients, it is used a first derivative of the corresponding reaction mass loss $\mathbf{M}_i$ with respect to each one of the initial unknown parameters involved, $\mathbf{P}_{i,j}$ [110, 116]. According to Dantas et al. [111], sensitivity coefficients with different orders of

magnitude may create difficulties in their comparison and in their linear dependence identification. These difficulties can be mitigated calculating the Reduced Sensitivity Coefficients (RSC) by multiplying the original sensitivity coefficients by the unknown parameter, Equation 3.15.

$$\mathbf{J}_{i,j} = \mathbf{P}_{i,j} \frac{\partial \mathbf{M}_i}{\partial \mathbf{P}_{i,j}} \tag{3.15}$$

Another important point involves the Equations 3.1 and 3.9, where both require that the matrix $\mathbf{J}^T\mathbf{J}$ is non-singular, that is, $|\mathbf{J}^T\mathbf{J}| \neq 0$ because if the determinant of $\mathbf{J}^T\mathbf{J}$ is zero or even very small, the unknown parameters cannot be determined by using the iterative procedure, being denoted as ill-conditioned problems. In the next chapter, the analysis of the determinant of $\mathbf{J}^T\mathbf{J}$ will be extremely important for the process of parameters estimation.

The stopping criteria was suggested by Dennis and Schnabel [7] to stop the iterative procedure of the Levenberg-Marquardt method given by Equation 3.9 and it is presented in the Equations 3.16 to 3.18:

$$\mathbf{S}(\mathbf{P}^{k+1}) < tol \tag{3.16}$$

$$\|(\mathbf{J}^k)^T[\mathbf{Y} - \mathbf{M}(\mathbf{P}^{(k)})]\| < tol \tag{3.17}$$

$$\|\mathbf{P}^{k+1} - \mathbf{P}^k\| < tol \tag{3.18}$$

where tol is the tolerance and $\| \ \|$ is the vector Euclidean norm.

The criterion given by Equation 3.16 tests if the least squares norm is sufficiently small. Similarly, the Equation 3.17 checks if the norm of the gradient of $\mathbf{S}(\mathbf{P})$ is sufficiently small, since it is expected to vanish at the point where $\mathbf{S}(\mathbf{P})$ is minimum. The last criterion given by Equation 3.18 results from the fact that changes in the vector of parameters are very small when the method has converged [117, 110].

Confidence intervals at the 99 % confidence level for the estimated parameters are obtained by Equation 3.19:

$$\mathbf{P}_i - 2.576\sigma_{\mathbf{P}_i} \leq \mathbf{P}_i \leq \mathbf{P}_i + 2.576\sigma_{\mathbf{P}_i} \tag{3.19}$$

The standard deviation for the estimated parameters is given by Equation 3.20:

$$\sigma_{P_i} = \sigma\sqrt{\left[\mathbf{J}^T\mathbf{J}\right]^{-1}} \tag{3.20}$$

where σ is the standard deviations for experimental devices.

It is noted that the Equation 3.20 is exact for linear estimation problems and is approximately used for non-linear parameter estimation problems as it presented here, where the sensitivity coefficients are functions of the unknown parameters [117].

3.3 Parameter Estimation Algorithm

After all these information above, the methodology for parameter estimation using the Levenberg-Marquardt algorithm present in this work is explained according to the following algorithm shown in the Figure 3.1.

The first step is to solve the direct problem, i.e. the time integration of the Ordinary Differential Equations (ODEs) system, composed of reaction rates for each specie Y_i, Equation 2.14, together with both initial conditions and initial guesses. The solution of these ODEs system requires a stiff numerical solver and it is made using the *Mathematica* 7.0 software. Various solution methods can be used, as *ExplicitEuler* method, *ExplicitMidPoint* method, *LocallyExact* method and *LinearlyImplicitEuler* method, where the last one requires a large computational time to be solved.

The second step is to evaluate the sensitivity coefficients and the determinant of the matrix $\mathbf{J}^T\mathbf{J}$. As explained previously, these analyzes are very important to verify the estimation pro-

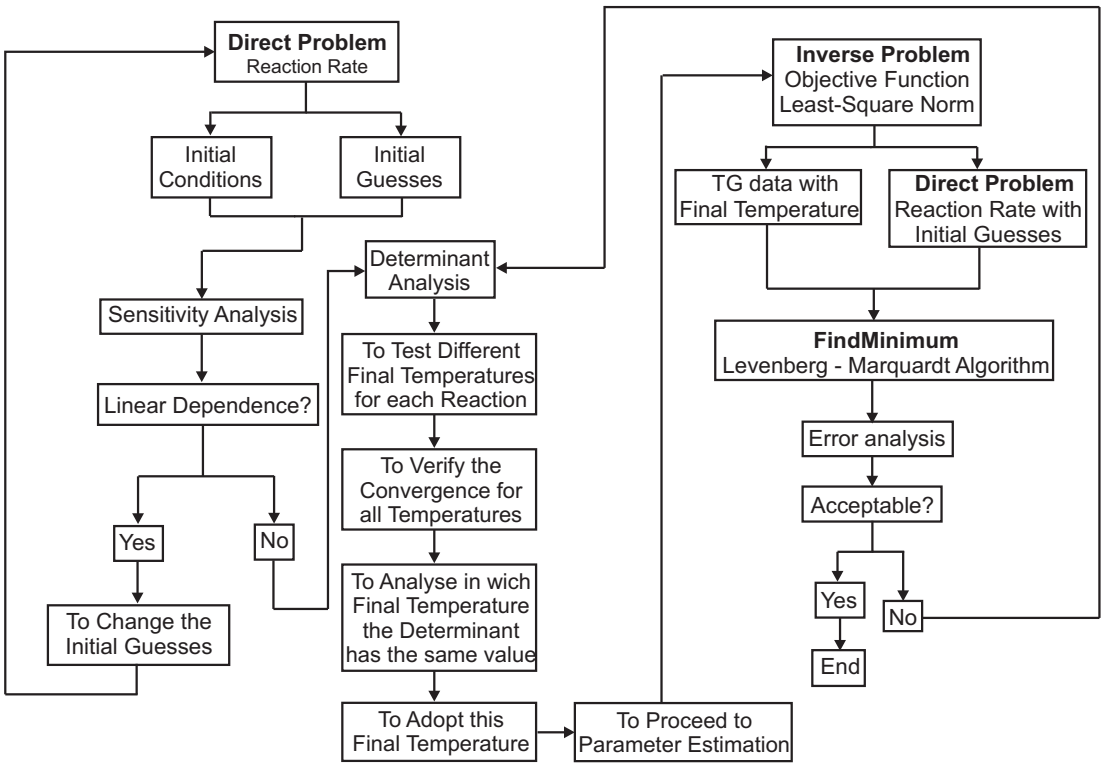

Figure 3.1: Computational algorithm of kinetic parameter estimation.

cess feasibility. Also, the sensitivity analyze indicates if the sensitivity coefficients are linearly dependent. If this happens, the parameters estimation cannot be made and it is necessary to change the initial guesses. Otherwise, the next step is to make the determinant analyze. This is an important step in parameters estimation because the beginning and the end of the chemical reaction can be previewed using the convergence of the sensitivity matrix determinant. The determinant analyze is evaluated using different final temperatures for each chemical reaction, where the final temperature indicates the end of the reaction. The main point of this analyze is to verify at which temperature the determinant do not has any change, i.e where its value do not increase any more. Thus, the final temperature adopted is the temperature where determinant is stable and the experimental data for parameters estimation are collected until this temperature.

After that, it is necessary to proceed to parameters estimation using the inverse problem technique. Thermogravimetric data and data from direct problem solution are used to estimate the kinetic parameters. Levenberg-Marquardt method is employed to minimize an objective function based on the least-square norm. The *FindMinimum* function present in the *Mathemat-*

ica software makes the iterative process. After to find a minimum for the unknown parameter, it is necessary to make a statistical analyze of the parameters estimation error. According to Varhegyi [118], laws of mathematical statistics cannot be useful in finding kinetic parameters with thermogravimetric analyze. The author shows that the statistics analyze would not be useful because the most important experimental errors from thermogravimetric apparatus are usually neither random nor independent but in relation to the difference between measured temperature and the estimated one.

Generally assumption as the sample has an uniform temperature equal to the furnace temperature is very restrictive but in the thermogravimetric analyze there are several experimental errors such as those due to the measurements of mass and temperature or due to the heterogeneity of the sample. Thus, these devices are very sensitive to the influence of many factors [119] and, this way, statistical analyzes are very important in relation to the parameters estimation.

After to evaluate the statistic error, it is essential to analyze if theses errors are acceptable. If it is not acceptable, it is necessary to back to the determinant analyze, to change the final temperature and to proceed to the parameters estimation again.

Chapter 4

Formulating and Optimizing a Pyrolysis Pathways for oil shale

Oil shales (OS) represents a valuable potential source of liquid hydrocarbons and energy due to their amount of organic matter in form of kerogen and fixed carbon, respectively. Oil and gas can be obtained by pyrolysis and retorting processes. The estimated amount of oil band to oil shale is much higher than resources of crude oil [120, 121]. However, it is necessary to know the kinetic parameters to model the pyrolysis process. In this chapter, it is presented the results of a new methodology to estimate the kinetic parameters for oil shale pyrolysis, using the Levenberg-Marquardt algorithm along with sensitivity and determinant analyzes.

4.1 Thermogravimetry

The degradation of the oil shale in general involves complex chemical pathways with small physical changes. An example of these small changes in the oil shale's microscale morphology when it is pyrolyzed can be seen in Figure 4.1, which it shows the Environmental Scanning Electron Microscopy (ESEM) images with a temperature-ramp of 30-924 ^{o}C and zoomed in 100 μm.

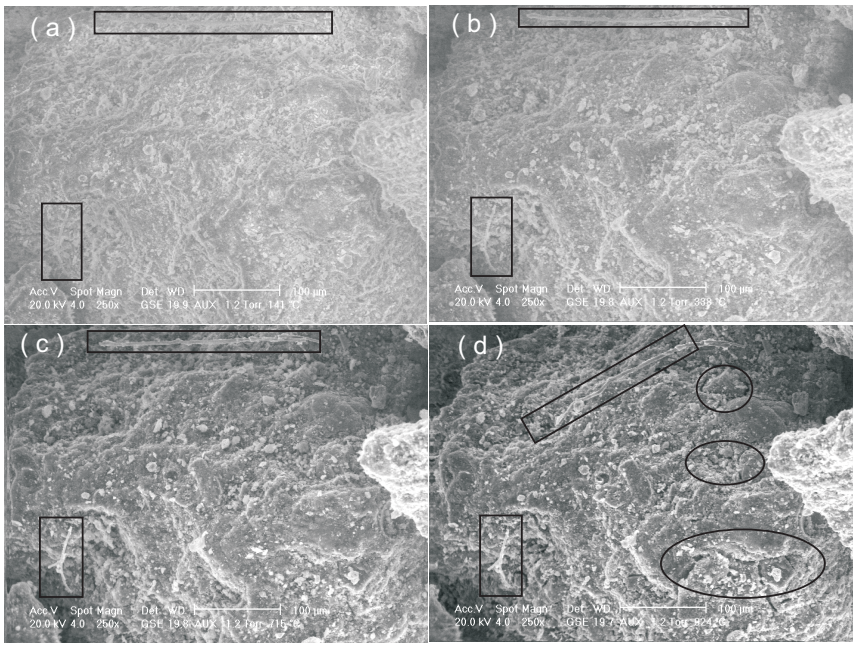

Figure 4.1: ESEM of oil shale pyrolyzed under an inert atmosphere and using a temperature ramp from 30 to 924 °C [12].

The virgin oil shale has a dense structure and the pores are imperceptible even if zoomed. When the oil shale undergoes, drying and pyrolyzes at temperatures between 100-700 °C, Figure 4.1(a-c), the surface morphology does not shows any perceptible change. Only as the temperature is up to 900 °C, some fractures can be observed and an shrinkage of the surface also become evident, Figure (4.1(d)). According to Martins et al. [13], the shrinkage along the combustion process does not exceed 3.5 % of oil shale's initial volume.

The survey of the thermochemical reactivity of a solid material is best carried out experimentally through thermogravimetric analyze. Despite of its complex kinetic behavior, experimental evidences for oil shales suggest that a mechanism consisting of only few global reactions would capture the most important characteristics of the combustion process. However, if the step numbers are so few, the mechanism results in excessive mass loss for some reaction while underpredicting other reactions rates.

The experiments of Martins et al. [13] for oil shale were carried out using a TG-DSC 111 (Setaram) with very sensitivity microbalance (limit of detection: 1 μg). The temperature

measurements were reproducible within $\pm$ 0.1 K at a temperature scale uncertainty $\pm$ 0.5 K. The samples with 40 mg approximately were heated at heating rate of 10 $Kmin^{-1}$ up to 800 ^{o}C.

These experiments suggest that a six-step mechanism would be better to describe the oil shale thermal decomposition. As known, the presence of a wide variety of minerals in the oil shale matrix significantly may difficult its thermal behavior. Consequently, a diversity of reactions is brought about by the application of heat, under an oxidative atmosphere, on the oil shale samples. In general, following reactions can potentially exist, Figure 4.2:

- evolution of water into vapor;
- conversion of Organic Matter (OM) into Volatile Matter (VM) and Fixed Carbon (FC);
- dissociation of VM into bitumen (Oil) and gases;
- oxidation of part of the gases from VM;
- oxidation of FC into gases;
- decarbonation of calcite into solid residue and gases.

By examining the thermogravimetry results in nitrogen atmosphere, Figure 4.3, it is suggested that the process of thermal decomposition can follow three stages as indicated:

1. at temperatures between 60 ^{o}C and 150 ^{o}C a mass loss of a few wt.% can be observed. This is attributed to water evaporation;
2. in the temperature range 150 ^{o}C to 600 ^{o}C an important mass loss can be observed. This stage is attributed to organic matter decomposition into volatile matter - including condensable oil - and into solid fixed carbon;
3. in the temperature range 600 ^{o}C to 800 ^{o}C, a last and important mass loss can be observed. This stage is attributed to the thermal decomposition of carbonates producing lime and carbon dioxide.

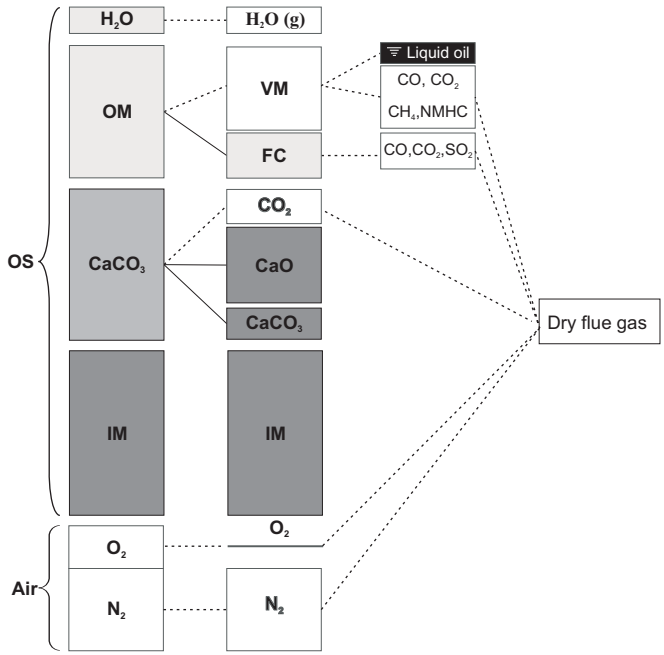

Figure 4.2: Description of the oil shale and air conversion to produce flue gas. On a dark color the components of oil shale solid residue [13].

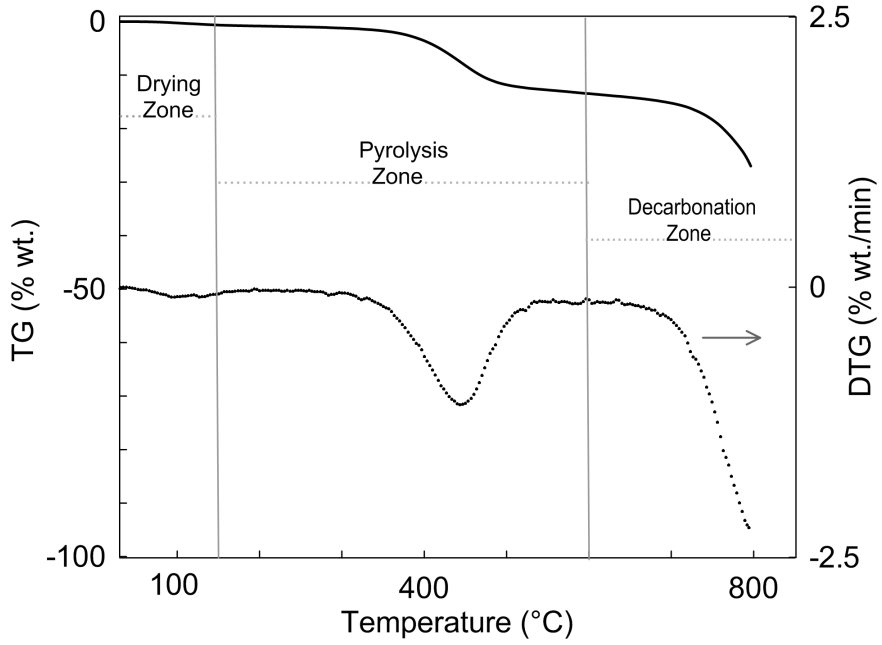

Figure 4.3: Thermogravimetric Analyze (TGA) and Differential Thermogravimetry (DTG) of oil shale under inert atmosphere - heating rate at 10 K min^{-1} [13].

It is noteworthy to mention that exists a mild to medium overlap (as indicated in Figure 4.3) with the drying/pyrolysis reactions and pyrolysis/decarbonation reactions. Consequently, the choice of the steps number in the reaction mechanism is limited, in the presented case, by the mass loss behavior from TG/DTG data, where the peak observed in DTG, Figure 4.3, represents a possible reaction occurring in this zone. Also, these physical phenomena (overlap) represents just one of the many *ill-posed* characters of the inverse problems treated here.

4.2 Kinetic Mechanisms

The kinetic mechanism for oil shale pyrolysis is shown in the Equations 4.1 to 4.5. Based on thermogravimetric results in nitrogen atmosphere, by experiments of Martins et al. [13], a three-step mechanism, Equations 4.2 to 4.4, is proposed here being composed of: *i)* drying reaction; *ii)* pyrolysis reaction and *iii)* decarbonation reaction. The overall reaction, Equation 4.1, and the Inert Material conservation, Equation 4.5, present in the kinetic mechanism are not taken into consideration in the estimation process.

$$OS \ \rightarrow H_2O + OM + CaCO_3 + IM \tag{4.1}$$

$$H_2O_{(l)} \ \xrightarrow{k_2} H_2O_{(g)} \tag{4.2}$$

$$OM \ \xrightarrow{k_3} (\alpha)VM + (1-\alpha)FC \tag{4.3}$$

$$CaCO_3 \ \xrightarrow{k_4} (\gamma)CaO + (1-\gamma)CO_2 \tag{4.4}$$

$$IM \ \rightarrow IM \tag{4.5}$$

The major breakdown mechanism in oil shale is the scission of the bonds associated with organic matter and carbonates decomposition. The devolatilization reaction of organic matter, Equation 4.3, releases volatile matter and leaves the fixed carbon in the solid matrix. In the decarbonation reaction, carbonates are considered essentially as $CaCO_3$, resulting into quick lime (solid specie) and into carbon dioxide, Equation 4.4. The drying process is described by an approach that represents a heterogeneous reaction between liquid water and vapor, Equation 4.2. The solid residue, after pyrolysis, remains as inert material, Equation 4.5.

To make possible the implementation of the mechanisms proposed above, Equations 4.2 to 4.4, into numerical models, it is necessary to quantify the stoichiometric and the kinetic parameters of each reaction. Accordingly, a method that can be applied to any mass-loss mechanism expressible in mathematical terms is implemented as following, Equations 4.6 to 4.13,

$$\frac{dY_{H_2O}}{dt} = -k_2(Y_{H_2O})^{n_2} \tag{4.6}$$

$$\frac{dY_{OM}}{dt} = -k_3(Y_{OM})^{n_3} \tag{4.7}$$

$$\frac{dY_{VM}}{dt} = (\alpha)k_3(Y_{OM})^{n_3} \tag{4.8}$$

$$\frac{dY_{FC}}{dt} = (1-\alpha)k_3(Y_{OM})^{n_3} \tag{4.9}$$

$$\frac{dY_{CaCO_3}}{dt} = -k_4(Y_{CaCO_3})^{n_4} \tag{4.10}$$

$$\frac{dY_{CaO}}{dt} = (\gamma)k_4(Y_{CaCO_3})^{n_4} \tag{4.11}$$

$$\frac{dY_{CO_2}}{dt} = (1-\gamma)k_4(Y_{CaCO_3})^{n_4} \tag{4.12}$$

where Y_i is the mass fraction of the solid species i with respect to the initial mass of the sample, and α and γ are the stoichiometric coefficients. The total mass-loss rate of the sample (Y), Equation 4.13, is the sum of the five solid species considered (Organic Matter (OM), Fixed Carbon (FC), Calcium Carbonate ($CaCO_3$), Calcium Oxide (CaO) and Inert Material (IM)) represented by Equations 4.6, 4.7, 4.9, 4.10 and 4.11.

$$Y = Y_{H_2O} + Y_{OM} + Y_{FC} + Y_{CaCO_3} + Y_{IM} \tag{4.13}$$

Each one of the reactions described in the Equation 4.2 to 4.4 is assumed to have an Arrhenius-type, Equation 2.13, and the reaction rate is according to form given by Equation 2.14.

The initial conditions (Equation 4.14) and temperature rise are set to simulate the environment in a thermogavimetric experiment,

$$\text{At } t = 0 \begin{cases} Y_{H_2O} = 0.0083 \\ Y_{OM} = 0.1684 \\ Y_{CaCO_3} = 0.3460 \\ Y_{IM} = 0.4773 \\ Y_{FC} = Y_{VM} = Y_{CaO} = Y_{CO_2} = 0 \\ T = T_0 \\ \dfrac{dT}{dt} = \beta \end{cases} \tag{4.14}$$

where the initial values and stoichiometric yields $\alpha = 0.758$ and $\gamma = 0.560$ are given from Martins et al. [13]; β is the heating rate, i.e., the controlled temperature inside the oven, typically a linear increase ramp in the thermogravimetric analyze.

4.3 Optimization Process

In this section, the results obtained by applying Levenberg-Marquardt algorithm to estimate kinetics parameters for oil shale pyrolysis are presented. The analyzes of both sensitivity coefficients and determinant of matrix $\mathbf{J}^T\mathbf{J}$ are made using the initial guesses for the unknown parameters to show the feasibility of the estimation. In addition, the comparison between experimental data from thermogravimetry and numerical results from Levenberg-Marquardt algorithm (using pre-exponential factors, activation energies and reaction orders estimated) is made, as well as the analyzes of the residual errors.

4.3.1 Sensitivity and Determinant Analyzes

The sensitivity coefficient is a measure of the degree to which changes in unknown parameters reflect on the estimated mass loss. The sensitivity coefficient that corresponds to a certain parameter reveals if it contributes or not with useful information for the estimation process. If

the sensitivity coefficient is rather small, the estimation of the corresponding parameter is quite difficult and, consequently, the estimation error can be high.

According to Dantas et al. [111], the analyzes of the sensitivity coefficients and of the determinant of the matrix $\mathbf{J}^T\mathbf{J}$ presented below are not global, that is, they are dependent on the values chosen in advance for the unknown parameters.

Thus, the sensitivity coefficients are obtained by Equation 3.14, using the following initial guess values to solve the ODEs system: $A_2 = 4.00\text{x}10^{-3}$ s^{-1}, E_2 =55.00 $kJmol^{-1}$, n_2 =1.00, A_3 =1.00 s^{-1}, E_3 =30.00 $kJmol^{-1}$, $n_3 = n_4$=1.30, A_4 =5.00x10^2 s^{-1}, E_4 =90.00 $kJmol^{-1}$. The values adopted are chosen by comparing to the similar reactions found in the literature. Figure 4.4 shows the Reduced Sensitivity Coefficients (RSC) for the kinetic parameters.

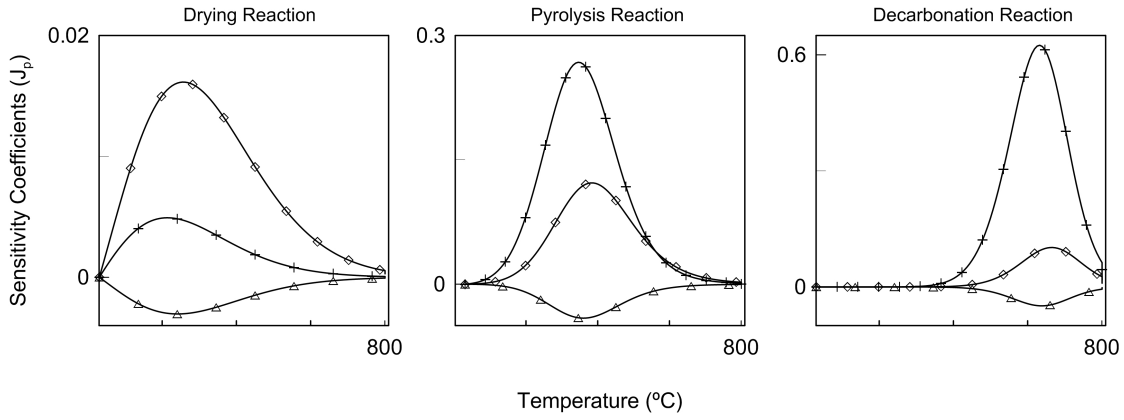

Figure 4.4: Sensitivity Analyze for drying, pyrolysis and decarbonation reactions, where ($\triangle$) is the pre-exponential factor A, ($+$) represents the activation energy E and ($\diamond$) is the reaction order n.

The sensitivity coefficient for the activation energies attain in reactions of pyrolysis and decarbonation relatively large orders of magnitude. However, for the drying reaction, all sensitivity coefficient values have very small order of magnitude, up to 10 times smaller than pyrolysis reaction. The sensitivity analyze for the pre-exponential factor, in general, presented relatively smaller magnitudes, especially for the drying reaction, where the sensitivity coefficient value was about 10^{-2}. In relation to the reaction order, their values were intermediate between the ones found for E and A, except for the drying reaction that had reaction order sensitivity coef-

ficient better than A_2 and E_2.

Note also in Figure 4.4, after passing through a maximum value, the reduced sensitivity coefficients tend to zero. For the case of the drying and pyrolysis reactions, this occurs at temperatures larger than 700 ^{o}C, and for the decarbonation reaction at temperatures larger than 800 ^{o}C. After these temperatures, the reduced sensitivity coefficients becomes relatively small and the information provided by mass measurements used in the estimation of such parameters is drastically reduced. Moreover, as the reduced sensitivity coefficient contains order of magnitude up to zero for the pre-exponential factors, the problem is highly ill-conditioned. Also, it is important to note that, after 800 ^{o}C, the decarbonation reaction is not completed due to experimental limitations of thermogravimetric analyze.

Figure 4.5 presents the results of the $|\mathbf{J}^T\mathbf{J}|$ against the temperature obtained using the initial guesses values shown previously. In the case of chemical reactions, the determinant analyze serves as a second evaluation to have a sense of where the temperature range for each reaction starts and ends. In other words, to obtain a confidence intervals and a confidence region to estimate the kinetics parameters. This analyze was performed by the trio of parameter (A_i, E_i and n_i) representing the three main reaction zones. After a careful analyze, the following temperature ranges are established to help the estimation process and they are close to the temperature ranges of the thermogravimetry. For oil shale pyrolysis:

1. The main remark about this analyze is that $|\mathbf{J}^T\mathbf{J}|$ is almost asymptotic up to 200 ^{o}C. Thus, it is established that drying reaction takes place between 60 ^{o}C and 195 ± 5 ^{o}C;

2. Based on $|\mathbf{J}^T\mathbf{J}|$ analyze, the pyrolysis reaction take place in the temperature range of 195 ± 5 - 570 ± 40 ^{o}C.

3. Finally, observing $|\mathbf{J}^T\mathbf{J}|$ values, it is established that the decarbonation reaction takes place between 570 ± 40 ^{o}C and 800 ^{o}C.

Moreover, Figure 4.5 shows that the magnitude of $|\mathbf{J}^T\mathbf{J}|$ is smaller for drying reactions. This is in agreement with the reduced sensitivity coefficients analyze, shown in Figure 4.4, which confirms that the problem is highly ill-conditioned, in special for the drying reaction. Due to

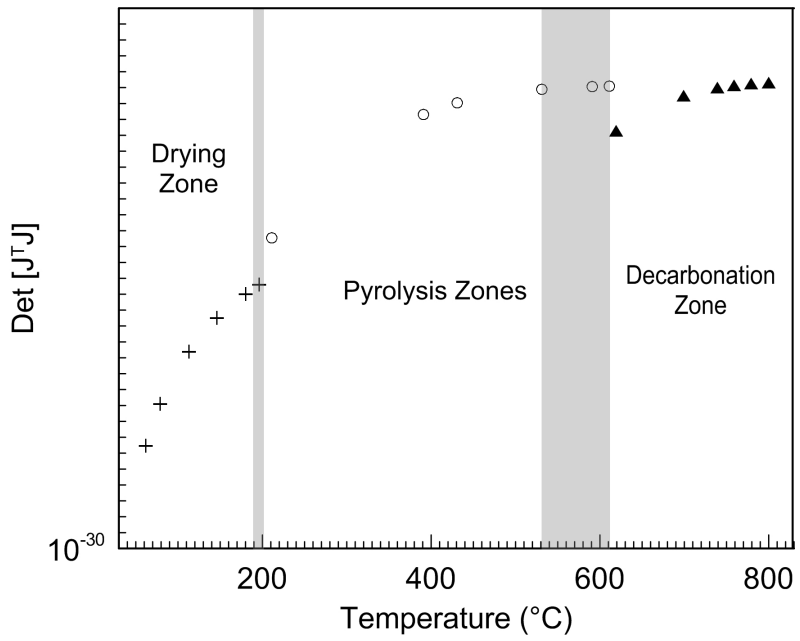

Figure 4.5: Determinant Analyze for each trio of parameters (A, E and n) estimated together.

this reason, it is expected that the parameters estimated for this set of time and temperature may have higher standard deviations.

4.3.2 Parameters Estimation

The kinetic parameters A_i, E_i and n_i estimated with Levenberg-Marquardt algorithm were obtained for a heating rate of 10 $Kmin^{-1}$. The estimation of A_2, E_2 and n_2, A_3, E_3 and n_3, A_4, E_4 and n_4 were made by using 100, 123 and 121 transient mass loss measurements respectively.

In the drying reaction, the oil shale sample lost a small amount of mass due to the water evaporation. This reaction occurs in the temperature range of 60 - 200 °C, which corresponds to the one proposed in the determinant analyze. The Arrhenius parameters estimated for this reaction were E_2 = 43.63 $kJmol^{-1}$, A_2 = 5.88x10^4 s^{-1} and n_2=1.58. For the pyrolysis reaction, occurring between 200 - 600 °C, the estimated activation energy and the pre-exponential factor were E_3 = 86.05 $kJmol^{-1}$, A_3 = 9.73x10^3 s^{-1}, and n_3=1.30. The literatures about oil shales pyrolysis [79, 62] report values of 36-103 $kJmol^{-1}$ for activation energies. Thus, this value

found here is in agreement with the literature. Finally, for the decarbonation reaction, occurring in an interval between 600 - 800 °C, the Arrhenius parameters estimated were E_4 = 251.20 $kJmol^{-1}$, A_4 = 2.14x10^{10} s^{-1} and n_4=1.29. The literature about this reaction [13, 122, 123] shows values between 135-215 $kJmol^{-1}$ for activation energies. One can note that all the reactions are of order superior to one, unlike the widely used hypothesis of first order for similar reactions, [71, 78].

Table 4.1 summarizes the results of the kinetic parameter estimation. According to Williams and Ahmad [85], the discrepancies in the activation energy for oil shales decomposition are not perhaps surprising, since the variations will occur depending on the type of oil shale and the type of pyrolysis. The authors also conclude that the activation energies are very similar irrespective of heating rates.

Reactions	**Unit**	**10 $\mathbf{Kmin^{-1}}$**	**Error (%)**
Drying	**$\mathbf{A_2}$ ($\mathbf{s^{-1}}$)**	5.88x10^4	2.61
	$\mathbf{E_2}$ ($\mathbf{kJmol^{-1}}$)	43.63	0.49
	$\mathbf{n_2}$ (-)	1.58	0.55
Pyrolysis	**$\mathbf{A_3}$ ($\mathbf{s^{-1}}$)**	9.73x10^3	1.47
	$\mathbf{E_3}$ ($\mathbf{kJmol^{-1}}$)	86.05	0.07
	$\mathbf{n_3}$ (-)	1.30	0.11
Decarbonation	**$\mathbf{A_4}$ ($\mathbf{s^{-1}}$)**	2.14x10^{10}	0.77
	$\mathbf{E_4}$ ($\mathbf{kJmol^{-1}}$)	251.20	0.02
	$\mathbf{n_4}$ (-)	1.29	0.05

Table 4.1: Parameters estimated for oil shale pyrolysis.

The estimation errors for the pre-exponential factor, A_2, the activation energy, E_2, and the reaction order, n_2, for the drying reaction were 2.61%, 0.49% and 0.55%, respectively. For the pyrolysis reaction, the errors were 1.47% , 0.07% and 0.11% respectively for A_3, E_3 and n_3. Concerning to the errors for the decarbonation reaction, the values obtained were 0.77%, 0.02% and 0.05% for A_4, E_4 and n_4 respectively. The relatively large error for the drying reaction confirms the results of both analyzes of the sensitivity and determinant of $\mathbf{J}^T\mathbf{J}$. This

large standard deviation can be attributed to the small amount of moisture in the oil shale sample (about 0.83%), becoming difficult a clear separation between the two stages involved (final temperature of drying process and initial temperature of organic matter decomposition).

Figure 4.6 shows a comparison between normalized mass loss, calculated using Equation 4.13 with estimated parameters, and experimental normalized mass loss. Such figure shows a great agreement between mass loss obtained by Equation 4.13 and measured one, which can be confirmed by the residuals shown in the figure as a dashed line. The maximum difference between estimated and measured mass loss is about 1% in the end of the experiment. The residual error is dispersed around zero line during whole experimental time. If the fitting match precisely with mean measured profile, it is possible to get the measurement errors (noise) rather of a model fluctuations [99].

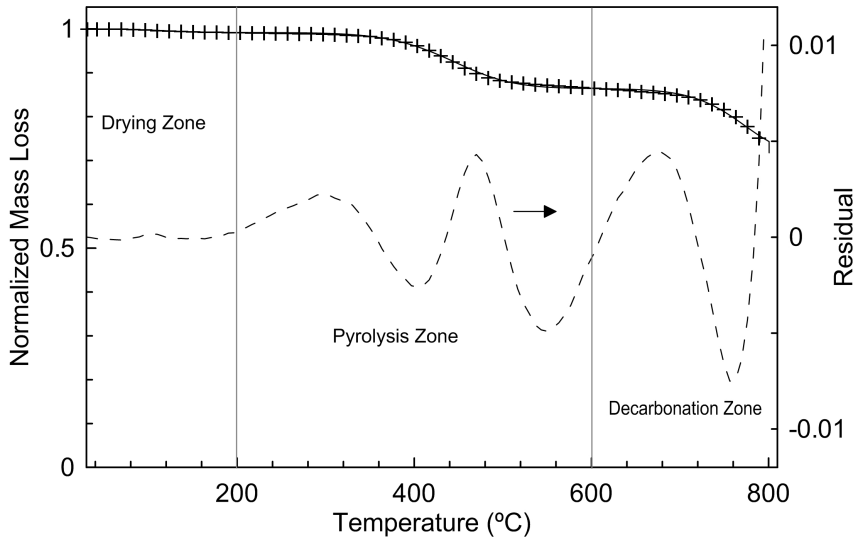

Figure 4.6: Comparison between numerical solution (line) and experimental data (+). The difference between them is the residual error (dashed line).

Finally, in the Figure 4.7, one can observe the mass fractions evolution against the temperature for oil shale pyrolysis. This figure is read by columns separated by species with same order of magnitude to facilitate the identification of their mass fraction evolution. Thus, it was established that: - for an oil shale containing about 16.84 wt.% of organic matter and 34.60 wt.% of $CaCO_3$, species mass fractions formed during pyrolysis reactions are 4.10 wt.% of fixed carbon and 12.76 wt.% of volatile matter. The mass fraction of CaO and CO_2 formed

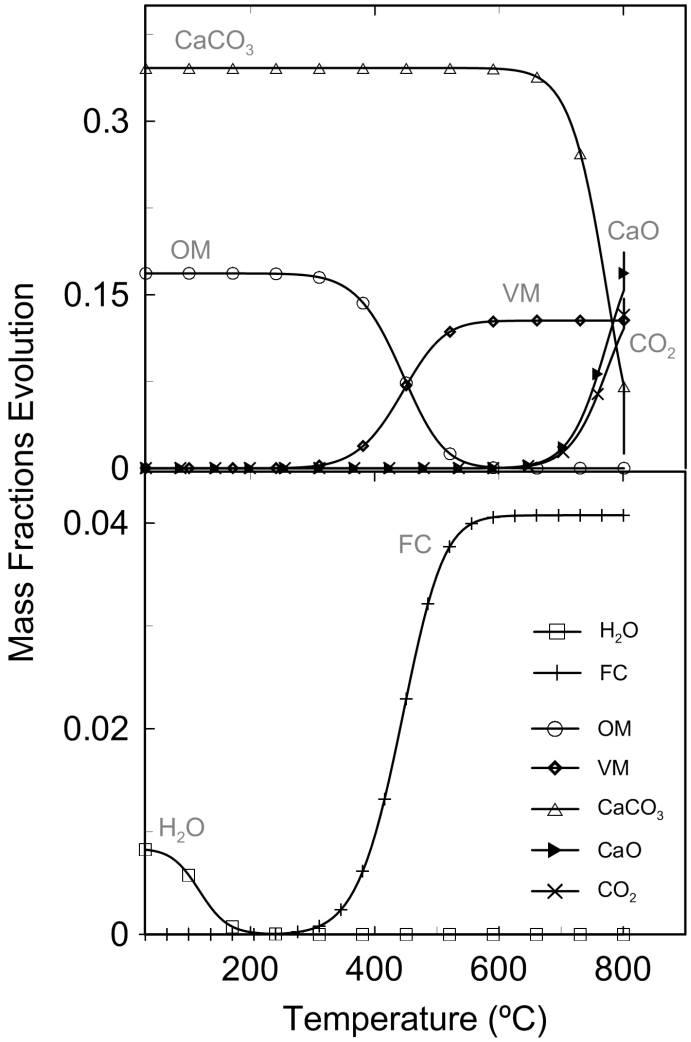

Figure 4.7: Mass fractions of different species involved in the oil shale pyrolysis.

from decarbonation reaction accounts a total of 18.66 wt.% and 14.66 wt.%, respectively.

Chapter 5

Formulating and Optimizing a Combustion Pathways for Oil shale and its Semi-Coke

Until analyzing the parameters estimation for oil shale, in this chapter is presented the kinetic parameter estimation for oil shale and its semi-coke combustion. As presented in the previous chapter, sensitivity and determinant analyzes also is made using the Levenberg-Marquardt algorithm.

5.1 Thermogravimetry

By examining the Thermogravimetry (TG)/Differential Scanning Calorimetric (DSC) results from Martins et al. [13] in an oxidative atmosphere and at heating rates of 3 and 10 $Kmin^{-1}$, it can be seen that several zones are indicated. For oil shale sample, Figure 5.1(a):

1. at temperatures between 60 ^{o}C and 150 ^{o}C a mass loss of a few wt.% can be observed. This is attributed to water evaporation. DSC experiment does not indicates significant reaction heat in this reaction, Figure 5.1(a)(in secondary axis).

2. in the temperature range 150 °C to 600 °C an important mass loss can be observed. This stage is attributed to: *i)* organic matter decomposition into volatile matter - including condensible oil - and into solid fixed carbon. *ii)* oxidation of part of the organic matter remaining as a solid, and fixed carbon oxidation. These both oxidation reactions are confirmed by the DSC test, where it is observed two strongly exothermic peaks, Figure 5.1(a).

3. in the temperature range 600 °C to 900 °C, a last and important mass loss can be observed. This stage is attributed to the thermal decomposition of carbonates producing lime and carbon dioxide. In DSC test an endothermic peak also can be noted, Figure 5.1(a).

It is clear that, in Figure 5.1, there is no precise definition where reactions start and end. Thus, the temperature range, in this case, is based on the behavior of the DSC experiments.

The origin of the second peak, observed in Figure 5.1(a), is better investigated by performing TG/DSC analyze with an semi-coke sample, Figure 5.1(b). Only the second peak appears, and it is lower compared to the test with oil shale samples. Two main conclusions can be made: - fixed carbon oxidation is responsible only for part of the energy released during High Temperature Oxidation (HTO); - The other species oxidizing during HTO is probably pyrolytic carbon that was deposited on the surface of the solid residue from the oil shale pyrolysis under TG/DSC experiments conditions. Thus, by semi-coke sample:

1. at temperatures between 60 °C and 200 °C a mass loss of a few wt.% is attributed to the water evaporation;

2. in the temperature range 200 - 550 °C is shown that the peak seen in DSC is due to fixed carbon oxidation, Figure 5.1(b)(in secondary axis).

3. in the temperature range 550 - 800 °C the mass loss is attributed to the thermal decomposition of carbonates.

It is noteworthy to mention that exist a mild to medium overlap (as indicated in Figure 5.1) with drying, pyrolysis and oxidation reactions and pyrolysis, oxidation and decarbonation

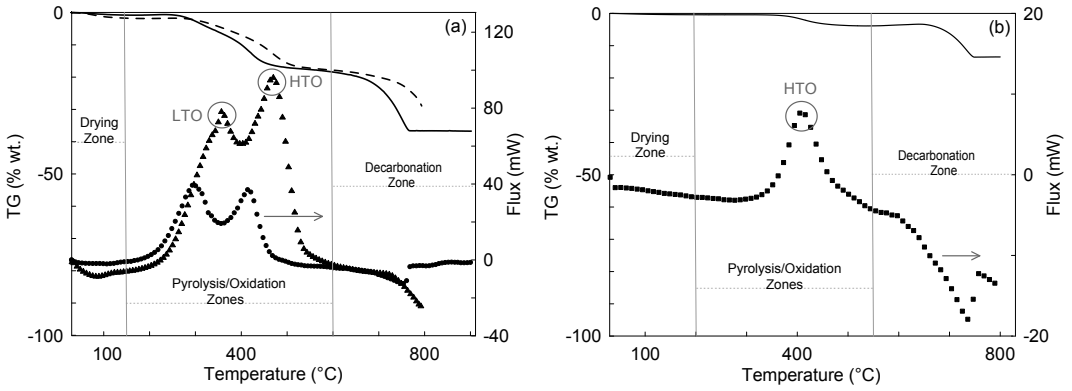

Figure 5.1: Experiments under air atmosphere. (a) Oil shale combustion. Dashed line: TGA at 10 $Kmin^{-1}$, bold solid line: TGA at 3 $Kmin^{-1}$, (▲) DSC at 10 $Kmin^{-1}$ and (•) DSC at 3 $Kmin^{-1}$. (b) Semi-coke combustion. Thin solid line: TGA at 3 $Kmin^{-1}$ and (■) DSC at 3 $Kmin^{-1}$.

reactions. Due to this overlap, the choice of the steps number in the reaction mechanism is greatly difficult and limited by TG/DSC experiments that serve only as a base to predict possible kinetic reactions that take place in combustion chambers. These physical phenomena represent just one of the many complexities of the treated problems.

5.2 Kinetic Mechanisms

The kinetic mechanism for oil shale and its semi-coke combustion is shown in the Equations 5.1 to 5.6 and Equations 5.7 to 5.11. Based on the data of Martins et al. [13], two mechanisms are proposed here: one for oil shale combustion, Equations 5.2 to 5.5, and a second one for semi-coke combustion, Equations 5.8 to 5.10. The first one is a four-steps mechanism, and the second one a three-steps mechanism. The overall reactions, Equations 5.1 and 5.7, and the Inert Material, Equations 5.6 and 5.11, present in both kinetic mechanisms are not taking into consideration in the estimation process.

$$OS \rightarrow H_2O + OM + CaCO_3 + IM \tag{5.1}$$

$$H_2O_{(l)} \xrightarrow{k_2} H_2O_{(g)} \tag{5.2}$$

$$OM \xrightarrow{k_3} [(\alpha_{Oil})Oil + (\alpha_{CO})CO + (\alpha_{CO_2})CO_2 + (\alpha_{HC})HC] + (\alpha_{FC})FC \tag{5.3}$$

$$(\alpha_{FC})FC + (\alpha_{FC})\left[\left(\frac{fr}{2}\right) + (1-fr)\right]O_2 \xrightarrow{k_4} (\alpha_{FC})(fr)CO + \\ +(\alpha_{FC})(1-fr)CO_2 \tag{5.4}$$

$$CaCO_3 \xrightarrow{k_5} (\gamma)CaO + (1-\gamma)CO_2 \tag{5.5}$$

$$IM \rightarrow IM \tag{5.6}$$

$$SC \rightarrow H_2O + FC + CaCO_3 + IM \tag{5.7}$$

$$H_2O_{(l)} \xrightarrow{k_2} H_2O_{(g)} \tag{5.8}$$

$$FC + \left[\left(\frac{fr}{2}\right) + (1-fr)\right]O_2 \xrightarrow{k_3} (fr)CO + (1-fr)CO_2 \tag{5.9}$$

$$CaCO_3 \xrightarrow{k_4} (\gamma)CaO + (1-\gamma)CO_2 \tag{5.10}$$

$$IM \rightarrow IM \tag{5.11}$$

The three main constituents of oil shale which decompose are organic matter, fixed carbon and carbonates, consequently its major breakdown mechanism is the scission of bonds associated with these constituents. The devolatilization reaction of Organic Matter (OM), Equation 5.3, releases Oil known as bitumen, as well as oxides of carbon such as CO, CO_2, and light hydrocarbons represented by HC, leaving fixed carbon (FC) in the solid matrix. In the oxidation reaction, Equation 5.4, fixed carbon is oxidized, releasing CO and CO_2. In decarbonation reaction, carbonates are considered essentially as $CaCO_3$, resulting into quick lime (solid specie) and more carbon dioxide, Equation 5.5. The drying process is described by the approach that represents a heterogeneous reaction between liquid water and vapor, Equation 5.2. In the solid residue, remains an Inert Material (IM), Equation 5.6.

5.2.1 Nonlinear Systems of Differential Equations

To make possible the implementation of the mechanisms proposed above, Equation 5.2 to 5.5 and Equation 5.8 to 5.10 into numerical models, it is necessary to quantify both stoichiometric and kinetic parameters of each reaction. Accordingly, a method that can be applied to

any mass loss mechanism expressible in mathematical terms is implemented following for oil shale and semi-coke, Equations 5.12 to 5.23 and Equations 5.24 to 5.31, respectively.

$$\frac{dY_{H_2O}}{dt} = -k_2(Y_{H_2O})^{n_2} \tag{5.12}$$

$$\frac{dY_{OM}}{dt} = -k_3(Y_{OM})^{n_3} \tag{5.13}$$

$$\frac{dY_{Oil}}{dt} = (\alpha_{Oil})k_3(Y_{OM})^{n_3} \tag{5.14}$$

$$\frac{dY_{HC}}{dt} = (\alpha_{HC})k_3(Y_{OM})^{n_3} \tag{5.15}$$

$$\frac{dY_{FC}}{dt} = (\alpha_{FC})k_3(Y_{OM})^{n_3} - (\alpha_{FC})k_4P_{O_2}(Y_{FC})^{n_4}(Y_{O_2})^{n_5} \tag{5.16}$$

$$\frac{dY_{O_2}}{dt} = -(\alpha_{FC})\left[\left(\frac{fr}{2}\right) + (1-fr)\right]k_4P_{O_2}(Y_{FC})^{n_4}(Y_{O_2})^{n_5} \tag{5.17}$$

$$\frac{dY_{CO}}{dt} = (\alpha_{CO})k_3(Y_{OM})^{n_3} + (\alpha_{FC})(fr)k_4P_{O_2}(Y_{FC})^{n_4}(Y_{O_2})^{n_5} \tag{5.18}$$

$$\frac{dY_{CO_2}}{dt} = (\alpha_{CO_2})k_3(Y_{OM})^{n_3} + (\alpha_{FC})(1-fr)k_4P_{O_2}(Y_{FC})^{n_4}(Y_{O_2})^{n_5} + \\ +(1-\gamma)k_5(Y_{CaCO_3})^{n_6} \tag{5.19}$$

$$\frac{dY_{CaCO_3}}{dt} = -k_5(Y_{CaCO_3})^{n_6} \tag{5.20}$$

$$\frac{dY_{CaO}}{dt} = (\gamma)k_5(Y_{CaCO_3})^{n_6} \tag{5.21}$$

where Y_i is the mass fraction of species i with respect to the initial mass of the sample, n_i represents the reaction order, α and γ are the stoichiometric mass coefficient given from experiments of Martins et al. [13] and P_{O_2} denotes the oxygen partial pressures given by Equation 5.22. The initial partial pressure Po is one used in the experiments of Martins et al. [13]. P_{O_2} increases until reaching a plateau of the 7.5 kPa in the time *t* and it remains constant until final time t_f. According to Soni and Thomson [124], P_{O_2} varies between 3 - 21 kPa in thermogravimetry experiments for given heating rate, β ($Kmin^{-1}$).

$$\begin{cases} P_{O_2} = Po + \beta t \quad to \quad t \leq t_f \\ P_{O_2} = 7.5 \quad to \quad t > t_f \end{cases} \tag{5.22}$$

The Arrhenius-type equation, Equation 2.13, is related with both mass fraction of species and reaction order. The species that correspond to water (H_2O), organic matter, fixed carbon, calcium carbonate ($CaCO_3$) and calcium oxide (CaO), Equations 5.12 to 5.21, are summed and added to Equation 5.6 resulting in the final mass fraction (Y), Equation 5.23.

$$Y = Y_{H_2O} + Y_{OM} + Y_{FC} + Y_{CaCO_3} + Y_{CaO} + Y_{IM} \tag{5.23}$$

Same procedure is made to the kinetic mechanism for the semi-coke, Equations 5.24 to 5.31, except that this solid fuel does not undergoes organic matter devolatilization reaction.

$$\frac{dY_{H_2O}}{dt} = -k_2(Y_{H_2O})^{n_2} \tag{5.24}$$

$$\frac{dY_{FC}}{dt} = -k_3 P_{O_2}(Y_{FC})^{n_3}(Y_{O_2})^{n_4} \tag{5.25}$$

$$\frac{dY_{O_2}}{dt} = -\left[\left(\frac{fr}{2}\right) + (1-fr)\right] k_3 P_{O_2}(Y_{FC})^{n_3}(Y_{O_2})^{n_4} \tag{5.26}$$

$$\frac{dY_{CO}}{dt} = (fr)k_3 P_{O_2}(Y_{FC})^{n_3}(Y_{O_2})^{n_4} \tag{5.27}$$

$$\frac{dY_{CO_2}}{dt} = (1-fr)k_3 P_{O_2}(Y_{FC})^{n_3}(Y_{O_2})^{n_4} + (1-\gamma)k_4(Y_{CaCO_3})^{n_5} \tag{5.28}$$

$$\frac{dY_{CaCO_3}}{dt} = -k_4(Y_{CaCO_3})^{n_5} \tag{5.29}$$

$$\frac{dY_{CaO}}{dt} = (\gamma)k_4(Y_{CaCO_3})^{n_5} \tag{5.30}$$

$$Y = Y_{H_2O} + Y_{FC} + Y_{CaCO_3} + Y_{CaO} + Y_{IM} \tag{5.31}$$

Initial conditions (Table 5.1), and temperature rise (controlled temperature inside the oven, typically a linear increase ramp) are set to simulate the environment in a thermogravimetric experiment for oil shale at heating rates of 3 $Kmin^{-1}$ and 10 $Kmin^{-1}$ and semi-coke at 3 $Kmin^{-1}$. Notice that, these initial conditions initially extracted from Martins et al. [13] were rebuilt to adapt them to the reaction ranges, as observed after in Figure 5.3.

The time integration of the mass loss rates, Equations 5.12 to 5.23 and Equations 5.24 to 5.31, together with initial conditions and initial guesses, Table 5.1 and Table 5.2 respectively, provide the mass fraction of each species (Y_i) at any given time.

Table 5.1: Initial conditions for the differential equation systems.

	Oil Shale	**Semi-Coke**
Y_{H_2O}[a]	1.25 $\pm$0.48	0.44
Y_{OM}[a]	19.70 $\pm$ 0.30	-
Y_{CaCO_3}[a]	34.60	40.56
Y_{IM}[a]	44.44 $\pm$ 0.17	55.56
Y_{FC}[a]	0.0	3.44
Y_{CO}[a]	0.0	0.0
Y_{CO_2}[a]	0.0	0.0
Y_{Oil}[a]	0.0	-
Y_{HC}[a]	0.0	-
Y_{O_2}[a]	3.59 $\pm$ 0.22	2.47
α_{Oil}[a]	53.00	-
α_{HC}[a]	16.73	-
α_{CO}[a]	1.02	-
α_{CO_2}[a]	5.05	-
α_{FC}[a]	24.20	-
P_{O_2} [b]	7.5	7.5
Po[b]	0.4	0.4
T=To[c]	30.08 $\pm$ 0.56	31.07

[a] Y in OS wt.% and α in OM wt.% .

[b] P in kPa.

[c] T in ^{o}C.

For oil shale combustion, the system contains 15 unknown kinetic parameters: four activation energies (E_i) and pre-exponential factors (A_i), five reaction-order coefficients (n_i), one (fr) parameter to estimate the amount of carbon oxidized into CO or/and CO_2, and one (γ) stoichiometric parameter to balance the ratio of the decarbonation products CaO and CO_2. For semi-coke combustion, the system contains 12 unknown kinetic parameters: three activation energies and pre-exponential factors, four reaction-order coefficients and finally, one (fr) and one (γ) parameter.

5.3 Sensitivity Analyze

Using the same methodology from Chapter 4, Figure 5.2 shows the reduced sensitivity coefficient analyze for the unknown parameters organized by reaction, heating rate and kind of fuel (oil shale and semi-coke). In the Table 5.2 is shown the initial guesses values used in this analyze.

The sensitivity coefficient related to activation energies attain relatively large orders of magnitude in pyrolysis, oxidation and decarbonation reactions, otherwise is observed in drying reaction. The sensitivity analyzes associated to the pre-exponential factor, in general, showed relatively smaller magnitudes when compared to the ones found for activation energies. In relation to the sensitivity analyzes for reaction order, the values were intermediate between the values for E and A, except for the drying reaction that had the sensitivity coefficient for the reaction order better than A_2 and E_2. About the oxidation reaction, sensitivity analyzes for fr indicate orders of magnitude close to the pre-exponential factor and in the decarbonation reaction, orders of magnitude for γ showed similar to those found for reaction order. The sensitivity value for γ, in semi-coke decarbonation, reached values better than A and n.

Table 5.2: Initial guesses for the unknown parameters in the differential equation systems.

Initial Guess			**Oil Shale**		**Semi-Coke**
Reaction		**Unit**	**3** $\mathbf{Kmin^{-1}}$	**10** $\mathbf{Kmin^{-1}}$	**3** $\mathbf{Kmin^{-1}}$
Drying	$\mathbf{A}_2$	(s^{-1})	4.00x10^{-3}	4.00x10^{-3}	3.50x10^{6}
	$\mathbf{E}_2$	($kJmol^{-1}$)	5.50	5.50	33.60
	$\mathbf{n}_2$	(-)	1.00	1.00	2.42
Pyrolysis	$\mathbf{A}_3$	(s^{-1})	4.00x10^{1}	4.00x10^{1}	-
	$\mathbf{E}_3$	($kJmol^{-1}$)	50.00	50.00	-
	$\mathbf{n}_3$	(-)	1.30	1.30	-
Oxidation	$\mathbf{A}_4$	(s^{-1})	8.05x10^{5}	8.05x10^{5}	8.60x10^{16}
	$\mathbf{E}_4$	($kJmol^{-1}$)	100.00	100.00	210.60
	$\mathbf{n}_4$	(-)	1.30	1.30	1.78
	$\mathbf{n}_5$	(-)	1.40	1.30	1.78
	fr	(-)	0.42	0.56	0.56
Decarbonation	$\mathbf{A}_5$	(s^{-1})	5.00x10^{2}	5.00x10^{2}	6.40x10^{7}
	$\mathbf{E}_5$	($kJmol^{-1}$)	110.00	110.00	105.60
	$\mathbf{n}_6$	(-)	1.40	1.60	1.60
	γ	(-)	0.43	0.56	0.70

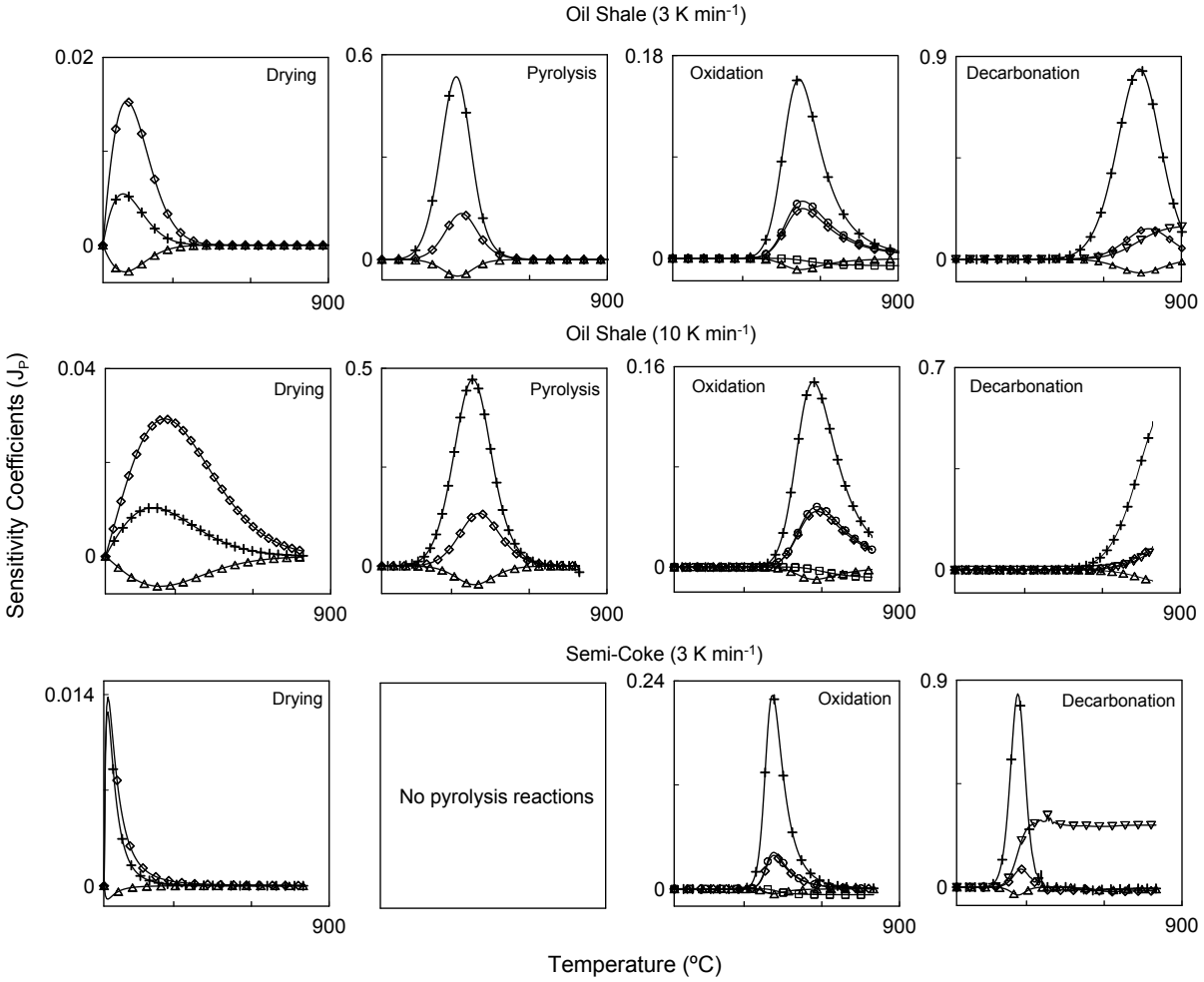

Figure 5.2: Sensitivity Analyze, where ($\triangle$) represents the pre-exponential factor A, ($+$) represents the activation energy E, ($\diamond$) represents the reaction order n, ($\square$) represents the fr and ($\bigtriangledown$) represents the γ

5.4 Determinant Analyze

In relation to the chemical reactions, the determinant analyze serves as a second evaluation to have a sense of where the temperature range for each reaction starts and ends. In other words, to obtain a confidence intervals and a confidence region to estimate the kinetics parameters. It was evaluated by using the same methodology from Chapter 4.

Figure 5.3 presents the results of the $|\mathbf{J}^T\mathbf{J}|$ against temperature. This analyze is performed by grouping of kinetics parameters correspondent to its respective chemical reaction, represented in this figure by reaction zones. After a careful analyze, the following temperature ranges are established to help the estimation process, and they are close to the temperature ranges of thermogravimetry. For oil shale combustion, Figure 5.3 (left side),

1. the main remark about this analyze is that $|\mathbf{J}^T\mathbf{J}|$ is almost asymptotic at 150 ^{o}C. Thus, it is established that the drying reaction takes place between 60 ^{o}C and 165 ± 15 ^{o}C;

2. based on $|\mathbf{J}^T\mathbf{J}|$ analyze, the pyrolysis and oxidation reactions take place in a temperature range of 165 ± 15 - 652 ± 17 ^{o}C.

3. finally, observing $|\mathbf{J}^T\mathbf{J}|$ values, it is established that the decarbonation reaction takes place between 652 ± 17 ^{o}C and 900 ^{o}C.

   By using the same methodology for semi-coke combustion, Figure 5.3 (right side), it is established that:

4. drying reaction takes place between 60 ^{o}C and 185 ± 35 ^{o}C. Note that due to the small amount of moisture in the semi-coke, see Table 5.1, and the fact of the thermogravimetric measurement become least accurate to catch little changes in mass, the temperature range, where drying reaction will finish, increases.

5. oxidation reaction takes place in a temperature range of 185 ± 35 ^{o}C - 540 ± 10 ^{o}C;

6. decarbonation reaction takes place between 540 ± 10 ^{o}C and 800 ^{o}C.

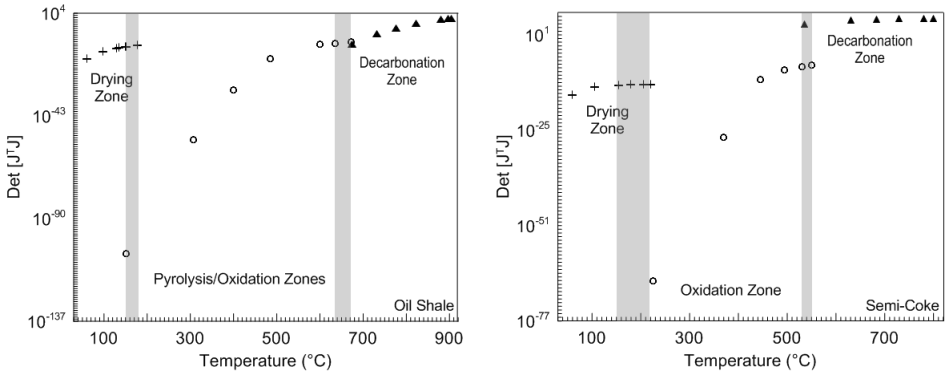

Figure 5.3: Determinant analyze for oil shale and semi-coke, where (+) represents the drying zone, (○) represents the pyrolysis/oxidation zone and (▲) represents the decarbonation zone. The vertical thin solid lines represent where is a possible beginning and end of the zones.

5.5 Parameters Estimation

Figure 5.4 presents the results obtained by comparing estimated mass loss with experimental mass loss from thermogravimetric analyze. From a qualitative point of view, this figure shows the data points with best-fitted lines and the corresponding residual errors. One can observe that, in all cases, residual errors not exceed 4.0 %. The residual error is dispersed around zero line during whole experimental time. If the fitting match precisely with the mean measured profile, it is possible to get the measurement errors (noise) rather of a model fluctuations [99].

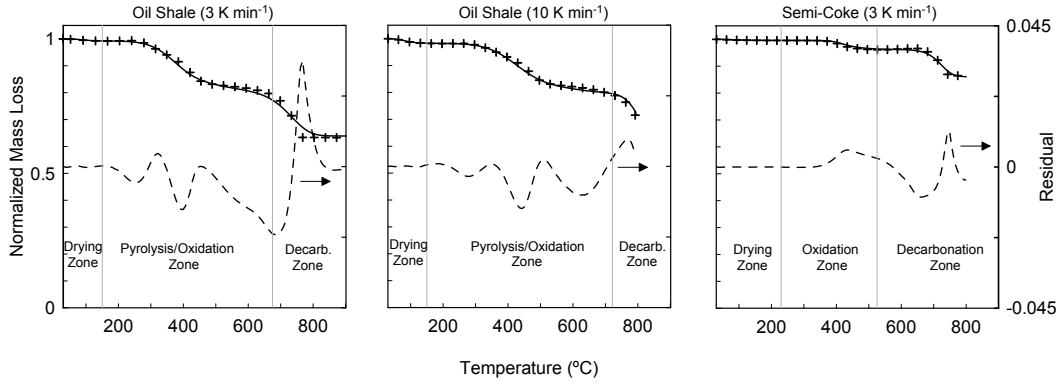

Figure 5.4: Comparison between numerical solution (bold line) and experimental data (+). The difference between them is the residual error (dashed line).

By examining the estimation process in more details, the relationship between sensitivity

coefficient and its impact on the standard error can be verified. The results are summarized in Table 5.3, showing the estimated kinetic parameters and their standard errors calculated by Equation (3.20), where the standard deviations for thermogravimetry apparatus was $\sigma = 10^{-4}$ kg [16].

As outlined previously, the sensitivity coefficient that corresponds to a certain parameter, if rather small does not contributes with useful information for the estimation process. Also, its estimation is quite difficult and consequently the estimation error is higher. This is the case verified to the pre-exponential factor that presents highs errors, up to 85.53% related to drying reactions and about 60.16% related to oxidation reaction.

Concerning to the estimated activation energies, they present a maximum error of 3.92% for drying reaction. As a result, the hypothesis of an heterogeneous reaction between liquid water and vapor remains reasonable. The estimated activation energies for oxidation reactions varies from 102 to 211 $kJmol^{-1}$. The literatures about oil shales [54, 125] report values of 82 - 195 $kJmol^{-1}$ and 13 - 408 $kJmol^{-1}$ respectively. The values of 61 - 65 $kJmol^{-1}$ estimated for pyrolysis reactions are in agreement with the ones reported by Thakur and Nuttall [71] to the same oil shale deposits. Regarding to the activation energies for decarbonation of $CaCO_3$, the estimated values are about 162 - 418 $kJmol^{-1}$ (oil shale decarbonation) and 291 $kJmol^{-1}$ (semi-coke decarbonation). According to previous work made by Thomson et al. [126], the calcite activation energy (in oil shale decarbonation) varies between 175 - 244 $kJmol^{-1}$. The high activation energy (418 $kJmol^{-1}$) for the oil shale decarbonation at heating rate of 10 $Kmin^{-1}$ is an overestimated value due to limitations in the temperature range of the thermogravimetry experiment. In this case, the decarbonation reaction was not fully completed. According to Williams and Ahmad [85], the discrepancies in the activation energy for oil shale decomposition is not perhaps surprising, since the variations will occur depending on the type of oil shale and type of pyrolysis. The authors also conclude that the activation energies are very similar irrespective of heating rates.

About the estimated values of the reaction orders, the maximum error is up to 21.96%. All the reactions studied have showed reaction order superior to one, except to the decarbonation reaction at heating rate of 3 $Kmin^{-1}$, where the reaction order is close to one.

Table 5.3: Estimated parameters for oil shale and semi-coke kinetics mechanism.

		Oil Shale				Semi-Coke	
Reactions	**Unit**	**3** $\mathbf{Kmin^{-1}}$	**Error (%)**	**10** $\mathbf{Kmin^{-1}}$	**Error (%)**	**3** $\mathbf{Kmin^{-1}}$	**Error (%)**
Drying	$\mathbf{A_2}$ **(**$\mathbf{s^{-1}}$**)**	1.09x10^{10}	49.17	3.40x10^{7}	35.17	3.14x10^{6}	85.53
	$\mathbf{E_2}$ **(**$kJmol^{-1}$**)**	67.80	1.38	54.65	1.27	33.42	3.92
	$\mathbf{n_2}$ **(-)**	2.29	1.42	1.89	1.30	2.41	2.82
Pyrolysis	$\mathbf{A_3}$ **(**$\mathbf{s^{-1}}$**)**	2.64x10^{2}	1.32	1.58x10^{2}	2.93	-	-
	$\mathbf{E_3}$ **(**$kJmol^{-1}$**)**	65.38	0.06	61.91	0.12	-	-
	$\mathbf{n_3}$ **(-)**	1.28	0.21	1.27	0.62	-	-
Oxidation	$\mathbf{A_4}$ **(**$\mathbf{s^{-1}}$**)**	7.41x10^{6}	23.72	3.40x10^{6}	7.72	9.32x10^{16}	60.16
	$\mathbf{E_4}$ **(**$kJmol^{-1}$**)**	102.51	0.86	103.73	1.04	211.03	0.56
	$\mathbf{n_4}$ **(-)**	1.32	4.41	1.34	21.96	1.78	1.85
	$\mathbf{n_5}$ **(-)**	1.96	1.70	1.65	14.56	1.77	4.73
	fr (-)	0.07	2.01	0.25	6.51	0.96	4.22
Decarbonation	$\mathbf{A_5}$ **(**$\mathbf{s^{-1}}$**)**	2.67x10^{6}	0.75	3.16x10^{18}	20.59	3.90x10^{12}	2.23
	$\mathbf{E_5}$ **(**$kJmol^{-1}$**)**	162.41	0.03	418.35	0.31	291.17	0.06
	$\mathbf{n_6}$ **(-)**	1.07	0.06	1.60	4.58	1.25	0.12
	γ **(-)**	0.53	0.00	0.56	2.02	0.75	0.00

With respect to the estimated parameters fr (to express the quantity of carbon oxidized into CO or/and CO_2) and γ (a stoichiometric parameter in decarbonation reaction), the following remarks can be made. The maximum error in their estimation is about 6.51% for fr and 2.02% for γ. Different values of fr are estimated for oil shale, 0.07 and 0.25, for the heating rate 3 and 10 K min^{-1}, respectively. It means that, numerically, by increasing heating rate, increases the amount of fixed carbon oxidized into CO. Martins et al.[13] report values of fr equal to 0.565 for oil shale combustion in a cylindrical reactor. Sennoune et al. [53], utilizing the same reactor, have studied the impact of the fixed carbon fraction oxidized into CO. For an oil shale containing 3.48 wt.% of fixed carbon and 22.4 wt.% of $CaCO_3$, and considering that the oxidation reaction occurs at 500 °C, fr value is up to 0.65. However, in both of these papers the heating rate inside the bed is between 60-90 K min^{-1}, this is much higher than the operating heating rate in a standard thermogravimetry experiment.

For the semi-coke case, where no more volatile matter exist, the value of the fr = 0.96 suggest that almost all carbon is oxidized into CO. There are not any works available in literature about semi-coke combustion to aid establish some comparison.

Finally, in the Figure 5.5, one can observe the mass fractions evolution against temperature for the three cases presented. This figure is read by columns and each column separated by species with same order of magnitude to facilitate the identification of their mass fraction evolution. From the runs at 3 K min^{-1} it was established that: - for an oil shale containing about 20 wt.% of organic matter and 34.60 wt.% of $CaCO_3$, the species mass fractions formed during pyrolysis and oxidation reactions are 3.4 wt.% of fixed carbon, 10.6 wt.% of Oil, 3.3 wt.% of hydrocarbons and 1.8 wt.% of CO. The mass fraction of CO_2 formed from pyrolysis/oxidation/decarbonation reactions accounts a total of 21.6 wt.%; - for a semi-coke containing 3.4 wt.% of fixed carbon and 40.6 wt.% of $CaCO_3$ its combustion forms 2.1 wt.% of CO. The CO_2 from oxidation and decarbonation reaction accounts 10.2 wt.%, considering that $\gamma = 0.75$ in the decarbonation reaction.

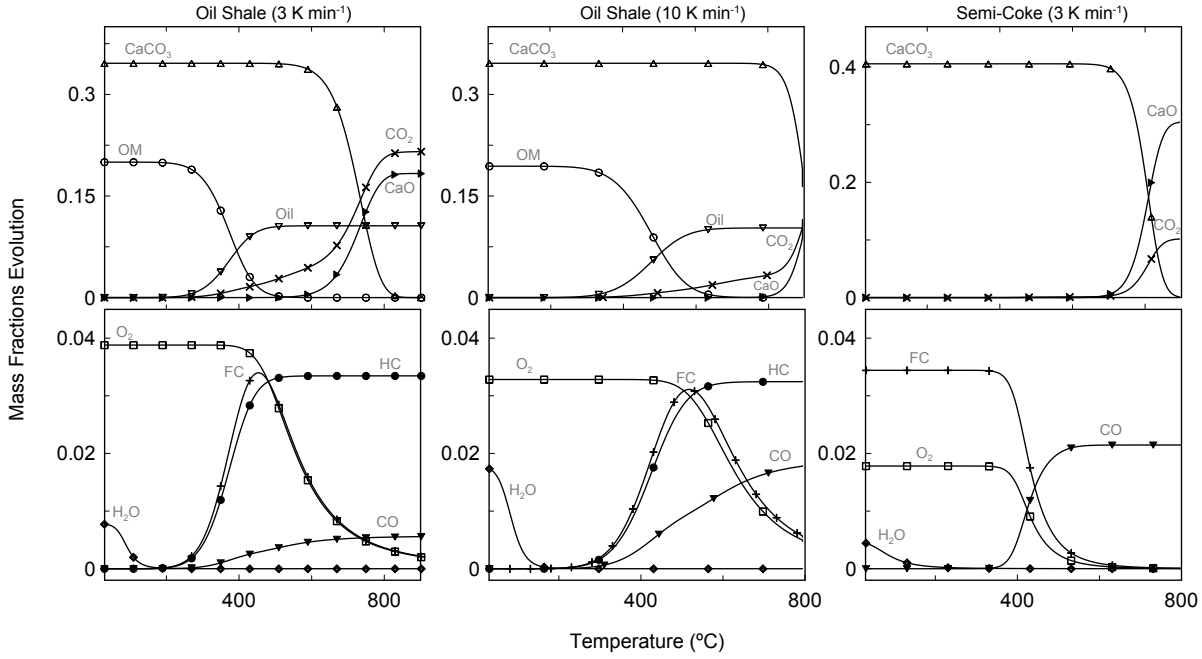

Figure 5.5: Mass fractions of different species involved in the oil shale and semi-coke combustion.

Chapter 6

Test Case - Semi-Coke Combustion in Porous Media

This chapter shows an application of semi-coke combustion in porous media using kinetic parameters estimated in the previous chapter. A complete mathematical model, developed by the *Institut de Mécanique des Fluides de Toulouse (IMFT)/ Centre de Recherche d'Albi en Génie des Procédés des Solides Divisés, de l'Énergie et de l'Environnement (RAPSODEE)* team [(Lapene, Martins, et al. [127]), (Lapene, Debenest, et al. [128]) and Martins [12]], is refined in terms of kinetic mechanism. Briefly, to solve the heat transfer and the mass transfer equations simultaneously in the reactive porous medium, a homogeneous description at the Darcy-scale is used. Thermal local-nonequilibrium transport is allowed by the model, and treated with a two temperature model: one for the gas phase and another one for the solid phase. The chemical reactions considered are drying, oxidation of fixed carbon and decarbonation reaction.

6.1 Mathematical Formulation

6.1.1 Nomenclature

m	Mass
t	Time, s
A	Frequency Factor, s^{-1}
A_{factor}	Adjust factor used to fit the heat transfer coefficient
F	View factor
I	Intensity of radiation, $kW.m^{-2}$
J	Radiosity, $W.m^{-2}$
r	Radius, m
R	Perfect gas constant, $J.K^{-1}.mol^{-1}$
x	Position in x-axis, m
P	Pressure, $kg.s^{-2}.m^{-1}$
K	Porous media permeability, m^2
Q	Heat reaction rate, $J.s^{-1}.m^{-3}$
M	Molar mass, $kg.molJ.s^{-1}.m^{-3}$
k_0	Reaction rate, s^{-1}
E	Activation Energy, J
T	Temperatura, K
v	Velocity, $m.s^{-1}$
$\dot{R}$	Reaction rate, $kg.s^{-1}.m^{-3}$
C_P	Mass heat capacity, $J.kg^{-1}.K^{-1}$
S_{spec}	Specific surface, m^{-1}
d_p	Average particle diameter, m
Pe	Peclet number
D	Dispersion coefficients, $m.s^{-1}$
h	Thermal loss through walls, $J.s^{-1}.m^{-3}.K^{-1}$
Y	Mass fraction

Greek Symbols

α	*[CO_2]/[CO]* ratio
ϵ	Volume Fraction
ε	Emissivity
μ	Viscosity, $kg.s^{-1}.m^{-1}$
Γ	Exchange coefficient, $J.s^{-1}.m^{-3}.K^{-1}$
σ	Stefan-Boltzmann constant, $W.m^{-2}.K^{-4}$
ρ	Density, $kg.m^{-3}$
λ	Thermal Conductivity, $J.m^{-1}.s^{-1}1.K^{-1}$
Φ	Radiative heat flux, $J.m^{-1}.s^{-2}$

Indices, exponents

*	Effective
s	Solid
k	Constituent *k*
g	Gas
k	*N_2, O_2, CO, CO_2, $CaCO_3$, Fuel*
T	Thermal
C	Chemical
amb	Ambient
rad	Radiation

6.1.2 Physical Model

The physical model is based on an experimental device, developed by Martins [12], to enable 1D co-current experiments; see Figures 6.1 and 6.2. It consists of a vertical cylindrical combustion chamber of 91 mm internal diameter and a height of 300 mm. The diameter is chosen to be wide enough to limit heat losses through the walls, but narrow enough to avoid the preparation of large sample quantities, and also to facilitate treatment of flue gas. It is made of a 2 mm-thick stainless steel material, surrounded by two types of insulating material: a 3 mm

thick layer of wool (Superwool 607 blanket, Thermal Ceramics, k = 0.28 $W.m^{-1}.K^{-1}$ at 982 °C) and a 50 mm thick layer of refractory fibre bloc (Kaowool HS 45 Board, Thermal Ceramics, k = 0.21 $W.m^{-1}.K^{-1}$ at 1000 °C).

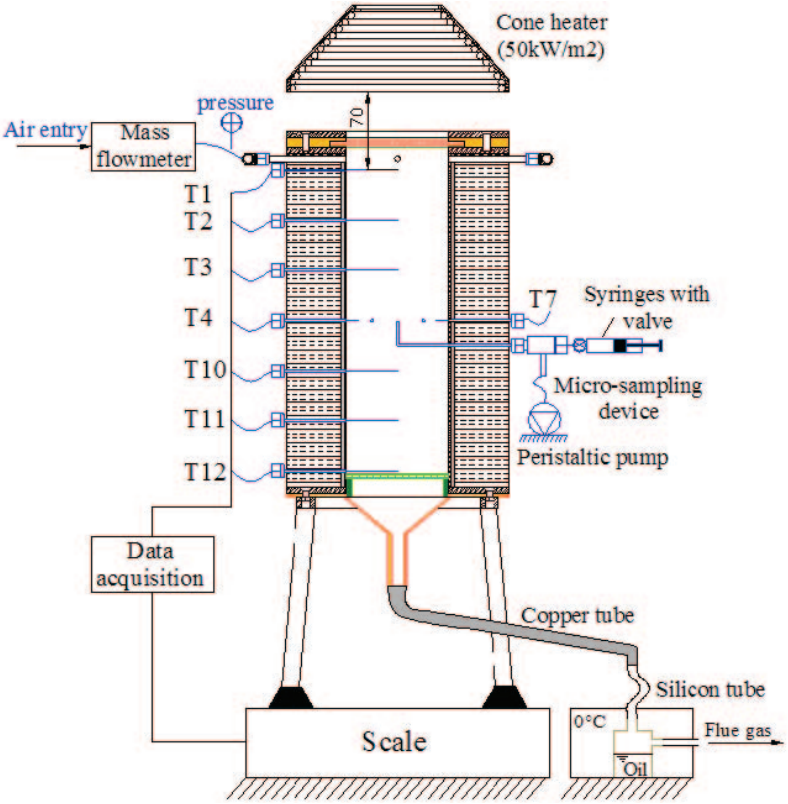

Figure 6.1: Cell of combustion in porous medium, with micro-sampling system [12].

A grate is located at the bottom of the chamber and consist of a stainless-steel mesh. It is supported by an inner ring, which in turn is supported by the lower cone of the reactor. At the bottom of the cell is placed a copper tube to start cooling the flue gas before contact with the flexible silicone tube connected to reservoirs to condense and collect liquid oil. The air entry is designed to supply uninterrupted airflow in a symmetrical way. Gas analyzers can be momentarily connected at the exit of the condensers to analyze.

The pressure at the top of the reactor and the total mass of the particle bed are continuously recorded. The reactor is finely instrumented. A group of six in-line thermocouples 0.96 mm in diameter (T_1, T_2, T_3, T_{10}, T_{11}, T_{12}) are located at Z = 0, 45 , 90 and 180, 225 and 270 mm (from top to bottom of the reactor), making it possible to measure the temperature along the axis of

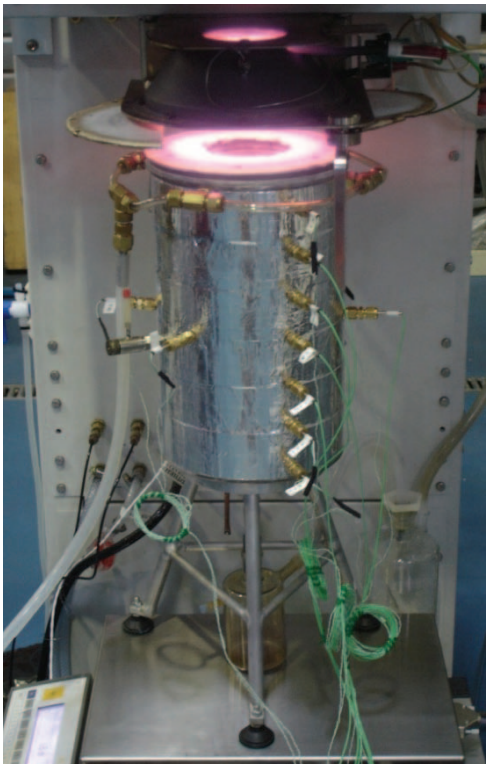

Figure 6.2: Photograph at the time of irradiation of the oil shale surface. [12].

the cell at different heights. A crown of six thermocouples, identical to the ones previously mentioned, makes it possible to measure the temperature over a horizontal cross section (at approximate middle height, Z = 135 mm) 11 mm away from the walls: this will reveal whether the combustion front progresses or not as a horizontal surface.

6.1.3 Simplifying Hypotheses

Three hypotheses are proposed in the present model:

1. *The problem is monodimensional*

   This hypothesis allows making a numerically efficient code, taking into account the couplings between heat and mass transport and the mechanisms of the chemical reactions, and especially allowing a first approach of the numerical problem. From this hypothesis it can be deduced the Equation 6.1:

$$\nabla = \frac{\partial}{\partial x} \tag{6.1}$$

2. *The porosity is constant in time and space:*

   This hypothesis is justified by the choice of the porous medium material. From this hypothesis it can be deduced the Equation 6.2:

$$\frac{\partial \epsilon_g}{\partial x} = \frac{\partial \epsilon_s}{\partial x} = \frac{\partial \epsilon_g}{\partial t} = \frac{\partial \epsilon_s}{\partial t} \tag{6.2}$$

3. *Perfect gas law:*

   This hypothesis is often considered and can be used because the pressure in the porous medium is around the atmospheric pressure. From this one it can be deduced the Equation 6.3:

$$P = \rho_g r T \;\; where \;\; r = \frac{R}{M_\beta} \tag{6.3}$$

Using these hypotheses and referring to the local-nonequilibrium model, it can be written a simplified system of conservation equations.

6.1.4 Conservation Equations

In this work, it is modelled mass and heat transport in reactive porous medium using a homogeneous description at the Darcy-scale. Local nonequilibrium transport of heat is treated with a two field temperature model, one for gas phase and one for solid phase.

It is assumed that two phases of the medium are:

- Solid phase: Semi-coke fixed carbon, $CaCO_3$ and inert matter;
- Fluid phase: gases N_2, O_2, CO, CO_2, H_2O;

Considering all approximations, it is written various balance equations as described below. The first is the mass conservation equation.

1. *Mass*

   - Continuity of the gas phase, Equation 6.4:

$$\epsilon_g \frac{\partial \rho_g}{\partial t} + \frac{\partial}{\partial x}\left(\rho_g V_g\right) = \dot{R}_g \tag{6.4}$$

   - Species transport, Equation 6.5:

$$\epsilon_g \frac{\partial \rho_g}{\partial t} Y_k + \epsilon_g \frac{\partial}{\partial x}\left(\rho_g v_g Y_k\right) - \frac{\partial}{\partial x}\left(\rho_g D_k^* \frac{\partial Y_k}{\partial x}\right) = \dot{R_{g,k}} \tag{6.5}$$

2. *Darcy equation - Neglecting gravity*, Equation 6.6:

$$v_g = -\frac{K}{\mu_g}\frac{\partial P_g}{\partial x} \tag{6.6}$$

3. *Energy equations:*

   - Gas phase energy balance, Equation 6.7:

$$\epsilon_g \left(\rho C_p\right)_g \frac{\partial T_g}{\partial t} + \epsilon_g \left(\rho C_p\right)_g v_g \frac{\partial T_g}{\partial x} = \epsilon_g \frac{\partial}{\partial x}\left(\lambda_g^* \frac{\partial T_g}{\partial x}\right) + \Gamma_{s,g}\left(T_g - T_s\right) + \epsilon_g Q_g + h(T_{amb} - T_g) \tag{6.7}$$

   - Solid phase energy balance, Equation 6.8:

$$\epsilon_s \left(\rho C_p\right)_s \frac{\partial T_s}{\partial t} = \epsilon_s \frac{\partial}{\partial x}\left(\lambda_s^* \frac{\partial T_s}{\partial x}\right) + \Gamma_{g,s}\left(T_s - T_g\right) + \epsilon_s Q_s + h(T_{amb} - T_s) \tag{6.8}$$

4. *Perfect gas law (PGL)*, Equation 6.9:

$$P_g = \rho_g \frac{P}{\bar{M}_g} T_g \tag{6.9}$$

   The pressure equation is obtained by combining Equations 6.8 and 6.9, resulting in Equation 6.10:

$$\frac{\epsilon_g \bar{M}_g}{R T_g}\frac{\partial P_g}{\partial t} - \frac{\epsilon_g \bar{M}_g P_g}{R T_g^2}\frac{\partial T_g}{\partial t} + \frac{\epsilon_g P_g}{R T_g}\frac{\partial \bar{M}_g}{\partial t} + \frac{\partial}{\partial x}\left(-\rho_g \frac{K}{\mu_g}\frac{\partial P_g}{\partial t}\right) = \dot{R}_g \tag{6.10}$$

   Thus, the equation PGL can be reformulated as Equation 6.11:

$$\rho_g = \frac{P_g \bar{M}_g}{T_g R} \tag{6.11}$$

6.1.5 Initial and Boundary Conditions

Restricting the attention to one dimensional solution, initial and boundary conditions at inlet and outlet of the reactor are formulated as follows:

- For Equation 6.5, it has Equations 6.12 to 6.16:

  - Initial condition:

$$At\ t = 0\ and\ \forall x,\ Y_k = {Y_k}^{amb} \tag{6.12}$$

  - Boundary conditions:

If $|Pe_C| < 1$ then:

$$Y_k|_{x=0} = Y_k|_{x=L} = {Y_k}^{amb} \tag{6.13}$$

If $|Pe_C| > 1$ and $v_g > 0$ then:

$$Y_k|_{x=0} = {Y_k}^{amb}$$

$$at\ x = L,\ Dankwerts\ \ conditions \tag{6.14}$$

If $|Pe_C| > 1$ and $v_g < 0$ then:

$$at\ x = 0,\ Dankwerts\ \ conditions$$

$$Y_k|_{x=L} = {Y_k}^{amb} \tag{6.15}$$

with:

$${Y_k}^{amb} = \begin{cases} Y_{N_2} \text{ in ambient air for } k = 1 \\ Y_{O_2} \text{ in ambient air for } k = 2 \\ \text{else } 0 \end{cases} \tag{6.16}$$

- For Equation 6.6, it has Equations 6.17 and 6.18:

  - Initial Condition:

$$At\ t = 0\ and\ \forall x,\ v_g = 0 \tag{6.17}$$

  - Boundary conditions:

$$v_g|_{x=0} = v_e^*$$

$$v_g|_{x=L} = -\frac{K}{\mu_g}\left.\frac{\partial P_g}{\partial x}\right|_{x=L} \tag{6.18}$$

    with v_e^* is the entry velocity directly linked to entry airflow that is equal v_e if $t > t_{all.}$, else $v_e/2$.

- For Equation 6.7, it has Equations 6.19 to 6.22:

  - Initial Condition:

$$At\ t = 0\ and\ \forall x\ T_g = T_g^{amb} \tag{6.19}$$

  - Boundary conditions:

    If $|Pe_T| < 1$ then:

$$T_g|_{x=0} = T_g|_{x=L} = T_g{}^{amb} \tag{6.20}$$

    If $|Pe_T| > 1$ and $v_g > 0$ then:

$$T_g|_{x=0} = T_g{}^{amb}$$

$$at\ x = L,\ Dankwerts\ \ conditions \tag{6.21}$$

    If $|Pe_T| > 1$ and $v_g < 0$ then:

$$at\ x = 0,\ Dankwerts\ \ conditions$$

$$T_g|_{x=L} = T_g{}^{amb} \tag{6.22}$$

where $T_g{}^{amb}$ is the ambient gas temperature.

- For Equation 6.8, it has Equations 6.23 to 6.25:

  - Initial Condition:

$$At\ t = 0\ and\ \forall x,\ T_s = T_s{}^{amb} \tag{6.23}$$

  - Boundary conditions:

If $t < t_{all.}$ then:

$$-\lambda_s^* \left.\frac{\partial T_s}{\partial x}\right|_{x=0} = \Phi_{rad}$$

$$\left.\frac{\partial T_s}{\partial x}\right|_{x=L} = 0 \tag{6.24}$$

else:

$$\left.\frac{\partial T_s}{\partial x}\right|_{x=0} = \left.\frac{\partial T_s}{\partial x}\right|_{x=L} = 0 \tag{6.25}$$

where $t_{all.}$ is the duration of the time ignition.

- For Equation 6.10, it has Equations 6.26 and 6.27:

  - Initial Condition:

$$At\ t = 0\ and\ \forall x,\ P_g = P^{amb} \tag{6.26}$$

  - Boundary conditions:

$$\left.\frac{\epsilon_g \bar{M}_g}{RT_g}\frac{\partial P_g}{\partial t}\right|_{x=0} - \left.\frac{\epsilon_g \bar{M}_g P_g}{RT_g^2}\frac{\partial T_g}{\partial t}\right|_{x=0} + \left.\frac{\epsilon_g P_g}{RT_g}\frac{\partial \bar{M}_g}{\partial t}\right|_{x=0} + \left.\frac{\partial}{\partial x}\left(-\rho_g v_g\right)\right|_{x=0} = \left.\dot{R}_g\right|_{x=0}$$

$$P_g|_{x=L} = P^{amb} \tag{6.27}$$

- For Equation 6.9, it has Equations 6.28 and 6.29:

  - Initial Condition:

$$At\ t = 0\ and\ \forall x,\ \rho_g = \rho^{amb} \tag{6.28}$$

  - Boundary conditions:

$$\rho_g|_{x=0} = \frac{P_g|_{x=0}\,\bar{M}_g}{T_g|_{x=0}\,R}$$

$$\rho_g|_{x=L} = \frac{P_g|_{x=L}\,\bar{M}_g}{T_g|_{x=L}\,R} \tag{6.29}$$

    where ρ^{amb} is the air density at ambient temperature.

The system equation is solved to find the following unknown variables dependent on the time t and space x: ρ_g, P_g, v_g, Y_k, T_g and T_s.

The physical variables calculated are: ϵ_g, ϵ_s, $\dot{R}_g$, D_k^*, $\dot{R}_{g,k}$, K, μ_g, $C_{p,g}$, $C_{p,s}$, λ_g^*, λ_s^*, $\Gamma_{s,g}$, $\Gamma_{g,s}$, Q_g, Q_s, R, and $\bar{M}_g$.

6.1.6 Empirical Data

Several physical variables are determined by empirical laws [73].

Dynamic viscosity of the gas mix, Equation 6.30:

$$\mu_g = \frac{1.458 \times 10^{-6} \times T_g^{3/2}}{110.4 + T_g} \tag{6.30}$$

Heat capacity of the gases, Equations 6.31 to 6.34 :

$$C_{pg,N_2} = 4.1868 \times 16 \times (6.76 + 0.606 \times 10^{-3} \times T_g + 0.13 \times 10^{-6} \times T_g^2) \tag{6.31}$$

$$C_{pg,O_2} = 4.1868 \times 36 \times (8.27 + 0.258 \times 10^{-3} \times T_g - \frac{1.877 \times 10^5}{T_g^2}) \tag{6.32}$$

$$C_{pg,CO} = 4.1868 \times 28 \times (6.60 + 1.2 \times 10^{-3} \times T_g) \tag{6.33}$$

$$C_{pg,C0_2} = 4.1868 \times 44 \times (7.70 + 5.3 \times 10^{-3} \times T_g - 0.83 \times 10^{-6} \times T_g^2) \tag{6.34}$$

Thermal conductivity of the gases, Equations 6.35 to 6.38:

$$\lambda_{g,N_2} = \frac{3.33143 \times 10^{-4} \times 1T_g^{0.7722}}{1 + \frac{16.323}{T_g} + \frac{373.72}{T_g^2}} \tag{6.35}$$

$$\lambda_{g,0_2} = \frac{4.4994 \times 10^{-4} \times 1T_g^{0.7456}}{1 + \frac{56.699}{T_g}} \tag{6.36}$$

$$\lambda_{g,CO} = \frac{5.9882 \times 10^{-4} \times 1T_g^{0.6863}}{1 + \frac{57.13}{T_g} + \frac{501.92}{T_g^2}} \tag{6.37}$$

$$\lambda_{g,CO_2} = \frac{3.69 \times 1T_g^{-0.3838}}{1 + \frac{964}{T_g} + \frac{1.86 \times 10^6}{T_g^2}} \tag{6.38}$$

Heat transfer coefficient, Equations 6.39 and 6.40:

$$\Gamma_{s,g} = A_{factor} \frac{\lambda_g}{d_p} \left(2 + 1.1 Re^{0.6} Pr^{1/3}\right) \tag{6.39}$$

$$A_{factor} \lambda_g^* \frac{\lambda_g}{d_p} \left[2 + 1.1 \left(\frac{\rho_g v_g d_p}{\mu}\right)^{0.6} \left(\frac{\mu C_{P_g}}{\lambda_g}\right)^{1/3}\right] \tag{6.40}$$

where A_{factor} is the adjust factor used to fit the solution of the heat exchange, $\Gamma_{s,g}$ between the two phases, solid and gas.

The global variables are calculated by mixing laws resulting in Equations 6.41 to 6.43:

$$C_{pg} = \sum_k Y_k C_{pg,k} \tag{6.41}$$

$$\lambda_g = \sum_{i=1}^{nbgaz} \frac{X_i \lambda_{g,i}}{\sum_j^{nbgaz} X_i A_{ij}} \tag{6.42}$$

$$A_{ij} = \frac{\left[1 + \left(\lambda_{g,i}/\lambda_{g,j}\right)^{1/2} \left(M_{g,i}/M_{g,j}\right)^{1/4}\right]^2}{\left[8\left(1 + M_{g,i}/M_{g,j}\right)\right]^{1/2}} \tag{6.43}$$

where $A_{i,j}$ is a factor taking into account in the calculation of λ_g, $nbgaz$ is the number of gaseous species, X_i is the molar fraction for the species i. Thus, the expressions of the macroscopic coefficient are represented by Equations 6.44 and 6.45:

$$\lambda_g^* = \epsilon_g \lambda_g \tag{6.44}$$

$$\lambda_s^* = \epsilon_s \lambda_s \tag{6.45}$$

Thus, a standard sequential non-iterative operator splitting scheme is used to solve the resulting non-linear problem. Firstly is solved the mass and energy transports term, thanks to a transport operator which uses a full sequential approach and finite volume schemes [12, 129]. Finally, the chemistry operator, which is reduced to a stiff ODE system, is solved by the LSODES FORTRAN library, which uses backward differentiation formulas by Gear.

6.2 Model Parameters Determination

6.2.1 Parameters Determined Experimentally by Martins et al. [13, 16]

Physical properties:

1. Apparent density of the packed bed, 1168 $kg.m^{-3}$;
2. Bed porosity, 0.472 %;
3. Real density adopted 2214 $kg.m^{-3}$;

Heat transfer properties:

1. Oil shale conductivity: λ_s= 0.89 $W.m^{-1}.K^{-1}$;
2. Heat transfer coefficient $\Gamma_{s,g}$=0.544 $kW.m^{-2}.K$.

Chemical properties:

1. Reaction heat of decarbonation reaction - 589 $kJ.kg^{-1}$;
2. Reaction heat of char oxidation + 19470 $kJ.kg^{-1}$.

6.2.2 Parameters Fitting

A number of parameters in the model are adjusted through a procedure of fitting the model to the experimental results. This is carried on when it is considered that the value determined directly is uncertain, and that their adjustments lead to better model results. Table 5.3 in the chapter 5 shows the kinetic parameters estimated for semi-coke combustion. In this table, only the parameters n_4 and n_5 are changed to n_4=1.81 and n_5=1.86 due to the computational incapacity. However, these values are in agreement with the estimation error for each one.

6.2.3 Parameters from the Numerical Model

Once these parameters are fitted, the modeling is run and the results interpreted into detailed to gain information about the front structure. Table 6.1 to Table 6.4 present the input data used.

Table 6.1: Values of numerical parameters used in the model for semi-coke combustion.

Numerical Parameters	**Description**	**Unit**
300	Number of nodes	–
dt=5x10^{-3}	Time step	–
dx=1x10^{-3}	Space step	m
t_{exp}=3000	Time of experiment	s

Table 6.2: Values of physical parameters used in the model for semi-coke combustion.

Physical Parameters	**Description**	**Unit**
t_{ig}=378	Ignition time duration	s
0.30	Reactor length	m
P_{atm}=1.013x10^5	Atmospheric pressure	Pa
T_{amb}=293.15	Ambient temperature	K
V_{in}=0.01215	Entry velocity	m.s^{-1}
S_{spec}=2321.26	Specific surface	m^{-1}
ϵ_s=0.47	Bed porosity	–
d_p=750	Average particle diameter	μm

Table 6.3: Values of heat transfer properties used in the model for semi-coke combustion.

Heat transfer properties	**Description**	**Unit**
ρ_s=2214	Solid density	kg.m^{-3}
λ_s=0.89	Solid conductivity	W.m^{-1}.K^{-1}
C_{P_s}=0.585xT+664.5	Heat capacity	J.kg^{-1}.K^{-1}
$\Gamma_{s,g} = 55.\frac{\lambda_g\left(2+1.1Re^{0.6}Pr^{1/3}\right)}{d_p}$	Heat transfer coefficient between solid and gas	W.$m^{-2}K^{-1}$

Table 6.4: Values of chemical parameters used in the model for semi-coke combustion.

Chemical Parameters	**Description**	**Unit**
Y_{CaCO_3}=40.57	Calcite mass fraction	kg/kg
Y_{FC}=3.44	Fixed carbon mass fraction	kg/kg
Y_{IM}=55.55	Inert matter mass fraction	kg/kg
Y_{H_2O}=0.44	moisture mass fraction	kg/kg
fr=0.96	Ratio of the products of combustion: CO/CO_2	–
19470	Reaction heat for char oxidation	kJ.kg^{-1}
-589	Reaction heat for decarbonation process	kJ.kg^{-1}
$C + \left[\frac{fr}{2} + (1-fr)\right] O_2 \rightarrow frCO + (1-fr)CO_2$	Fixed carbon oxidation reaction	–
$CaCO_{3_s} \rightarrow 0.56CaO_s + 0.44CO_{2_g}$	Decarbonation reaction	–

6.2.4 Model for Ignition Process

To start the combustion process, Martins [12] has used a sophisticated ignition device, called Cone Calorimeter. On the ignition time, the radiant conical heater temperature has been adjusted to 845 °C to impose a heat flux of 45 to 50 $kW.m^{-2}$ over the top surface of the oil shale; see Figure 6.3. This radiative flux has been generated by a metal surface called a cone heater, heated at high temperature; it has previously been calibrated using a water-cooled fluxmeter. The radiative flux crosses a quartz porthole that ensures the sealing of the closure, as shown in Figure 6.2. The time of irradiation was 220 s, controlled by opening/closing the insulator shield.

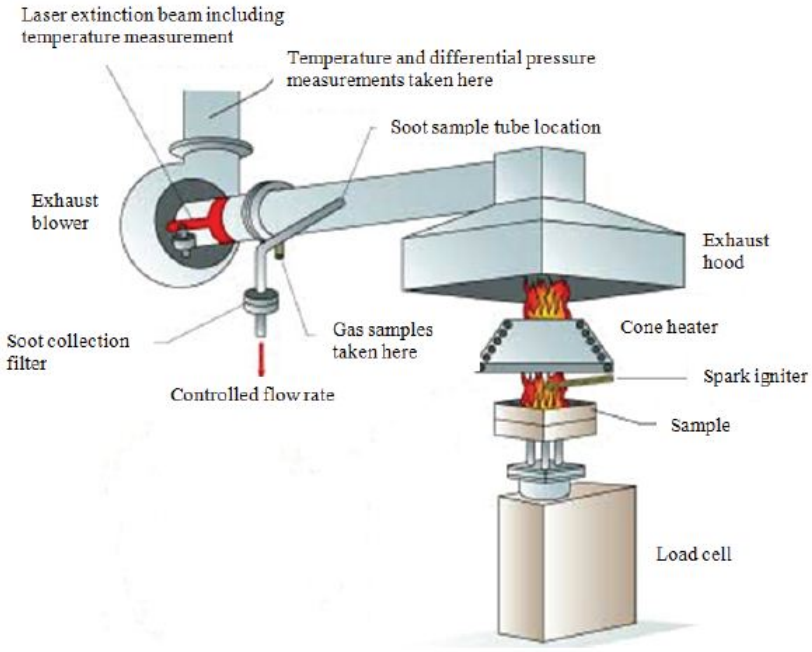

Figure 6.3: Original schematic diagram of the cone calorimeter [12].

To compute, numerically, radiation exchange between any two surfaces, it is necessary to introduce the concept of a *view factor*. The *view factor* F_{ij} is defined as the fraction of the radiation leaving surface *i* that is intercepted by surface *j*. In this work, the *view factor* is considered using a disk approximation to coaxial annular ring on parallel disk [14], as shown in the Figure 6.4.

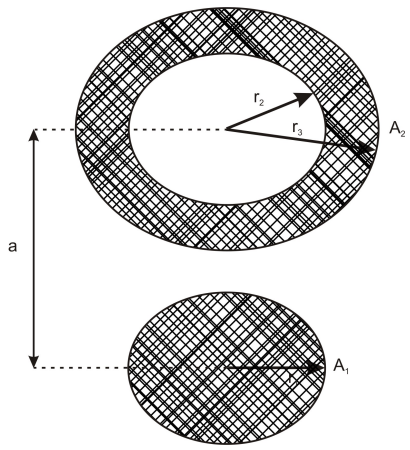

Figure 6.4: Disk to coaxial annular ring on parallel disk to determinate the view factor [14].

Thus, the *view factor* for this configuration is according Equations 6.46 to 6.49.

$$F_{21} = \frac{1}{2}\{R_3^2 - R_2^2 - \left[\left(1 + R_3^2 + H^2\right)^2 - 4R_3^2\right]^{1/2} + \left[\left(1 + R_2^2 + H^2\right)^2 - 4R_2^2\right]^{1/2}\} \quad (6.46)$$

$$F_{12} = \frac{A_1}{A_2}F_{21} \quad (6.47)$$

$$F_{13} = 1 - F_{12} \quad (6.48)$$

$$F_{23} = F_{13} \quad (6.49)$$

at $H = \frac{a}{r_1}$, $R_2 = \frac{r_2}{r_1}$, $R_3 = \frac{r_3}{r_1}$, surface areas $A_1 = \pi r_1^2$ and $A_2 = \pi(r_3^2 - r_2^2)$ with r_1=0.045 m, r_2=0.025 m, r_3=0.065 m and center distance between parallel disk a=0.07 m.

To evaluate the radiation heat flux, Φ, is necessary to solve the following equations, represented by Equations 6.50 to 6.57 where *I* is the radiation intensity defined by Equation 6.50, *J* is the radiosity defined by Equation 6.56, ε_1=0.9, ε_2=0.95, T_1=1118 K, T_3=293 K and *Stefan-Boltzmann constant* σ=5.67x10^{-8} $W.m^{-2}.K^{-4}$. The other letters are only to simplify the radiosity factor and they do not have a specific meaning.

$$I = \frac{\varepsilon_1}{(1 - \varepsilon_1)} + F_{12} + F_{13} \quad (6.50)$$

$$B = \frac{\varepsilon_2}{(1 - \varepsilon_2)} + \frac{A_2}{A_1}F_{12} + F_{23} \quad (6.51)$$

$$C = B + \frac{A_2}{A_1}\frac{F_{12}^2}{I} \tag{6.52}$$

$$D = \frac{\left\{\left(\frac{A_2}{A_1}F_{12}\right)\left[\left(\frac{\varepsilon_1\sigma T_1^4}{1-\varepsilon_1}\right) + (F_{13}\sigma T_3^4)\right]\right\}}{I} \tag{6.53}$$

$$E = F_{23}\sigma T_3^4 \tag{6.54}$$

$$N = \frac{\varepsilon_2\sigma T(t)^4}{1-\varepsilon_2} \tag{6.55}$$

$$J(t) = \frac{(D+E+N)}{C} \tag{6.56}$$

$$\Phi(t) = \frac{\varepsilon_2(-\sigma T(t)^4) + J(t)}{1-\varepsilon_2} \tag{6.57}$$

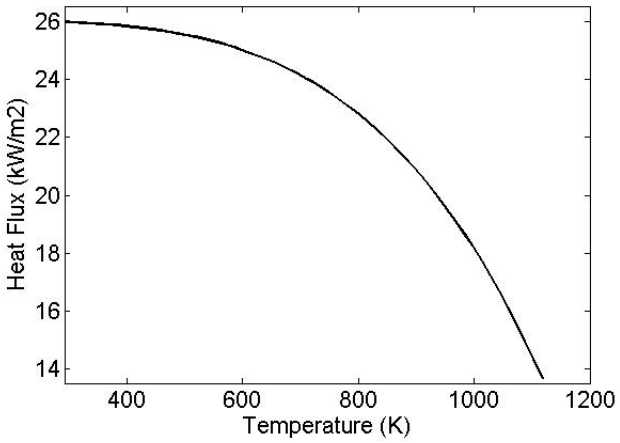

Figure 6.5: Radiative heat flux evolution with the temperature.

Other formulations for *view factors* do not involve the temperature variation. In this work, radiation heat flux, Equation 6.57 varies with temperature (see Figure 6.5). This a model more realistic than the one applied by Martins [12], where the author had used a constant radiation heat flux, overestimating the process. Figure 6.5 shows that in t=0 s and initial temperature of 293 K, radiation heat flux is maximum with Φ=26 $kW.m^{-2}$. As the temperature of receiving surface increases, radiation heat flux tends to decrease. It is important to note that the radiation

heat flux is applied only to reach the ignition temperature. After t=378 s, as shown in the Table 6.2, this flux is stopped.

6.2.5 Influence of the Kinetic Mechanism in the Temperature Evolution and Temperature Profile

Concerning to the temporal evolution of temperature, Figure 6.6 shows the results for semi-coke combustion using a porous bed with composition of 0.44 wt.% of H_2O, 3.44 wt.% of fixed carbon, 40.56 wt.% of $CaCO_3$ and 55.56 wt.% of inert material (see Table 5.1). The Darcy velocity adopted is 0.023 $m.s^{-1}$ at 20 °C, or 0.108 $m.s^{-1}$ at 1000 °C with a flow rate of 1461 $lmin^{-1}$ at STP (Standard Temperature Pressure) for 1 m^2 of section. After ignition, in the top of the reactor (with z=0 mm and where the first thermocouple is located and represented by T_1), a combustion front starts to propagate through the bed. For the other thermocouples (T_2, T_3, T_{10}, T_{11} and T_{12}), peaks at a temperature near to 800 °C were observed. The nomenclature and numeration of the thermocouples was took of Martins [12] and maintained here to compare the results. Apparently, the combustion process is in an established regime. The experiments developed by Martins et al. [13, 16] and applied by Sennoune et al. [53] have found a temperature peak up to 837 °C using a bed of semi-coke with 0.45 wt.% of volatiles matter, 3.475 wt.% of fixed carbon, 42.41 wt.% of $CaCO_3$ and 53.76 wt.% of inert material. The Darcy velocity has the same value of 0.023 $m.s^{-1}$ at 20 °C. Thus, the results presented here shows a good coherence with the experiments made by Sennoune et al. [53].

Figure 6.7 shows axial temperature profiles for the solid and the gas along the reactor axis at different times. In this figure, temperature decreases downstream the front, while hot zone upstream the front becomes getting larger as the front progresses, confirming that reaction zone propagates more rapidly than heat exchange zone, as indicated in the Figure 2.13(a) presented previously and found by Martins [12].

The temperature level is almost the same once combustion process is well established, near to Z= 45 mm until 300 mm. Moreover, Figure 6.7 still shows that the difference between gas

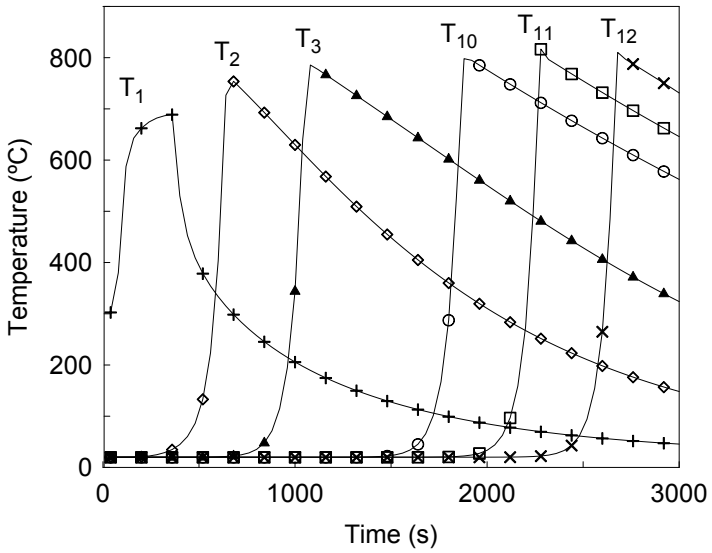

Figure 6.6: Temperature evolution for semi-coke combustion in fixed bed.

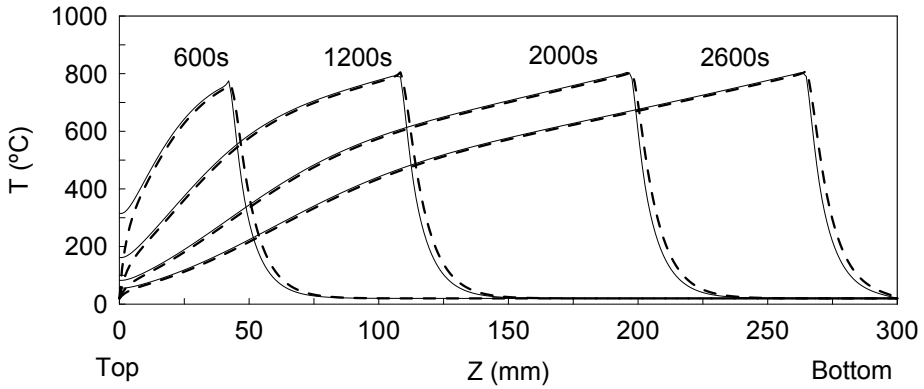

Figure 6.7: Temperature profile in the bed where the line $(-)$ is the solid temperature profile and the dashed line $(--)$ is the gas temperature profile.

temperature profile and solid temperature profile is very small. Thus, the hypotheses of local thermal equilibrium is a good approximation for this case.

6.2.6 Combustion Front Velocity

The model predicts a constant numerical front velocity in the order of 5.958 $mm.min^{-1}$). This value is higher than the ones found by Sennoune et al. [53] (3.77 $mm.min^{-1}$). However, this difference is expected because it depends on the oxygen fraction and the bed composition, as shown by Schult et al. [50] and Johnson et al. [51].

6.3 Parametric Study

This topic is dedicated to the observation of the numerical model behavior when a parameter is changed. In this section, the entry air velocity is varied between 0.01215 to 0.0972 $m.s^{-1}$ to verify its influence in the numerical stability. In addition, the amount of fixed carbon also is varied in the range of 1.80 wt.% until 3.44 wt.% to verify which is the minimum amount of fixed carbon to start the combustion front.

6.3.1 Influence of Entry Air Velocity

Figure 6.8(a) illustrates the influence of the entry air velocity. The model indicates that increasing the entry air velocity from 0.01215 to 0.0729 $m.s^{-1}$ results in an increase of almost 170 ^{o}C in the temperature peak, using the thermocouple T_{10} with reference. Concerning to the combustion front velocity, it is observed that when the entry air velocity increases, the combustion front velocity also increases, as observed in the Figure 6.8(a).

Using an entry air velocity of 0.0972 $m.s^{-1}$, the model became unstable (see Figure 6.8(b)) and the simulation is stopped suddenly. Thus, it is possible that 0.0972 $m.s^{-1}$ is the upper limit for air velocity for a numerical stable propagation of a combustion front.

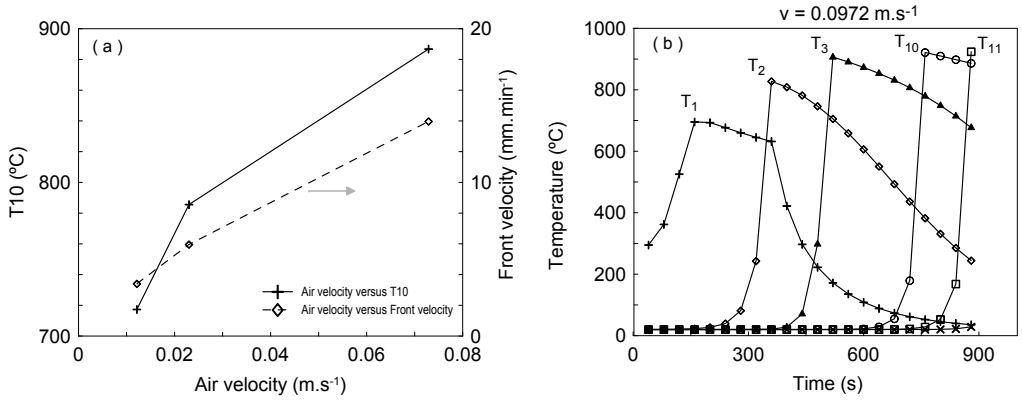

Figure 6.8: Evolution of temperature varying the air velocity.

6.3.2 Influence of Fixed Carbon Fraction

By varying the amount of fixed carbon, Figure 6.9(a) shows that, for 3.44 wt.% of fixed carbon, the combustion front proceeds normally and the temperature is up to 800 ^{o}C. Decreasing the amount of fixed carbon, the front temperature decreases gradually reaching almost 460 ^{o}C with 1.90 wt.% of fixed carbon. Finally, with 1.80 wt.% of fixed carbon, there is no combustion front propagation due to the low amount of fixed carbon (see Figure 6.9(b)). Regarding to the front velocity, Figure 6.9(a), it has a low variation being in 5.472 $mm.min^{-1}$ with 1.9 wt.% of fixed carbon, reaching a maximum value, 6.72 $mm.min^{-1}$, with 2.5 wt.% of fixed carbon and decreasing until 5.958 $mm.min^{-1}$ for 3.44 wt.% of fixed carbon, as observed by Fadaei et al. [130].

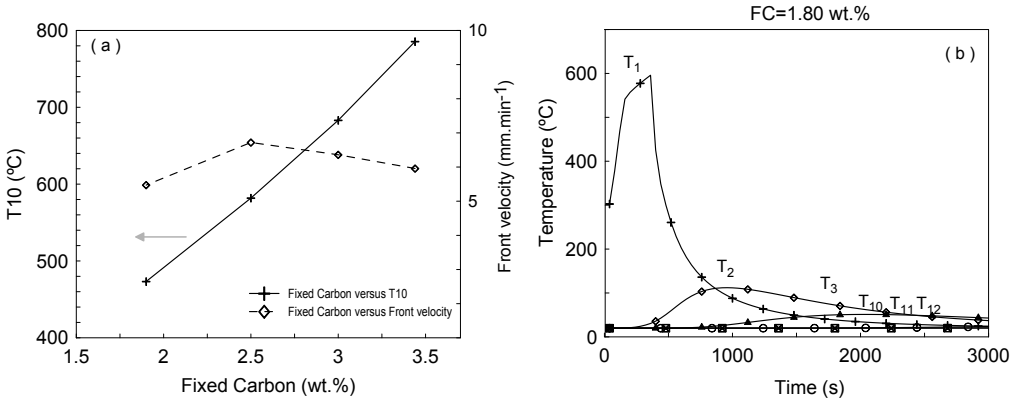

Figure 6.9: Evolution of temperature varying the amount of fixed carbon and fixing the air velocity in v=0.023 $m.s^{-1}$.

Chapter 7

Conclusions and Perspectives

In the last part of this work, the main developments and results are summarized. Possible directions for further research are given.

7.1 Conclusion

A computational methodology that allows formulation and optimization of the pyrolysis and combustion pathways for oil shale and its semi-coke was developed with success. The main contribution of this methodology lies in combining TG/DSC data with a detailed determinant analyze to estimate the kinetic parameters.

Regarding to the oil shale pyrolysis, a new three-step reaction mechanism was proposed and tested. The sensitivity and determinant analyzes were used to show the feasibility of the estimation, as well as a first evaluation about where the temperature range for each reaction starts and ends. Since the Arrhenius parameters were estimated with accuracy, a low error for activation energies and reaction orders in the three reactions were obtained. The maximum estimation error established was up to 2.6% for the pre-exponential factor A_2. For reaction orders examined in this work, all reactions are of order superior to one.

By exploiting the determinant analyze for oil shale pyrolysis, it was established that the

evaporation reaction may occur between 60 and 195 ± 5 °C. It was reasonable to consider that the pyrolysis reaction takes place from 195 ± 5 to 570 ± 40 °C. The hypothesis that the carbonates are essentially $CaCO_3$ also reasonable. For this reaction, the established temperature range was 570 ± 40 to 800 °C. The activation energies for pyrolysis and decarbonation reactions were 86.05 $kJmol^{-1}$ and 251.20 $kJmol^{-1}$ respectively.

About the mass fraction evolution, the amount of fixed carbon and volatile matter formed in the pyrolysis reaction were 4.10 wt.% and 12.76 wt.% respectively. Moreover, the amount of CO_2 released in the decarbonation reaction was 14.66 wt.%.

Concerning to the oil shale and semi-coke combustion, 4-steps combustion mechanisms for oil shale and 3-steps combustion mechanisms for its semi-coke were formulated, and then optimized. The fitted-lines were obtained with low residual errors. The sensitivity analyze confirmed higher errors in the estimation of the pre-exponential factors, otherwise it was found for activation energies, reaction orders and stoichiometric coefficients.

The activation energy for the fixed carbon oxidation in oil shale combustion was around 100 $kJmol^{-1}$, and for the semi-coke combustion about 211 $kJmol^{-1}$. Taking into consideration that the carbonates are essentially composed of calcite ($CaCO_3$), its activation energy varies between 162 - 418 $kJmol^{-1}$. The estimated values for fr in oil shale combustion suggest that the mass fraction of fixed carbon - formed during pyrolysis reaction - is oxidized into CO_2. For the semi-coke combustion almost all carbon is oxidized into CO.

The mass fraction of fixed carbon (between 3.1 - 3.4 wt.% of OS) predicted using estimated parameters proved to be reasonable when compared with experimental measures given in the literature for the same oil shale deposits. Considering the estimated parameters, as well as a heating rate at 3 $Kmin^{-1}$, in relation to an oil shale containing about 20 wt.% of organic matter and 34.6 wt.% of $CaCO_3$, the species mass fractions formed during combustion process were 3.4 wt.% of fixed carbon, 10.6 wt.% of Oil, 3.3 wt.% of hydrocarbons and 1.8 wt.% of CO. The fraction of CO_2 formed accounts a total of 21.6 wt.%. For a semi-coke containing 3.4 wt.% of fixed carbon and 40.6 wt.% of $CaCO_3$, its combustion formed 2.1 wt.% of CO. The CO_2 fraction from oxidation and decarbonation reactions accounts 10.2 wt.%, considering that $\gamma =$ 0.75 in the decarbonation reaction.

Concerning to the numerical model in porous media for semi-coke combustion, a new model of the radiation heat flux was proposed. Also, a parametric study was made to identify the dependence between temperature profile and entry air velocity, and temperature profile and fixed carbon fraction. Thus, varying the entry air velocity of 0.01215 to 0.0972 $m.s^{-1}$, it was established that the better temperature profile was found for 0.023 $m.s^{-1}$, and for 0.0978 $m.s^{-1}$ temperature profile is unstable, occurring an abrupt stop in the numerical simulation. In addition, when the air velocity increases, a peak temperature also increases, maintaining up to 880 ^{o}C for 0.0729 $m.s^{-1}$. About the amount of fixed carbon, the combustion front propagation is established with the amount of fixed carbon greater than 1.8 wt.%.

Therefore, the parametric study confirmed that the front propagation was controlled by air supply and amount of fixed carbon.

7.2 Perspectives

The estimation of kinetic parameters are extremely important in combustion processes. Several parameters estimation methods used until today involve only the utilization of reaction mechanism with one reaction step. On the other hand, the parameters estimation using inverse problems (Levenberg-Marquardt algorithm and genetic algorithm) may use many reaction steps. This work has presented a kinetic parameter estimation using the Levenberg-Marquardt algorithm for oil shale pyrolysis and oil shale and its semi-coke combustion and also the application of these kinetic parameters in a code in porous media developed by Martins et al. [13, 16, 127, 128, 12]. The results have shown a good agreement with the ones found in the literature. However, some points have to be taken into consideration.

Code - Parameters Estimation

- To estimate the stoichiometric parameter α for each specie in the pyrolysis reaction of the oil shale.
- To propose a reaction mechanism more complex, taking into consideration the volatiles

oxidation;

- To use other parameters estimation methods such as genetic algorithm along with other solid fuels;

Code - Solid Combustion in Porous Media

- Implementation of the proposed and estimated reaction mechanism for oil shale combustion.

Bibliography

[1] D. Woynillowicz, C. Severson-Baker, and M. Raynolds, *Oil Sands Fever - The Environmental Implications of Canada's Oil Sands Rush*. Alberta - Canada: The Pembina Institute, 2005.

[2] U. E. P. Agency, *Municipal Solid Waste Generation, Recycling, and Disposal in the United States: Facts and Figures*. 2009.

[3] C. for Sustainable Systems, *Municipal Solid Waste Factsheet*. University of Michigan, No. CSS04-15, 2011.

[4] J. T. Bartis, T. LaTourrette, L. Dixon, and C. G. Peterson, D. J., *Oil Shale Development in the United States - Prospects and Policy Issues*. Prepared for the National Energy Technology Laboratory of the U.S. Department of Energy by the Rand Corporation, Santa Monica, California, 2005.

[5] H. Johnson, P. Crawford, and J. Bunger, *Strategic significance of America's oil shale resource. Volume I: Assessment of strategic issues*. Office of Strategic Petroleum Reserves, U.S. Department of Energy, contract DE- AC01-03FE67758, 2004.

[6] J. H. Gary, *An Assessment of Oil Shale Technologies*. United States Congress - Office of Technology Assessment, 1980.

[7] U. Cements, *Available in http://www.understanding-cement.com [Accessed october 20, 2011]*.

[8] T. Xia, M. Greaves, A. Turta, and C. Ayasse, "Thai–a [']short-distance displacement' in situ combustion process for the recovery and upgrading of heavy oil," *Chemical Engineering Research and Design*, vol. 81, no. 3, pp. 295 – 304, 2003.

[9] STAR, *Self-Sustaining Smoldering Treatment for Active Remediation*. Available in http://star.siremlab.com/overview.php [Accessed January 06, 2012].

[10] A. Aldushin, I. Rumanov, and B. Matkowsky, "Maximal energy accumulation in a superadiabatic filtration combustion wave," *Combustion and Flame*, vol. 118, no. 1?2, pp. 76 – 90, 1999.

[11] P. S. Sarathi, *In-Situ Combustion Handbook - Principles and Practices*. U.S. Department of Energy - Oklahoma Tulsa, 1999.

[12] M. F. Martins, *The structure of a combustion front propagating in a fixed bed of crushed oil shale: co-current configuration*. PhD thesis, Université de Toulouse, Centre RAPSODEE, UMR EMAC-CNRS 2392, 2008.

[13] M. Martins, S. Salvador, J.-F. Thovert, and G. Debenest, "Co-current combustion of oil shale - part 1: Characterization of the solid and gaseous products," *Fuel*, vol. 89, no. 1, pp. 144 – 151, 2010.

[14] S. Abishek, K. S. Ramanujam, and S. S. Katte, "View factors between disk/rectangle and rectangle in parallel and perpendicular planes," *J. Thermophsics*, vol. 21, no. 1, pp. 236 – 239, 1995.

[15] Y. H. Khraisha, "Batch combustion of oil shale particles in a fluidized bed reactor," *Fuel Processing Technology*, vol. 86, no. 6, pp. 691 – 706, 2005.

[16] M. Martins, S. Salvador, J.-F. Thovert, and G. Debenest, "Co-current combustion of oil shale - part 2: Structure of the combustion front," *Fuel*, vol. 89, no. 1, pp. 133 – 143, 2010.

[17] M. V. Kok, G. Guner, and S. Bagci, "Combustion kinetics of oil shales by reaction cell experiments," *Estonian Academy Publishers*, vol. 25, p. 516, 2008.

[18] A. Saoiabi, A. Doukkali, M. Hamad, A. Zrineh, M. Ferhat, and Y. Debyser, "Schistes bitumineux de timahdit (maroc) : composition et propriétés physicochimiques timahdit (morocco) oil shales: composition and physicochemical properties.," *Comptes Rendus de l'Académie des Sciences - Series IIC - Chemistry*, vol. 4, no. 5, pp. 351 – 360, 2001.

[19] V. Kattai, T. Saadre, and L. Savitski, "Estonian oil shale: geology, resource, mining conditions.," *Tallinn: Geological Survey of Estonia*, p. 226, 2000.

[20] I. West, *Burning Beach, Burning Cliffs and the Lyme Volcano: Oil-Shale Fires*. Geology of the Wessex Coast., 2010.

[21] S. [online picture], *Available in http://min-novation-estonia.blogspot.com/ [Accessed october 20, 2011]*.

[22] A. Trikkel, R. Kuusik, A. Martins, T. Pihu, and J. M. Stencel, "Utilization of estonian oil shale semicoke," *Fuel Processing Technology*, vol. 89, no. 8, pp. 756 – 763, 2008.

[23] R. Motlep, K. Kirsimae, P. talviste, E. Puura, and J. Jurgenson, "Mineral composition of estonian oil shale semi-coke sediments," *Estonian Academy Publishers*, vol. 24, no. 3, pp. 405–422, 2007.

[24] M. M. Smadi and R. H. Haddad, "The use of oil shale ash in portland cement concrete," *Cement and Concrete Composites*, vol. 25, no. 1, pp. 43 – 50, 2003.

[25] R. F., E. K., M. R. A., and P. L., *The Alberta Oil Sands: Reserves and Supply Outlook*. Calgary, Alberta, Canada: Energy Resources Conservation Board, 2008.

[26] R. Martínez-Palou, M. de Lourdes Mosqueira, B. Zapata-Rendón, E. Mar-Juárez, C. Bernal-Huicochea, J. de la Cruz Clavel-López, and J. Aburto, "Transportation of heavy and extra-heavy crude oil by pipeline: A review," *Journal of Petroleum Science and Engineering*, vol. 75, no. 3-4, pp. 274 – 282, 2011.

[27] E. D. Attanasi and R. F. Meyer, *Natural bitumen and extra-heavy oil*. London, UK: 2007 Survey of Energy Resources, eds., J. Trinnaman and A. Clarke: World Energy Council, 2007.

[28] C. R. Bartone, L. Leite, T. Triche, and R. Schertenleib, "Private sector participation in municipal solid waste service: Experiences in latin america," *Waste Management and Research*, vol. 9, no. 6, pp. 495 – 509, 1991.

[29] C. Wang, X. Hu, M.-L. Chen, and Y.-H. Wu, "Total concentrations and fractions of cd, cr, pb, cu, ni and zn in sewage sludge from municipal and industrial wastewater treatment plants," *Journal of Hazardous Materials*, vol. 119, no. 1-3, pp. 245 – 249, 2005.

[30] S. Inoue, S. Sawayama, T. Ogi, and S. ya Yokoyama, "Organic composition of liquidized sewage sludge," *Biomass and Bioenergy*, vol. 10, no. 1, pp. 37 – 40, 1996.

[31] M. S. W. [online picture], *Available in http://blogs.ft.com/energy-source [Accessed october 20, 2011]*.

[32] S. [online picture], *Available in http://www.elega.lt [Accessed october 20, 2011]*.

[33] P. Pironi, C. Switzer, J. I. Gerhard, G. Rein, and J. L. Torero, "Self-sustaining smoldering combustion for napl remediation: Laboratory evaluation of process sensitivity to key parameters," *Environmental Science and Technology*, vol. 45, no. 7, pp. 2980–2986, 2011.

[34] C. Switzer, P. Pironi, J. Gerhard, G. Rein, and J. Torero, "Self-sustaining smoldering combustion: A novel remediation process for non-aqueous-phase liquids in porous media," *Environmental Science and Technology*, vol. 43, no. 15, pp. 5871–5877, 2009.

[35] J. Qian and J. Wang, *World Oil Shale Retorting Technologies*. International Conference on Oil Shale:Recent Trends In Oil Shale, 2006.

[36] X. Han, X. Jiang, and Z. Cui, "Studies of the effect of retorting factors on the yield of shale oil for a new comprehensive utilization technology of oil shale," *Applied Energy*, vol. 86, no. 11, pp. 2381 – 2385, 2009.

[37] H. Pforzheimer, *Paraho Oil Shale Project*. Paraho Oil Shale Demonstration, Inc., Anvil Points, Colorado, 1976.

[38] Q. Wang, H. Wang, B. Sun, J. Bai, and X. Guan, "Interactions between oil shale and its semi-coke during co-combustion," *Fuel*, vol. 88, no. 8, pp. 1520 – 1529, 2009.

[39] T. W. Marrero, B. P. McAuley, W. R. Sutterlin, J. S. Morris, and S. E. Manahan, "Fate of heavy metals and radioactive metals in gasification of sewage sludge," *Waste Management*, vol. 24, no. 2, pp. 193 – 198, 2004.

[40] C. J. Roos, *Clean Heat and Power Using Biomass Gasification for Industrial and Agricultural Projects*. WSU Extension Energy Program, Olympia, WA, USA, 2010.

[41] U. Arena, "Process and technological aspects of municipal solid waste gasification. a review," *Waste Management*, no. 0, pp. –, 2011.

[42] G. E. Kit, *Available in http://gekgasifier.com/ [Accessed october 20, 2011]*.

[43] P. Consulting, *Available in http://pr-en-ma.com/ [Accessed october 20, 2011]*.

[44] A. K. Rajvanshi, *Biomass Gasification*, vol. 02. Alternative Energy in Agriculture, 1986.

[45] G. Rein, "Smouldering combustion phenomena in science and technology," 2009.

[46] T.J. and Ohlemiller, "Modeling of smoldering combustion propagation," *Progress in Energy and Combustion Science*, vol. 11, no. 4, pp. 277 – 310, 1985.

[47] A. R. Brandt, "Converting oil shale to liquid fuels: Energy inputs and greenhouse gas emissions of the shell in situ conversion process," *Environmental Science and Technology - American Chemical Society*, vol. 42, 2008.

[48] P. Pironi, C. Switzer, G. Rein, , J. Gerhard, J. Torero, and A. Fuentes, "Small-scale forward smouldering experiments for remediation of coal tar in inert media," *Proceedings of the Combustion Institute*, vol. 32, no. 2, pp. 1957–1964, 2009.

[49] K.N. and Palmer, "Smouldering combustion in dusts and fibrous materials," *Combustion and Flame*, vol. 1, no. 2, pp. 129 – 154, 1957.

[50] D. A. Schultz, B. J. Matkowksky, V. A. Volpert, and A. C. Fernandez-Pello, "Forced forward smolder combustion," *Combustion and Flame*, vol. 104, no. 95, pp. 1–26, 1996.

[51] B. Johnson, G. Froment, and C. Watson, "Temperature profiles in packed beds of catalyst during regeneration," *Chemical Engineering Science*, vol. 17, no. 11, pp. 835 – 848, 1962.

[52] J. Torero and A. Fernandez-Pello, "Forward smolder of polyurethane foam in a forced air flow," *Combustion and Flame*, vol. 106, no. 1?2, pp. 89 – 109, 1996.

[53] M. Sennoune, S. Salvador, and M. Quintard, "Reducing co2 emissions from oil shale semicoke smoldering combustion by varying the carbonate and fixed carbon contents," *Combustion and Flame*, vol. 158, no. 11, pp. 2272 – 2282, 2011.

[54] X. Jiang, X. Han, and Z. Cui, "New technology for the comprehensive utilization of chinese oil shale resources," *Energy*, vol. 32, no. 5, pp. 772 – 777, 2007.

[55] I. C. Lee and H. Y. Sohn, "Experimental investigation and mathematical modeling of the ignition of an oil shale bed with hot air," *Industrial and Engineering Chemistry Process Design and Development*, vol. 24, no. 3, pp. 753–761, 1985.

[56] I. A. Vasalos, A. Lefkopoulos, and M. Georgiadou, "Modeling an oil shale fluid bed combustor," *Industrial and Engineering Chemistry Research*, vol. 27, no. 2, pp. 317–324, 1988.

[57] D.L. and Simms, "Ignition of cellulosic materials by radiation," *Combustion and Flame*, vol. 4, no. 0, pp. 293 – 300, 1960.

[58] D. Simms and M. Law, "The ignition of wet and dry wood by radiation," *Combustion and Flame*, vol. 11, no. 5, pp. 377 – 388, 1967.

[59] J. O. Jaber and S. Probert, "Reaction kinetics of fluidised bed gasification of jordanian oil shales," *International Journal of Thermal Sciences*, vol. 39, no. 2, pp. 295 – 304, 2000.

[60] I. Y. Akkutlu and Y. C. Yortsos, "The dynamics of in-situ combustion fronts in porous media," *Combustion and Flame*, vol. 134, no. 3, pp. 229 – 247, 2003.

[61] M. Kok and M. Pamir, "Astm kinetics of oil shales," *Journal of Thermal Analysis and Calorimetry*, vol. 53, pp. 567–575, 1998.

[62] O. O. Sonibare, R. Egashira, and T. A. Adedosu, "Thermo-oxidative reactions of nigerian oil sand bitumen," *Thermochimica Acta*, vol. 405, no. 2, pp. 195 – 205, 2003.

[63] A. B. Hubbard and W. E. Robinson, *Decomposition study of Colorado Oil Shale*. U.S. Department of Energy - Oklahoma Tulsa, 1950.

[64] V. D. Allred *Chem. Eng. Prog. Symp. Ser.*, vol. 62, 1966.

[65] K. Rajeshwar, R. Nottenburg, and J. Dubow, "Review - thermophysical properties of oil shales," *Journal of Materials Science*, vol. 14, 1979.

[66] H. S. Yang and H. Y. Sohn, "Mathematical analysis of the effect of retorting pressure on oil yield and rate of oil generation from oil shale," *Industrial and Engineering Chemistry Process Design and Development*, vol. 24, no. 2, pp. 274–280, 1985.

[67] W. W. Wendlandt, *Thermal Analysis - Third Edition*. A Wiley-Interscience Publication, 1986.

[68] J. Leifeld, "Thermal stability of black carbon characterised by oxidative differential scanning calorimetry," *Organic Geochemistry*, vol. 38, no. 1, pp. 112 – 127, 2007.

[69] R. G. Moore, C. J. Laureshen, J. D. M. Belgrave, M. G. Ursenbach, and S. A. R. Mehta, "In situ combustion in canadian heavy oil reservoirs," *Fuel*, vol. 74, no. 8, pp. 1169 – 1175, 1995.

[70] L. M. Castanier and W. E. Brigham, "Upgrading of crude oil via in situ combustion," *Journal of Petroleum Science and Engineering*, vol. 39, no. 1-2, pp. 125 – 136, 2003.

[71] D. S. Thakur and H. E. Nuttall, "Kinetics of pyrolysis of moroccan oil shale by thermogravimetry," *Industrial and Engineering Chemistry Research*, vol. 26, no. 7, pp. 1351–1356, 1987.

[72] L. Ballice, M. Yuksel, M. Saglam, H. Schulz, and C. Hanoglu, "Application of infrared spectroscopy to the classification of kerogen types and the thermogravimetrically derived pyrolysis kinetics of oil shales," *Fuel*, vol. 74, no. 11, pp. 1618 – 1623, 1995.

[73] G. Debenest, *Simulation numérique 3D, à la microéchelle, de la combustion en lit fixe de schistes bitumineux*. PhD thesis, l'Université de Poitiers, 2003.

[74] A. K. Burnham, "Chemical kinetics and oil shale process design," *NATO Advanced Study Institute: Composition:Geochemistry and Conversion of Oil Shale*, 1993.

[75] W. D. Schnackenberg and C. H. Prien *Industrial and Engineering Chemistry*, vol. 45, no. 313, 1953.

[76] S.-M. Shih and H. Y. Sohn, "Nonisothermal determination of the intrinsic kinetics of oil generation from oil shale," *Industrial and Engineering Chemistry Process Design and Development*, vol. 19, no. 3, pp. 420–426, 1980.

[77] A. Karabakan and Y. Yürüm, "Effect of the mineral matrix in the reactions of oil shales: 1. pyrolysis reactions of turkish göynük and us green river oil shales," *Fuel*, vol. 77, no. 12, pp. 1303 – 1309, 1998.

[78] M. Kok, G. Pokol, C. Keskin, J. Madarász, and S. Bagci, "Combustion characteristics of lignite and oil shale samples by thermal analysis techniques," *Journal of Thermal Analysis and Calorimetry*, vol. 76, pp. 247–254, 2004.

[79] H. Barkia, L. Belkbir, and S. Jayaweera, "Kinetic studies of oxidation of residual carbon from moroccan oil shale kerogens," *Journal of Thermal Analysis and Calorimetry*, vol. 86, pp. 121–123, 2006.

[80] P. Murugan, N. Mahinpey, T. Mani, and K. Asghari, "Effect of low-temperature oxidation on the pyrolysis and combustion of whole oil," *Energy*, vol. 35, no. 5, pp. 2317 – 2322, 2010.

[81] E. S. Freeman and B. Carroll, "Reaction kinetics in differential thermal analysis," *J. Phys. Chem.*, vol. 62, 1958.

[82] H. E. Kissinger, "Reaction kinetics in differential thermal analysis," *Analytical chemistry*, vol. 29, no. 11, pp. 1702–1706, 1957.

[83] A. Aboulkas, K. E. harfi, and A. E. bouadili, "Kinetic and mechanism of tarfaya (morocco) oil shale and ldpe mixture pyrolysis," *Journal of Materials Processing Technology*, vol. 206, no. 1-3, pp. 16 – 24, 2008.

[84] A. W. Coats and J. P. Redfern, "Reaction kinetics in differential thermal analysis," *Nature*, vol. 201, 1964.

[85] P. T. Williams and N. Ahmad, "Investigation of oil-shale pyrolysis processing conditions using thermogravimetric analysis," *Applied Energy*, vol. 66, no. 2, pp. 113 – 133, 2000.

[86] T. Ozawa, "A new method of analyzing thermogravimetric data," *Bulletin Of The Chemical Society of Japan*, vol. 38, no. 11, pp. 1881–1886, 1965.

[87] A. Aboulkas, K. E. harfi, M. Nadifiyine, and A. E. bouadili, "Investigation on pyrolysis of moroccan oil shale/plastic mixtures by thermogravimetric analysis," *Fuel Processing Technology*, vol. 89, no. 11, pp. 1000 – 1006, 2008.

[88] M. V. Kok and M. R. Pamir, "Comparative pyrolysis and combustion kinetics of oil shales," *Journal of Analytical and Applied Pyrolysis*, vol. 55, no. 2, pp. 185 – 194, 2000.

[89] T. Hatakeyama and F. Quinn, *Thermal Analysis: Fundamentals and Applications to Polymer Science*. John Wiley and Sons Ltd - England, 1999.

[90] L. Elliott, D. Ingham, A. Kyne, N. Mera, M. Pourkashanian, and C. Wilson, "The use of ignition delay time in genetic algorithms optimisation of chemical kinetics reaction mechanisms," *Engineering Applications of Artificial Intelligence*, vol. 18, no. 7, pp. 825 – 831, 2005.

[91] M. Frenklach, H. Wang, and M. J. Rabinowitz, "Optimization and analysis of large chemical kinetic mechanisms using the solution mapping method–combustion of methane," *Progress in Energy and Combustion Science*, vol. 18, no. 1, pp. 47 – 73, 1992.

[92] J. H. Holland, *Adaptation in Natural and Artificial Systems*. The University of Michigan Press, AnnArbor, MI., 1975.

[93] C. Lautenberger, G. Rein, and C. Fernandez-Pello, "The application of a genetic algorithm to estimate material properties for fire modeling from bench-scale fire test data," *Fire Safety Journal*, vol. 41, no. 3, pp. 204 – 214, 2006.

[94] G. Rein, C. Lautenberger, A. C. Fernandez-Pello, J. L. Torero, and D. L. Urban, "Application of genetic algorithms and thermogravimetry to determine the kinetics of

polyurethane foam in smoldering combustion," *Combustion and Flame*, vol. 146, no. 1-2, pp. 95 – 108, 2006.

[95] K. Levenberg, "A method for the solution of certain problems in least squares," *Quart. Appl. Math.*, vol. 2, pp. 164–168, 1944.

[96] D. Marquardt, "An algorithm for least-squares estimation of nonlinear parameters," *SIAM J. Appl. Math.*, vol. 11, pp. 431–441, 1963.

[97] F. Fang, B.-J. Ni, and H.-Q. Yu, "Estimating the kinetic parameters of activated sludge storage using weighted non-linear least-squares and accelerating genetic algorithm," *Water Research*, vol. 43, no. 10, pp. 2595 – 2604, 2009.

[98] A. K. Sadhukhan, P. Gupta, and R. K. Saha, "Modelling and experimental studies on pyrolysis of biomass particles," *Journal of Analytical and Applied Pyrolysis*, vol. 81, no. 2, pp. 183 – 192, 2008.

[99] T. Loulou, S. Salvador, and J. Dirion, "Determination of reaction parameters for cardboard thermal degradation using experimental data," *Chemical Engineering Research and Design*, vol. 81, no. 9, pp. 1265 – 1270, 2003.

[100] C. Reverte, J.-L. Dirion, and M. Cabassud, "Kinetic model identification and parameters estimation from tga experiments," *Journal of Analytical and Applied Pyrolysis*, vol. 79, no. 1-2, pp. 297 – 305, 2007.

[101] K. Ragland, D. Aerts, and A. Baker, "Properties of wood for combustion analysis," *Bioresource Technology*, vol. 37, no. 2, pp. 161 – 168, 1991.

[102] B. Peters and C. Bruch, "Drying and pyrolysis of wood particles: experiments and simulation," *Journal of Analytical and Applied Pyrolysis*, vol. 70, no. 2, pp. 233 – 250, 2003.

[103] D. L. Pyle and C. Zaror, "Heat transfer and kinetics in the low temperature pyrolysis of solids," *Chemical Engineering Science*, vol. 39, no. 1, pp. 147–158, 1984.

[104] M. F. Martins, M. A. B. Zanoni, and E. N. Macêdo, *Modeling the Thermochemical Conversion of Single Wood Particle*, vol. II. Biomass and Renewable. In: Prof Daniel Favrat

(Author); MER François Maréchal (Author); Yannick Bravo (Creator); Nicolas Borboën (Creator). (Org.). ECOS 2010: Proceedings of ECOS 2010 Conference in Lausanne. 1 ed., 2011.

[105] A. Oliveira and M. Kaviany, "Nonequilibrium in the transport of heat and reactants in combustion in porous media," *Progress in Energy and Combustion Science*, vol. 27, no. 5, pp. 523 – 545, 2001.

[106] D. Shin and S. Choi, "The combustion of simulated waste particles in a fixed bed," *Combustion and Flame*, vol. 121, no. 1-2, pp. 167 – 180, 2000.

[107] B. S. Gottfried, "A mathematical model of thermal oil recovery in linear systems.," *Soc. Pet. Eng. J.*, pp. 196 – 210, 1965.

[108] H. Zhou, A. Jensen, P. Glarborg, P. Jensen, and A. Kavaliauskas, "Numerical modeling of straw combustion in a fixed bed," *Fuel*, vol. 84, no. 4, pp. 389 – 403, 2005.

[109] G. Debenest, V. V. Mourzenko, and J. F. Thovert, "Smouldering in fixed beds of oil shale grains: governing parameters and global regimes," *Combustion Theory and Modelling*, vol. 9, no. 2, pp. 301–321, 2005.

[110] M. Ozisik and H. Orlande, *Inverse Heat Transfer: Fundamentals and Applications*. New York: Taylor and Francis, 2000.

[111] L. B. Dantas, H. R. B. Orlande, and R. M. Cotta, "Estimation of dimensionless parameters of luikov's system for heat and mass transfer in capillary porous media," *International Journal of Thermal Sciences*, vol. 41, no. 3, pp. 217 – 227, 2002.

[112] J. Hadamard, *Le probleme de Cauchy et les equations aux derivees partielles lineaires hyperboliques*. Hermann: Paris, 1932.

[113] N. R. Farooji, A. Vatani, and S. Mokhtari, "Kinetic simulation of oxidative coupling of methane over perovskite catalyst by genetic algorithm: Mechanistic aspects," *Journal of Natural Gas Chemistry*, vol. 19, no. 4, pp. 385 – 392, 2010.

[114] A. Eftaxias, J. Font, A. Fortuny, A. Fabregat, and F. Stüber, "Nonlinear kinetic parameter estimation using simulated annealing," *Computers and Chemical Engineering*, vol. 26, no. 12, pp. 1725 – 1733, 2002.

[115] R. C. O. Sebastião and J. P. Braga, "Retrieval of kinetic rates in reactions with semi batch liquid phase using ill-posed inverse problem theory," *Quimica Nova*, vol. 34, pp. 213 – 217, 00 2011.

[116] J. Beck and K. Arnold, *Parameter Estimation in Engineering and Science*. New York: Wiley, 1977.

[117] L. Dantas, H. Orlande, and R. Cotta, "An inverse problem of parameter estimation for heat and mass transfer in capillary porous media," *International Journal of Heat and Mass Transfer*, vol. 46, no. 9, pp. 1587 – 1598, 2003.

[118] G. Varhegyi, "Aims and methods in non-isothermal reaction kinetics," *Journal of Analytical and Applied Pyrolysis*, vol. 79, no. 1?2, pp. 278 – 288, 2007.

[119] C. Reverte, J.-L. Dirion, and M. Cabassud, "Kinetic model identification and parameters estimation from tga experiments," *Journal of Analytical and Applied Pyrolysis*, vol. 79, no. 1?2, pp. 297 – 305, 2007.

[120] M. V. Kok, "Oil shale : Pyrolysis , combustion , and environment : A review," *Energy Sources*, vol. 24, no. 2, pp. 135–143, 2002.

[121] A. Sadiki, W. Kaminsky, H. Halim, and O. Bekri, "Fluidised bed pyrolysis of moroccan oil shales using the hamburg pyrolysis process," *Journal of Analytical and Applied Pyrolysis*, vol. 70, no. 2, pp. 427 – 435, 2003.

[122] J. Liu and J. Zhang, "Assessment of the apparent activation energies for gas/solid reactions carbonate decomposition.," *Journal of University of Science and Technology Beijing*, vol. 10, pp. 25 – 29, 2003.

[123] A. K. Galwey and M. E. Brown, "Arrhenius parameters and compensation behaviour in solid-state decompositions," *Thermochimica Acta*, vol. 300, no. 1-2, pp. 107 – 115, 1997.

[124] Y. Soni and W. J. Thomson, "Oxidation kinetics of oil shale char," *Ind. Eng. Chem. Process Des. Dev.*, 1979.

[125] M. V. Kok and A. G. Iscan, "Oil shale kinetics by differential methods.," *Journal of Thermal Analysis and Calorimetry*, vol. 88, pp. 657 – 661, 2007.

[126] W. J. Thomson, K. A. Helling, and R. J. Rodriquez, "Dxrd studies of oil shale mineral reactions," *Energy and Fuels*, vol. 2, no. 1, pp. 9–13, 1988.

[127] A. Lapene, M. F. Martins, G. Debenest, M. Quintard, and S. Salvador., "Numerical simulation of oil shale combustion in a fixed bed: Modelling and chemical," *Eurotherm Seminar N° 81 Reactive Heat Transfer in Porous Media, Albi, France*, 2007.

[128] A. Lapene, G. Debenest, M. Quintard, M. F. Martins, , and S. Salvador., "Numerical simulation of combustion in reactive porous media," *International Review of Mechanical Engineering (I.RE.M.E.)*, 2008.

[129] A. Lapene, "Modélisation numérique de la combustion en lit fixe de combustibles solides," *Rapport de stage, IMFT, Toulouse: Master Recherche en Dynamique des Fluides, Energétique et Transferts*, 2006.

[130] H. Fadaei, M. Sennoune, S. Salvador, A. Lapene, and G. Debenest, "Modelling of non-consolidated oil shale semi-coke forward combustion: Influence of carbon and calcium carbonate contents," *Fuel*, vol. 95, no. 0, pp. 197 – 205, 2012.